

University of St Andrews



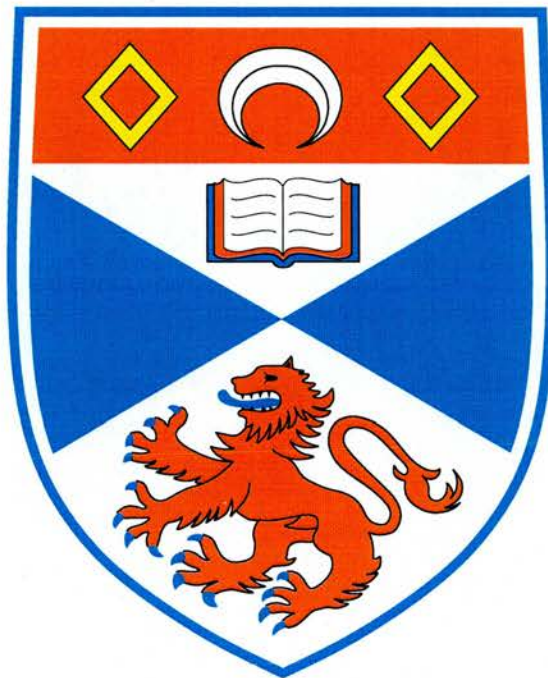
Full metadata for this thesis is available in
St Andrews Research Repository
at:

<http://research-repository.st-andrews.ac.uk/>

This thesis is protected by original copyright

Quiet-Sun Coronal Fields and the Magnetic Carpet

Robert M. Close



Thesis submitted for the degree of Doctor of Philosophy of
the University of St Andrews

August 31, 2004



Th E863

Abstract

The visible surface of the Sun, the photosphere, is covered with a multitude of small magnetic fragments that form a “magnetic carpet”. Understanding the behaviour of these fragments and the overlying magnetic fields that they produce is crucial to unravelling the nature of coronal heating.

This thesis, spurred on by observations, is an examination of various aspects of the magnetic carpet. MDI magnetograms are used as input to a model which investigates the connections between opposite-polarity fragments, as well as examining the origin of the flux present at various altitudes. The domain structures through which the many opposite-polarity connections are forged are examined and classified according to their geometry and topological features.

The abundance of magnetic separators in mixed-polarity magnetic fields is then estimated using both a Monte Carlo experiment and a model based on observed data. It is found that they are more abundant than one would expect, since some pairs of nulls are linked by more than one separator. The orientation of separators about null points, as well as connections between coronal nulls, is also studied.

MDI data is then used again in order to determine the timescales over which coronal flux is recycled. After determining changes in domain fluxes due to emergence and cancellation of flux between magnetogram images, it is found that coronal flux is recycled in only a fraction of the time taken to recycle all photospheric flux. Typical separator currents required to maintain observed heating rates are also calculated.

Finally, a $2\frac{1}{2}D$ model is used to estimate how complexity affects the separatrix currents that result from shearing motions applied to magnetic sources. The main factors that affect the current are found to be the number of sources through which a given amount of flux emerges through the photosphere, along with the spatial distribution of the sources.

Declaration

- (i) I, Robert M. Close, hereby certify that this thesis, which is approximately 43 000 words in length, has been written by me, that it is the record of work carried out by me and that it has not been submitted in any previous application for a higher degree.

Name: Robert M. Close **Signature:**

Date: 4-3-05

- (ii) I was admitted as a research student in September 2001 and as a candidate for the degree of Doctor of Philosophy in September 2001; the higher study for which this is a record was carried out in the University of St Andrews between 2001 and 2004.

Name: Robert M. Close **Signature:..**

Date: 4-3-05

- (iii) I hereby certify that the candidate has fulfilled the conditions of the Resolution and Regulations appropriate for the degree of Doctor of Philosophy in the University of St Andrews and that the candidate is qualified to submit this thesis in application for that degree.

Name: Eric R. Priest **Signature:..**

Date: 4-3-05

- (iv) In submitting this thesis to the University of St Andrews I understand that I am giving permission for it to be made available for use in accordance with the regulations of the University Library for the time being in force, subject to any copyright vested in the work not being affected thereby. I also understand that the title and abstract will be published, and that a copy of the work may be made and supplied to any bona fide library or research worker.

Name: Robert M. Close **Signature:..**

Date: 4-3-05

Acknowledgements

There are many people in St Andrews and elsewhere who have provided invaluable assistance throughout my three years as a research student in St Andrews. In particular, I would like to thank my supervisors Clare Parnell and Eric Priest for their continual patience, advice and support.

I would also like to thank many others in the solar group here in St Andrews, among them Duncan Mackay and Daniel Brown, as well as collaborators from further afield, namely Jean Heyvaerts and Dana Longcope. I am especially indebted to those who have put up with my frequent hawing during coffee breaks.

I must express my gratitude for the financial support provided by the Particle Physics and Astronomy Research Council. Additionally, I would like to thank Richard Harrison and the Rutherford Appleton Laboratory for my CASE studentship, along with PLATON, whose funding made my collaborative trips to Strasbourg possible.

On a personal level, I would like to acknowledge my family for their constant encouragement and support, and my friends for providing a welcome distraction from my work.

Lastly, I would like to thank my girlfriend Minamiko for all the fun we've had over the past three years.

Contents

Contents	i
1 Introduction	1
1.1 The Sun	1
1.1.1 The Solar Interior	1
1.1.2 The Solar Photosphere	2
1.1.3 The Solar Atmosphere	3
1.2 The Magnetic Sun	4
1.2.1 Quiet-Sun Regions	5
1.3 Modelling the Sun's Magnetic Field	7
1.3.1 Magnetohydrostatics	10
1.4 Topology and the Potential Field Approximation	11
1.4.1 Representing Photospheric Fragments	12
1.4.2 The Topological Skeleton	13
1.5 Some Results and Theories	14
1.6 Outline	16
2 Statistical Flux-Tube Properties of 3D Magnetic-Carpet Fields	19
2.1 Introduction	19
2.2 Analysing the Magnetic Carpet	20
2.3 Flux-Tube Characteristics	23
2.3.1 A Balanced Inner Region	25
2.3.2 An Unbalanced Inner Region	27
2.4 Connectivity	31
2.4.1 Balanced Region	31
2.4.2 Unbalanced Region	35

2.5	Properties of Fragments	37
2.5.1	Balanced Region	38
2.5.2	Unbalanced Region	38
2.6	Conclusions	39
3	A Categorisation of the Building Blocks of Coronal Magnetic Fields	43
3.1	Introduction	43
3.2	Two Key Building Blocks of 3D Fields	44
3.3	Locating Separators	46
3.3.1	Tracing Separator Curves	48
3.4	Classification of Magnetic Domains: An Extrapolation with no Upright Nulls	49
3.4.1	Topology Equations	50
3.4.2	Photospheric Separator-Ring Domains	53
3.4.3	A Multiply Connected Pair of Sources	56
3.4.4	Coronal Domains	57
3.5	Magnetic Fields Containing Upright Nulls	58
3.5.1	Photospheric Domains about Upright Nulls	58
3.5.2	Semi-Coronal Domains	59
3.6	Conclusions	61
4	Separators in Quiet-Sun Magnetic Fields	63
4.1	Introduction	63
4.2	An Exponential Distribution of Source Strengths	64
4.3	Monte Carlo Simulation	65
4.3.1	Separator Densities	67
4.3.2	Density of Topologically Distinct Regions	68
4.3.3	Separator Bunching	71
4.3.4	Connections between Coronal Nulls	76
4.4	An Observed Sequence of Magnetograms	77
4.4.1	Separator Distributions	79
4.5	Conclusions	82
5	Coronal Flux Recycling Times	85

5.1	Introduction	85
5.2	Photospheric Flux Fragments	87
5.3	Analysis	89
5.3.1	Comparing Magnetogram Pairs	90
5.3.2	Emergence, Cancellation and Reconnection	92
5.4	Scenario 1: Excluding Emergence and Cancellation	94
5.4.1	Coronal Flux Recycling Time Due to Reconnection Driven by Footpoint Motions Alone	96
5.5	Scenario 2: Including Emergence and Cancellation	97
5.5.1	Photospheric Recycling Times	100
5.5.2	Coronal Recycling Time Due to Emergence and Cancellation	101
5.5.3	Coronal Recycling Time Due to Reconnection Driven by Emer- gence, Cancellation and Motions of Fragments	103
5.6	Energy Dissipation	104
5.7	Conclusions	107
6	Coronal Tectonics Model	109
6.1	Introduction	109
6.2	Flux Tube Tectonics	111
6.2.1	Overview of 2D Magnetic Fields	111
6.2.2	Non-Constant- α Force-Free Fields	112
6.3	Perturbation of 2D Potential Field into a 2 ¹ / ₂ D Force-Free Field	114
6.3.1	Infinitesimal Perturbations by Shearing Footpoints of a Potential Field	114
6.3.2	Peculiarities of Fragmented-Flux Model	115
6.4	Extra Energy Stored	116
6.5	Example: Four Sources	118
6.6	Effects of Complexity	121
6.6.1	Scenario 1: Constant Source Strengths	123
6.6.2	Scenario 2: Random Source Strengths	127
6.7	A Comparison of Separator and Separatrix Heating	128
6.7.1	2D Separator Current Sheet Formation	129
6.7.2	Analogous Separatrix Stick-Slip Reconnection	130
6.7.3	Comparison of Energy Storage	131

6.8	Conclusions	133
7	Discussions and Future Work	135
7.1	Discussion	135
7.2	Future Work	137
	Appendix A: Comparison of Photospheric Fragment Representations	139
A.1	Flux Tube Characteristics	140
A.2	Connectivity	142
	Appendix B: Boxcar Data Smoothing	145
	Appendix C: Effects of Data Smoothing	147
	Appendix D: Specific Volume about a 2D Null Point	151
	Appendix E: Energy Storage in a 3D Configuration	153
	Appendix F: CD Information	155
	Bibliography	157

Chapter 1

Introduction

水	蛙	古	An old pond
の	飛	池	A frog leaps in
音	び	や	The sound of water
	込		
	む		

松尾芭蕉

MATSUO BASHO (1644–1694)

1.1 The Sun

The Sun is by far the most dominant feature in our solar system, accounting for approximately 98% of its mass. Situated 1.497×10^8 km from the Earth at the centre of the solar system, it is actually a fairly ordinary star of spectral type G2 V and absolute stellar magnitude 4.83. However, our close proximity to the Sun makes it special, as it provides a unique opportunity for us to gain an invaluable insight and understanding into the behaviour of stars in general.

1.1.1 The Solar Interior

Traditionally, the interior of the Sun has been viewed in terms of a series of layers, as illustrated in Figure 1.1. The innermost region of the Sun, the core, extends from the centre of the Sun to about $0.25 R_{\odot}$. It is there that the temperature of 1.5×10^7 Kelvin and pressure of 340 billion times the Earth's air pressure at sea level allow thermonuclear reactions to take place, generating some 99% of the Sun's energy.

In the region above the core, the radiative layer, the high density of the plasma pre-

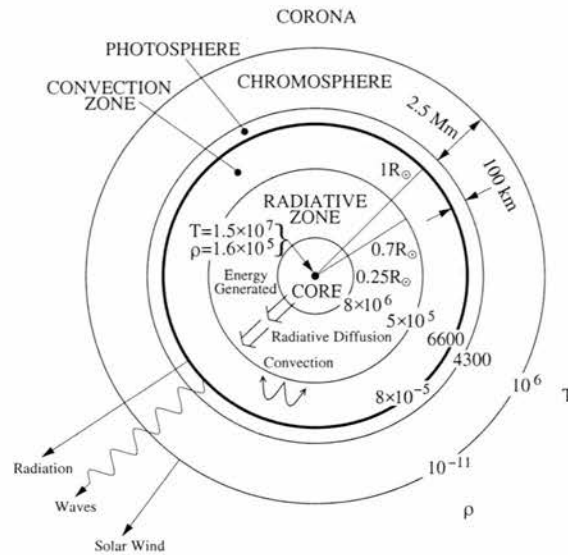


Figure 1.1: Structure of the Sun. The temperatures shown are in degrees Kelvin and the densities are in kg m⁻³. The radius of the Sun, R_{\odot} , is 6.96×10^8 Mm.

vents the radiation from the core from travelling unimpeded to the solar surface, a process that would take around 2 seconds. Instead, the many collisions between the photons and the plasma (or absorptions and re-emissions of energy) mean that the photons follow a ‘random walk’ through the radiative layer, a process which takes around 170 thousand years. Hence, the photons that start out as gamma rays emerge as visible light having lost more than 99.999% of their energy.

At around $0.7 R_{\odot}$, the Sun’s interior becomes too cool and too opaque to allow any further radiative transport of energy. At this point, huge convection currents give rise to a cellular pattern by causing the plasma to rise, cool and fall in a cyclic motion akin to the way in which bubbles transfer energy in boiling water. This process efficiently transfers energy over a distance of around 2.1×10^5 km to the solar surface.

1.1.2 The Solar Photosphere

Above the convection zone lies the visible surface of the Sun that we are most familiar with, the solar photosphere. The photosphere is a very narrow region of only around 100 km in thickness, from which the majority of the energy that we receive from the Sun originates. At this level, the temperature is around 6600 K, and it is only here that direct observations of the various features of the outer Sun can start to be made. It is for this reason that the photosphere is commonly known as the solar surface. The photospheric surface is characterised by the granular and supergranular flow patterns resulting from the

convection below.

Granules, which are the tops of convection cells, are small cellular features, typically 1000 km in diameter, that cover the entire surface of the Sun (except those regions occupied by sunspots). Hot material from the solar interior rises in the centre of each granule and spreads out to the cell boundaries where it cools and drains. Thus, cell centres appear bright, whereas the boundaries appear dark. On average, granules survive for around 8 minutes.

Supergranular cells exist in addition to granular cells, and their sizes range from 13 Mm to 18 Mm in diameter (mean 14 Mm) (Hagenaar et al., 1997), although they are generally irregular in shape and size. They are best seen by observing Doppler shifts in the light emitted by the photospheric material in motion. Supergranule cells typically last for 1–2 days.

1.1.3 The Solar Atmosphere

Proceeding outwards to the base of the chromosphere, a highly non-uniform layer of around 2000–3000 km in thickness, the temperature decreases to around 4400 K. However, rather unintuitively, the temperature then starts rising, and reaches a temperature of around 10 000 K at the top of the chromosphere.

Above the chromosphere, the temperature continues to rise further, and exhibits a sharp increase through a narrow layer termed the transition region. Over a 30 km distance, the temperature rises from 3×10^4 to 3×10^5 K. The temperature continues rising above this, increasing from 3×10^5 to 10^6 K within 2500 km.

The temperature attains a mean value of over a million Kelvin in the outermost layer of the Sun's atmosphere, the solar corona. The solar corona, which extends from the top of the transition region out to the Earth and beyond into interstellar space, may be observed by the naked eye during solar eclipses as a halo that crowns the Sun. The corona gives rise to a multitude of interesting features that occur as a consequence of the dominant magnetic fields that are present there.

Around sunspots and active regions, closed magnetic field lines connect magnetic regions on the solar surface and show up as magnificent loop structures in the corona.

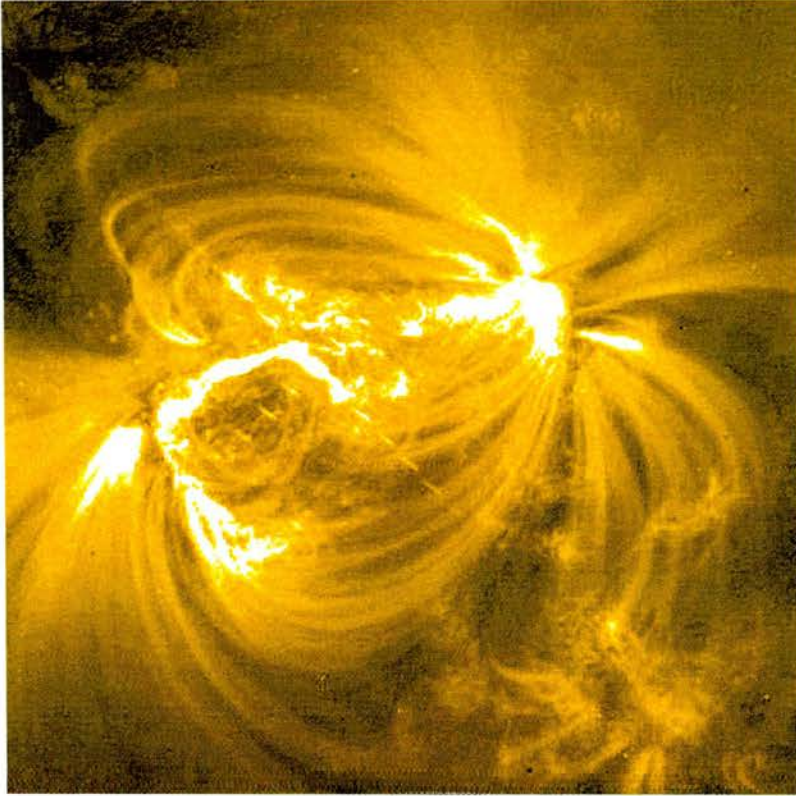


Figure 1.2: Coronal loop structures as seen by the TRACE spacecraft.

1.2 The Magnetic Sun

The surface of the Sun exhibits differential rotation, meaning that the poles rotate slower than the equator. The result of this is that the Sun has a rotation period of 35 days at the poles, but only 25 days at the equator. Solar seismological studies have demonstrated that this behaviour persists throughout the convection zone; however, at a radius corresponding to the base of the convection zone, termed the tachocline, the picture changes and the Sun rotates as a solid body through the radiative layer and the core. The interface layer between the top of the radiative zone and the base of the convection zone is believed to be the seat of a deep-rooted mechanism that generates intense, large-scale magnetic fields, called the solar dynamo. These intense magnetic fields rise to the solar surface due to magnetic buoyancy and pierce through the photosphere, producing a variety of phenomena in the solar atmosphere. Figure 1.2 shows an example of the typical kind of loop structures that one would associate with the magnetic concentrations that characterise the solar photosphere.

Typically, the fields that are observed at the photospheric level are divided into two classes, namely *quiet-Sun regions* and *active regions* (illustrated in Figure 1.3). The tra-

ditional view is that active region fields arise as a direct consequence of the large-scale solar dynamo, whilst quiet-Sun fields are a by-product of this process. Recently, however, it has been realised that other dynamo processes may be at work in the Sun. The continued presence of quiet-Sun fields at solar minimum, when active regions are generally absent, has led to the suggestion that the quiet-Sun photospheric flux is generated by local dynamo action just below the Sun's surface, driven by granular and supergranular flows (Meneguzzi and Pouquet, 1989; Durney et al., 1993; Petrovay and Szakály, 1993; Lin, 1995; Hughes et al., 1998; Tobias, 2002). In practice, it is likely that both mechanisms are at work, so that the problem lies with determining how substantial a role each mechanism plays in the generation of quiet-Sun magnetic fields.

In this thesis, it is the smaller quiet-Sun magnetic fields, rather than the large, conglomerate active region fields, that are subject to scrutiny.

1.2.1 Quiet-Sun Regions

It was previously thought that the quiet Sun, with fields ranging from the detection limit of $\sim 10^{16}$ Mx up to about 3×10^{20} Mx, is static and uneventful, with magnetic fields that are unimportant. However, in recent years it has been realised that the quiet Sun is in fact highly dynamic and complex in nature. A magnetogram image of the line-of-sight magnetic field associated with a typical quiet-Sun region is shown in Figure 1.3.

At the photospheric level, quiet-Sun regions are made up of an interwoven array of small magnetic fragments, termed the 'magnetic carpet' (Schrijver et al., 1997). Magnetic flux is located in many fragments that form a network-like pattern which evolves with the supergranular convection. The majority of the quiet-Sun flux originates in so-called *ephemeral regions*, which have a total absolute flux ranging from 2.6×10^{18} Mx to 407×10^{18} Mx (Hagenaar, 2001). Title (2000) found that initially they diverge rapidly at a speed of 4.5 km s^{-1} , growing in flux until they acquire their maximum flux. This birth phase occurs over about 30 minutes. They then slow down to around 1.4 km s^{-1} as they drift towards the supergranule boundary. They are later characterised by a further reduction in speed, typically to around $0.7\text{--}1.7 \text{ km s}^{-1}$ (Harvey, 1993). Title (2000) also found that the average flux concentration in the quiet Sun only travels around 25 000 km before cancelling. Ephemeral regions essentially form clusters of fragments, whose total net flux is zero, and have a slight tendency to appear near the edges of supergranule cells (Wang, 1988). Hagenaar (2001) found the mean flux per ephemeral region to be around 11.3×10^{18} Mx, emerging at an average rate of 4.4×10^4 per day (averaged over the en-

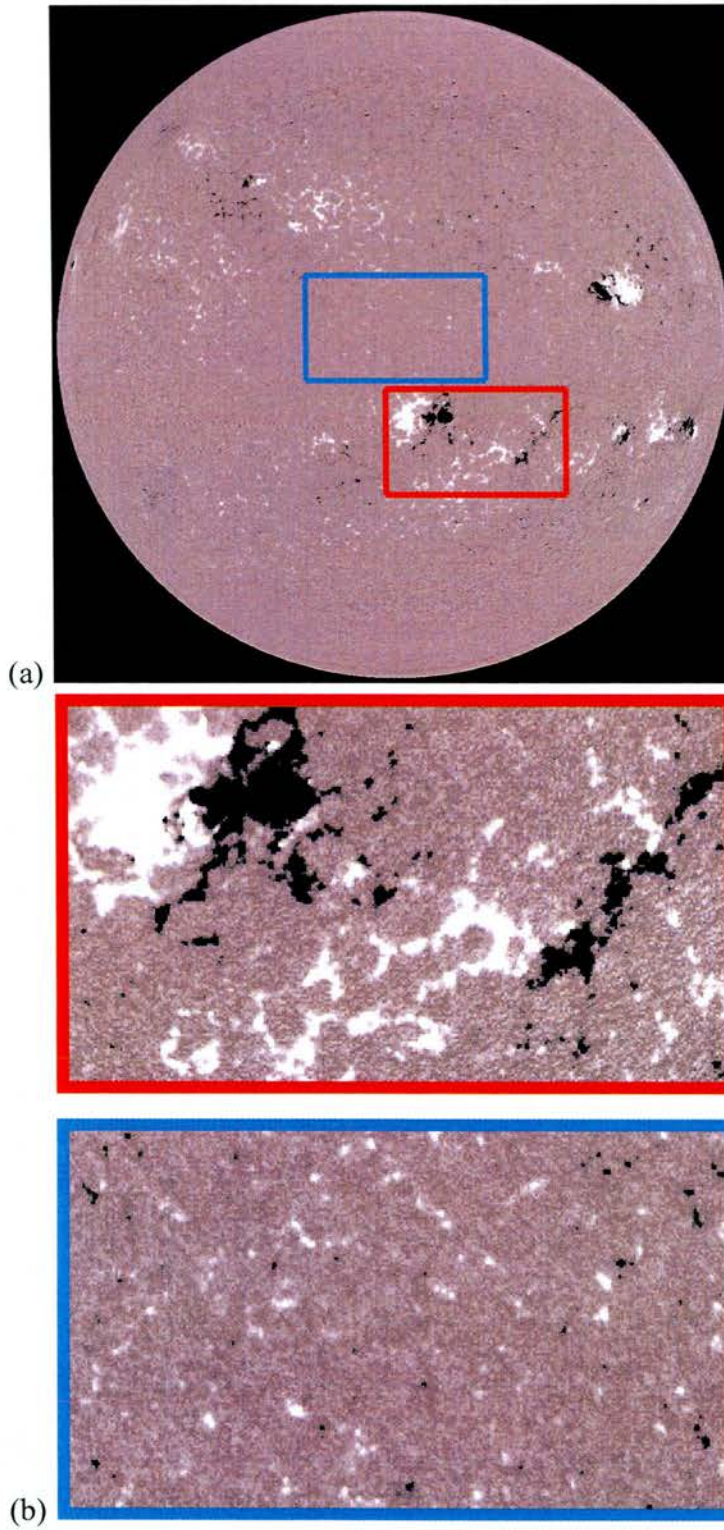


Figure 1.3: (a) Full-disk magnetogram showing the line-of-sight component of the photospheric magnetic field. An active region is highlighted by the red rectangle, whilst the blue rectangle highlights a quiet-Sun region (Courtesy of SOHO/MDI). (b) Close-ups of the two highlighted regions.

tire Sun). With this rate of emergence, the magnetic field in the quiet Sun can be replaced every 14 hours. (Recent work by Hagenaar et al. (2003) revised this figure to 8–19 hours).

The quiet Sun is dominated by *network fragments*, 90% of whose flux originates in ephemeral regions (Martin, 1990). Network regions (Martin, 1988) are typically found at sites of strong downflow, usually at the confluence of two or more supergranule cells. They have typical strengths of 10^{18} – 10^{19} Mx, and typical diameters of 1000–10 000 km. The remaining 10% of flux in the network fragments comes from the piling up of *intranetwork fragments* (Livingston and Harvey, 1975; Martin, 1984, 1988, 1990; Livi et al., 1985; Wang et al., 1985; Wang and Shi, 1988; Wang and Zirin, 1988; Wang et al., 1988; Zirin, 1985, 1987). These fragments have typical fluxes of 10^{16} – 10^{18} Mx (average 5×10^{16} Mx). Intranetwork fragments are very small (diameter ~ 2000 km) and relatively short-lived. As such, it has traditionally been believed that intranetwork regions have little impact on the outer atmosphere.

The typical behaviour of the photospheric magnetic flux in the quiet Sun can be described by four processes: (i) *emergence* – the appearance of new flux from below the photosphere; (ii) *cancellation* – the mutual loss of flux from opposite-polarity magnetic fragments; (iii) *fragmentation* – the break-up of fragments into smaller ones and (iv) *coalescence* – the merging of fragments of the same sign to form a single larger fragment.

Recent models by Parnell (2001) and Simon et al. (2001) for the way in which the Sun's magnetic field distribution is created and maintained by ephemeral flux emergence, fragmentation, coalescence and cancellation built upon previous work by Schrijver et al. (1997) and van Ballegooijen et al. (1998). Parnell estimated that the average emergence rate of new flux in the quiet Sun must lie between 6×10^{-2} and 10^{-5} Mx cm $^{-2}$ s $^{-1}$ in order to maintain an absolute flux density of 2.5–3 G. This requires a fragmentation rate of more than 12×10^{-5} s $^{-1}$ in order to agree with observations.

1.3 Modelling the Sun's Magnetic Field

The magnetic field that emerges into the Sun's atmosphere from the flux concentrations on the photosphere obeys the equations of magnetohydrodynamics (MHD) (see, for example, Priest (1982) or Boyd and Sanderson (2003) for a detailed discussion). These essentially consist of a simplified form of Maxwell's equations together with Ohm's Law, a gas law, and equations of mass continuity, motion and energy.

In mks units, Maxwell's equations may be expressed as-

$$\nabla \times \mathbf{B} = \mu \mathbf{j} + \frac{1}{c^2} \frac{\partial \mathbf{E}}{\partial t}, \quad (1.1)$$

$$\nabla \cdot \mathbf{B} = 0, \quad (1.2)$$

$$\nabla \times \mathbf{E} = -\frac{\partial \mathbf{B}}{\partial t}, \quad (1.3)$$

$$\nabla \cdot \mathbf{E} = \frac{\rho_0}{\epsilon}, \quad (1.4)$$

where \mathbf{B} is the magnetic induction (loosely referred to as the magnetic field), \mathbf{E} is the electric field, \mathbf{j} is the current density, μ is the magnetic permeability, ϵ is the permittivity of free space, ρ_0 is the charge density and c is the speed of light in a vacuum. In non-relativistic MHD, the plasma flow speed v_0 is much less than the speed of light c (i.e. $v_0 \ll c$), so that Equation (1.1) reduces to Ampère's law, namely

$$\nabla \times \mathbf{B} = \mu \mathbf{j}. \quad (1.5)$$

It is also worth noting here that for solar plasmas, μ and ϵ are approximated by their vacuum values, μ_0 and ϵ_0 , respectively.

Plasma moving with a velocity \mathbf{v} across a magnetic field is subject to an electric field $\mathbf{v} \times \mathbf{B}$. Since there may also be an electric field \mathbf{E} which would act on the material at rest, Ohm's law may be written as:

$$\mathbf{j} = \sigma(\mathbf{E} + \mathbf{v} \times \mathbf{B}), \quad (1.6)$$

where σ is the electrical conductivity.

The equation of mass continuity,

$$\frac{\partial \rho}{\partial t} + \nabla \cdot (\rho \mathbf{v}) = 0, \quad (1.7)$$

states that the density at a point increases ($\partial \rho / \partial t > 0$) if mass flows into the surrounding region ($\nabla \cdot (\rho \mathbf{v}) < 0$), whereas it decreases when there is a divergence of the mass flux.

The equation of motion may be stated as

$$\rho \frac{D\mathbf{v}}{Dt} = -\nabla p + \mathbf{j} \times \mathbf{B} + \rho \mathbf{g} + \mathbf{F}_\nu, \quad (1.8)$$

where ρ is the plasma density, p is the plasma pressure, \mathbf{g} is the gravitational acceleration,

\mathbf{F}_ν is the viscous force (neglected here) and

$$\frac{D\mathbf{v}}{Dt} = \frac{d\mathbf{v}}{dt} + (\mathbf{v} \cdot \nabla)\mathbf{v} \quad (1.9)$$

is the material derivative. In the solar context, the plasma pressure is related to the plasma density by the perfect gas law

$$p = \mathcal{R}\rho T, \quad (1.10)$$

where \mathcal{R} is the gas constant and T is the plasma temperature, which in turn is given by an energy equation.

It is often convenient to combine together Equations (1.3), (1.5) and (1.6) in order to eliminate \mathbf{E} and \mathbf{j} , resulting in the so-called induction equation

$$\frac{\partial \mathbf{B}}{\partial t} = \nabla \times (\mathbf{v} \times \mathbf{B}) + \eta \nabla^2 \mathbf{B}, \quad (1.11)$$

where η is the magnetic diffusivity, equal to $(\mu\sigma)^{-1}$. The equation of motion and the induction equation are essentially the two fundamental equations of MHD, determining the two primary variables \mathbf{v} and \mathbf{B} . By comparing the two terms on the right-hand side of the induction equation, the magnetic Reynolds number R_m may be defined as

$$R_m \sim \left| \frac{\nabla \times (\mathbf{v} \times \mathbf{B})}{\eta \nabla^2 \mathbf{B}} \right| \sim \frac{l_0 v_0}{\eta}, \quad (1.12)$$

where l_0 and v_0 are typical length and velocity scales.

When $R_m \gg 1$, the magnetic field is said to be “frozen into the plasma”, meaning that, whilst the plasma is free to move along magnetic field lines, plasma motions perpendicular to the magnetic field drag the field lines along with them. In this limit, the frozen-flux theorem of Alfvén holds, and so the plasma is perfectly conducting. This is the case nearly everywhere in the Sun's atmosphere.

However, when $R_m \ll 1$, the the magnetic field is governed by a diffusion equation, implying that field variations on a scale l_0 are destroyed over a time scale $t_0 = l_0^2/\eta$.

In the cases where $R_m \lesssim 1$, the plasma is free to move across field lines with different topological connections, which in turn may result in magnetic reconnection. Reconnection is the process by which field lines are broken and then reconnected in a different way. In two dimensions, reconnection can only occur at null points; however, in three dimensions, reconnection can occur both at null points and in the absence of null points

(Schindler et al., 1988; Hesse and Schindler, 1988; Lau and Finn, 1990).

1.3.1 Magnetohydrostatics

It is often convenient to use reduced forms of the MHD equations depending on the relative importance of all the forces acting within the region of interest. When the plasma flow speed is much less than the sound speed $(\gamma p_0/\rho_0)^{1/2}$ (here γ is the adiabatic constant), the Alfvén speed $B_0/(\mu\rho_0)^{1/2}$ and the gravitational free-fall speed $(2gl_0)^{1/2}$ collectively (here l_0 represents a vertical scale length), the result is magnetohydrostatic balance

$$\mathbf{0} = -\nabla p + \mathbf{j} \times \mathbf{B} + \rho\mathbf{g}, \quad (1.13)$$

between the pressure gradient, the Lorentz force and the gravitational force. Taking the ratio of the first two terms in Equation (1.13) gives the plasma beta

$$\beta = \left| \frac{-\nabla p}{\mathbf{j} \times \mathbf{B}} \right| \sim \frac{2\mu p_0}{B_0^2}, \quad (1.14)$$

where p_0 represents a typical value for the plasma pressure. Thus β is essentially a measure of the relative magnitudes of the plasma pressure and the magnetic pressure. Taking the ratio of the third and first terms in Equation (1.13) gives

$$\left| \frac{\rho\mathbf{g}}{-\nabla p} \right| \sim \frac{l_0}{H_0},$$

where H_0 is the pressure scale height. When $\beta \ll 1$ and $l_0 \ll H_0$, the plasma pressure gradient and gravity are dominated by the Lorentz force and Equation (1.13) becomes

$$\mathbf{j} \times \mathbf{B} = \mathbf{0}. \quad (1.15)$$

This is the so-called force-free assumption. Although a force-free approximation is invalid during highly dynamic events, such as the explosive phase of a flare, it is otherwise a good approximation to the field in the Sun's corona. One subtlety is that the electric current flows along magnetic field lines. Furthermore, since the electric field is given by Ampere's law, Equation (1.15) may be written as

$$\nabla \times \mathbf{B} = \alpha(\mathbf{r})\mathbf{B}, \quad (1.16)$$

where $\alpha(\mathbf{r})$ is some function of position. In general, $\alpha(\mathbf{r})$ is constant along each individual field line. However, choosing α to be the same constant along every field line results in the simpler *linear* or *constant- α* approximation. By choosing $\alpha = 0$ in particular, the so-called *current-free* (or *potential*) field is obtained.

1.4 Topology and the Potential Field Approximation

Throughout this thesis, much use will be made of potential fields in studying the statistical properties of the Sun's magnetic field. To do this, the field will be considered to be emanating from a series of point sources. In such an approximation, the charges are assumed to lie in a plane, and the corona is considered to be the region $z > 0$. Thus, if the field arises from n point sources at positions \mathbf{r}_i ($i = 1 \dots n$) and with strengths ϵ_i ($i = 1 \dots n$), then the magnetic field $\mathbf{B}(\mathbf{r})$ at a point $\mathbf{r} = x\hat{\mathbf{x}} + y\hat{\mathbf{y}} + z\hat{\mathbf{z}}$ is obtained using the point-source Poisson solution

$$\mathbf{B}(\mathbf{r}) = \sum_{i=1}^n \frac{\epsilon_i(\mathbf{r} - \mathbf{r}_i)}{|\mathbf{r} - \mathbf{r}_i|^3}. \quad (1.17)$$

Field lines may then be calculated by numerically solving

$$\frac{dl}{|\mathbf{B}|} = \frac{dx}{B_x} = \frac{dy}{B_y} = \frac{dz}{B_z}. \quad (1.18)$$

In this thesis, the integration of Equation (1.18) will be carried out using a fifth-order Runge-Kutta-Fehlberg method of integration with a self-adjusting step size.

Before continuing any further, though, it is worth stopping to ponder over the assumptions outlined above. Although the use of point sources appears at first to violate the solenoidal condition $\nabla \cdot \mathbf{B} = 0$, if each source is considered to represent a flux tube passing through the solar surface and spreading out into the overlying corona, then this simplification is allowable. Furthermore, although the Sun isn't flat, its curvature may be neglected when the area of the solar surface under consideration is sufficiently small.

The potential field approximation, in which no currents flow and the field therefore permits no stress, is more disputable. Certainly active regions, which are comprised of multifarious flux elements that have complex geometrical structure and are separated by distances less than present angular resolutions, give rise to complicated current systems that are poorly represented by potential field models. In the quiet Sun, though, such prob-

lems are less pronounced, as the current concentrations that build up in quiet-Sun regions are undoubtedly far less complex than those that are suggested by images of the corona above active regions. Indeed, it is believed that the magnetic field at sufficiently high altitudes in the corona (away from structures such as prominences) is close to potential (e.g. Longcope, 1996).

At present, any attempt to use a more elaborate method of construction than the potential field extrapolation requires a great deal of effort. Such studies are hampered by insufficient knowledge of boundary conditions (due in no small part to the fact that current magnetograms only view the photosphere from one fixed position, and so only record the longitudinal component of magnetic fields in all but the strongest of magnetic regions), and often require trying out several boundary conditions until the one that most closely matches the observed field is obtained. Moreover, the resulting fields are never unique and depend strongly upon observations of field structures which are highly instrument (i.e. temperature) dependent.

1.4.1 Representing Photospheric Fragments

When choosing to represent photospheric fragments by a series of point sources, there is a couple of ways in which one may proceed. Either several point sources may be clustered together to represent a single photospheric fragment (Chapter 2), or each individual point source may itself represent a single photospheric fragment (Chapters 3–6).

Each scenario has its own distinct advantages and disadvantages over the other (examined in Appendix A). When one wishes to extrapolate the field from an observed magnetogram, it is worthwhile to consider representing each fragment by a cluster of point sources. The number of sources in each fragment is then generally determined by the resolution of the magnetogram from which the field is being extrapolated, since a natural criterion for placing the sources is to put a single point source at the centre of each pixel. The strength of the point source is then determined by the intensity of the pixel (although pixels below a fixed threshold value are typically ignored, as they are indistinguishable from noise). In this way, the overall geometry of each fragment is conserved far more than it is when each fragment is represented by a single point source.

However, if one wishes to study the topology of a magnetic configuration, then representing each magnetic fragment by a series of point sources has some awkward disadvantages. As null points are crucial to the study of magnetic charge topology, the artificial null points that occur between sources within a fragment result in many artificial sepa-

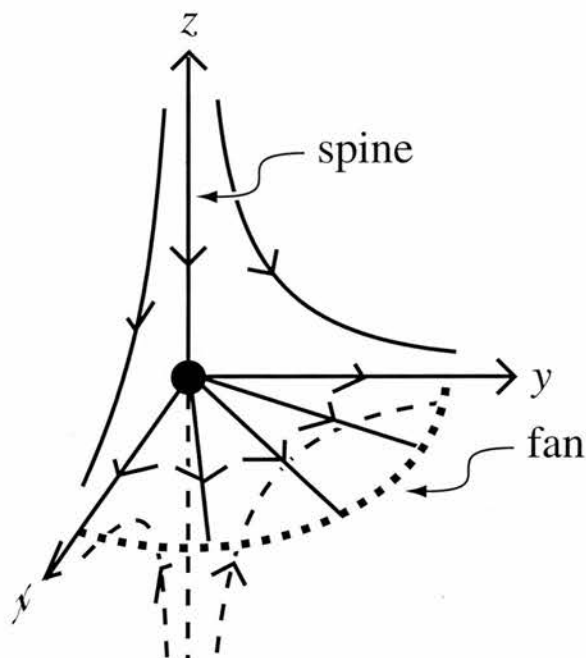


Figure 1.4: The structure of the field about a 3D null point. The null here is positive, with the spine field lines lying on the z -axis and directed towards the null point. Fan field lines are directed away from the null point and lie radially in the x - y plane.

rators and fan surfaces threading the corona. Although it has been realised recently that quiet-Sun fragments are likely to be comprised of many smaller magnetic flux elements, which would indeed lead to internal nulls within each fragment, it would be wrong to allow artificial nulls here when there is no observational evidence showing the structure of the sub-elements within a given magnetic flux fragment.

Instead, it is more convenient to treat each individual fragment as a single point source when studying magnetic charge topology. This allows for faster computations of the field, since there are fewer sources, whilst still retaining the main features of the overall field.

1.4.2 The Topological Skeleton

The topological skeleton of a magnetic field $\mathbf{B}(\mathbf{r})$ consists of sources, null points, separatrix surfaces (fans), spines and separators (Cowley, 1973; Priest et al., 1997). *Null points* are locations at which the magnetic field vanishes, the structure near a typical 3D null point being shown in Figure 1.4. Locally, in the region around the null, the magnetic field can be approximated by Taylor expanding the field $\mathbf{B}(\mathbf{r})$ and neglecting all the resulting terms except the linear ones. This linearised representation possesses three distinct eigenvalues that must sum to zero, given that $\nabla \cdot \mathbf{B} = 0$ (Fukao et al., 1975; Greene, 1988;

Parnell et al., 1996). Thus, if the degenerate case when an eigenvalue is zero is ignored, then it must hold that either two eigenvalues are positive (giving a so-called *positive* null), or two are negative (a *negative* null). The two similarly signed eigenvectors define a planar surface, termed the *fan plane*. Outwith the neighbourhood of the null, the field lines that originate in the fan plane form *separatrix surfaces*. The remaining eigenvector determines the direction of the two *spine field lines*, which terminate at the null point and are, in the case of potential nulls, normal to the fan plane. Fan field lines are oppositely directed to spine field lines, so that field lines entering the null along the spine leave via the fan plane (a positive null), and vice versa.

Photospheric nulls in potential fields may be either *upright* or *prone* (Beveridge et al., 2003). Upright nulls are defined as those nulls with their spine field lines normal to the photospheric surface, whilst prone nulls are defined as those with their spine field lines lying within the photospheric plane.

When two separatrix surfaces intersect, they form a topologically distinct feature called a *separator*, which joins two oppositely signed null points. Separatrix surfaces divide the volume into distinct regions, called *domains*, within which all the field lines connect the same pair of sources. Thus, separatrix surfaces provide the borders between domains.

1.5 Some Results and Theories

The motions of network elements force the coronal magnetic fields to interact in a complex way. Numerous theories predict dissipation of magnetic energy at null points (Dungey, 1958; Schindler et al., 1988), whilst other models predict energy dissipation along separators (Lau and Finn, 1990, 1996; Longcope, 1996, 1998; Priest and Titov, 1996; Galsgaard and Nordlund, 1997; Galsgaard et al., 2000). Recently, Galsgaard et al. (2000), Priest et al. (2002) and Mellor et al. (2004) also showed that dissipation may occur across separatrix surfaces. Priest et al. (2002) explored the formation and dissipation of current sheets on multiple separatrix surfaces (referred to as ‘flux-tube tectonics’) and their effect on coronal heating. They found that simple relative motions (rather than complex braiding) of separate flux sources produce current sheets along the separatrices, which then dissipate rapidly by fast reconnection or in a turbulent manner. However, there is very little observational evidence to show what roles each of these mechanisms play in determining the way in which the solar corona is heated.

Aside from investigating the physics of how the various mechanisms work, several statistical studies have attempted to quantify the density of null points present in the quiet Sun's atmosphere. Schrijver and Title (2002) studied the statistical properties of the connectivity of field lines representing the magnetic field in the solar atmosphere by analysing the potential field over a source plane randomly sprinkled with 300 magnetic point sources. By looking at 200 such realisations (in order to improve statistics), they found that each source connects to 1–12 opposite-polarity sources by field lines in the plane (typically 3–4), whilst the total number of opposite-polarity sources that a source is connected to by field lines both in and out of the plane ranges from 1 to 32, with an average of 8. They discovered a relation of approximately 1 null per source, with 91% lying in the source plane. One surprising result was that even the smallest sources frequently connect to many sources, with only a weak trend of stronger sources connecting to more sources. Despite the many connections, they found that 50% of the flux from a source connects to just one near source, 40% connects to another 2–6 near neighbours, and the remaining 10% connects to as many as 25 other sources.

This study was followed by Longcope et al. (2003) who derived an expression for the distribution of magnetic null points in potential magnetic fields and applied their results in numerical experiments which also accounted for the effects of varying degrees of flux imbalance. By considering 10 000 different model fields, each emanating from a random number of mixed-polarity sources scattered on a disk (typically ~ 300) and with strengths chosen from both uniform and exponential distributions in two separate runs, they found that the coronal density of null points in a given field is highly dependent on the degree of imbalance between positive and negative sources, with the greatest density of coronal nulls occurring when 20% of the sources are of the minority polarity.

In the $z = 0$ plane, one generally finds that prone nulls are far more common than upright nulls. Beveridge et al. (2003), found a density of 0.0018 ± 0.0007 upright nulls per charge for fields in perfect flux balance with an exponential distribution of source strengths (they also considered a uniform distribution of source strengths and obtained similar results). This density was found to increase exponentially as the flux imbalance increases, with the highest density of upright nulls occurring when all sources are of one polarity. This behaviour makes sense if one considers only the footprints of the field (the two dimensional regions formed by the intersection of a domain with the photospheric plane (Welsch and Longcope, 1999)). In the scenario where there are only positive sources, the footprint fan field lines have no negative sources to connect to, and so they must either terminate at upright nulls or connect to a balancing source at infinity.

1.6 Outline

Throughout this thesis, potential field models are used, often based on observed data, to deduce the properties of the Sun's magnetic carpet. These models typically consist of hundreds of magnetic flux fragments, from which statistical properties of the corona over the quiet Sun are obtained.

In the following chapter, the aim is to explore the geometric and connectivity characteristics of flux tubes in the quiet Sun. This is achieved by using data from magnetogram images taken by the MDI instrument on board SOHO as input to a potential field model. It is found that the coronal magnetic field over the quiet Sun, whilst generally being complex in character with many interconnections between fragments covering a broad range of sizes, is highly sensitive to local flux imbalances. Fragments are found to connect to numerous opposite-polarity fragments, with larger fragments generally having more connections. The origin of the flux at various heights is also examined, leading to the startling observation that even smaller fragments contribute to the field at higher altitudes. Chapter 2 is concluded with a summary of the main findings of the analysis, along with a detailed comparison with the study of Schrijver and Title (2002).

The next chapter, Chapter 3, explores the coronal magnetic field from a more topological viewpoint. It has previously been suggested by several authors (e.g. Lau and Finn, 1990; Longcope, 2001; Longcope and Klapper, 2002) that the coronal field is comprised of domains of only two types, namely isolated domains and separator-ring domains. After presenting an algorithm for tracing separator field lines, the remainder of the chapter examines the nature of both isolated and separator-ring domains, and categorises them further according to their geometry and topology.

The density of separators in mixed-polarity regions is examined in Chapter 4 by analysing magnetic fields arising from point sources that are distributed using a Monte Carlo experiment initially (the same method as used by Schrijver and Title (2002), in fact), and later by utilising observed data. It is found that they are more abundant than previously thought, as many nulls are found to be linked by more than one separator. It is also shown that they have a tendency to bunch together about the nulls and form trunks, similar to the findings of Beveridge et al. (2003) in the source plane. Connections between coronal nulls are then studied, with the conclusion that bifurcations in the corona, rather than those confined to the (highly symmetric) photospheric plane, may be quite common in practice.

Recycling times for the coronal field are obtained using MDI data in Chapter 5. This

involves initially isolating the effects on domain fluxes of emergence and cancellation of flux in the photosphere, for which a subtle method is devised. It is found that when the effects of emergence and cancellation are considered, the coronal flux is recycled in roughly 1/10th of the time taken to recycle the photospheric flux calculated by Hagenaar (2001). Indeed, by comparison with the amount of time taken to recycle all coronal flux when emergence and cancellation are prohibited, it becomes clear that a certain amount of reconnection occurs in reaction to emergence and cancellation of flux. An estimate of the currents required to be flowing along separators in order to give observed heating rates is then made.

Chapter 6 goes on to consider a model 2D translationally symmetric field in which the magnetic sources are subjected to shearing motions. An examination of the effects of complexity on the build-up of currents on separatrices is preceded by a simple 4-source example demonstrating the properties of simple shearing motions. It is then found that the amount of free energy built up by the shearing motions is dependent upon the number of sources through which a given quantity of flux emerges into the system, and also the spatial distribution of the sources. A simple comparison is also made between coronal heating due to separatrix currents and coronal heating due to separator currents by revisiting the four-source quadrupolar configuration mentioned previously.

A summary of the work presented in this thesis is given in Chapter 7, along with a discussion regarding its possible applications and extensions.

Chapter2

Statistical Flux-Tube Properties of 3D Magnetic-Carpet Fields[†]

夏	夢	蛸	A lobster in a pot
の	き	壺	Dreaming awhile
月	夢	や	Under the summer moon
松	を		
尾			
芭			
蕉			

MATSUO BASHO (1644–1694)

2.1 Introduction

One of the most important discoveries in the history of solar physics in recent times has been that of the so-called ‘magnetic carpet’. Where it had been previously thought that the Sun’s weak magnetic field away from active regions has a negligible influence on the outer atmosphere, early observations with SOHO’s Michelson Doppler Imager (MDI) provided a revolutionary insight into just how dynamic the quiet-Sun magnetic field really is.

Several studies, discussed in Chapter 1.2.1, have determined the various properties of quiet-Sun magnetic flux. Further studies (e.g. Domínguez Cerdeña et al., 2003) have recently shown that the field in intranetwork fragments is as strong as that in the larger network fragments that cluster in supergranular lanes. Thus, the main distinguishing factor between intranetwork fragments, with strengths $\sim 10^{16}$ – 10^{17} Mx, and network fragments,

[†]The work in this chapter was published in Vol. 212 of Solar Physics in February 2003 (Close et al., 2003).

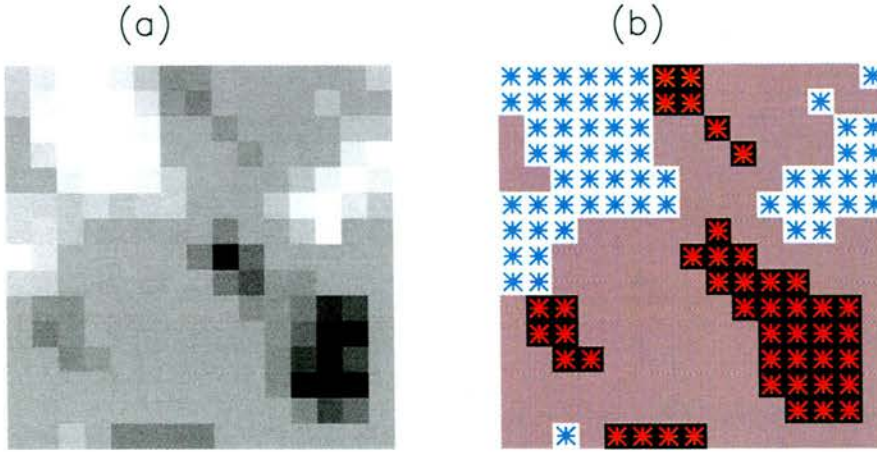


Figure 2.1: (a) Magnetogram image from the inner balanced region with noise removed. (b) Sketch of the point-source-per-pixel representation of the magnetogram. The blue stars are positive point sources and the red are negative.

with strengths ranging from 10^{18} Mx to 10^{19} Mx, is one of flux.

However, since the magnetic concentrations that abide in the quiet-Sun photosphere give rise to a web of intermingled magnetic flux tubes, a good statistical understanding of the magnetic field above the photosphere is needed in order to understand better the connection between the photospheric magnetic flux fragments and the coronal magnetic field. In this chapter, the nature of coronal flux tubes is studied.

In the following analysis, each photospheric magnetic fragment is represented by a series of point sources and the overlying potential field is analysed. A detailed explanation of how the field is represented is given in Section 2.2. Results are presented in three sections: Section 2.3 discusses properties of flux tubes, Section 2.4 details the connectivity between opposite-polarity fragments, and Section 2.5 examines how individual fragments influence the field at varying heights. Finally, Section 2.6 provides a discussion of the results.

2.2 Analysing the Magnetic Carpet

In order to study the properties of the magnetic carpet, high-resolution MDI magnetograms of the quiet Sun, observed near disk centre on 13th June 1998, are used. Before the analysis is performed, temporal noise in the data, which is largely due to 5-minute oscillations, is reduced by averaging over 9 magnetograms spaced by 1 minute. Furthermore, the resolution of the magnetogram is reduced by a factor of 2 in both the x and y directions by summing 2×2 groups of pixels. This helps reduce some of the spatial noise

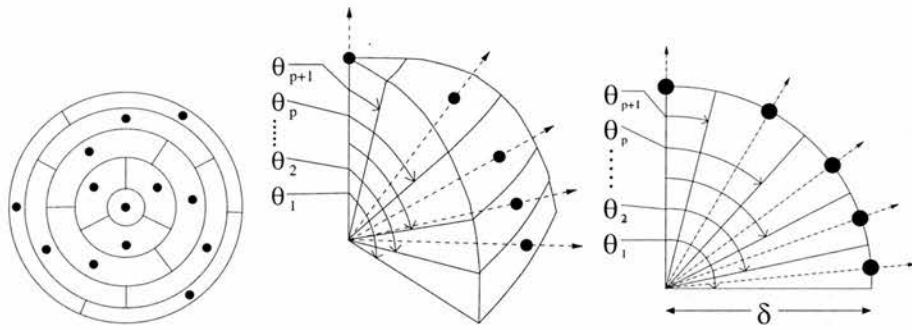


Figure 2.2: Example case showing starting points for $n = 13$; here $p = 4$ and $q = 3$, with one field line starting directly above the source.

in the magnetogram.

To obtain information about the spectrum of flux tubes in the magnetic carpet, the flux in a magnetogram is represented by a series of point sources. Each macropixel with an absolute flux over 20 Mx cm^{-2} is represented by a point source, which is placed in its centre (as discussed in Subsection 1.4.1). The flux of each source is set equal to the flux in the pixel it represents. Figure 2.1 shows a representation of a section of the magnetogram and the positions of the point sources used. In order to consider the effects of choosing different regions with varying net flux, only a section of the magnetogram is used in the analysis; two subregions are specially selected to give preferred scenarios. In each case, a square, 300×300 macropixels in area, is selected with the subsequent analysis performed on a smaller inner square of just 100×100 macropixels so as to reduce greatly the bias of edge effects.

To calculate the field lines, a potential field is used, as discussed in Section 1.4. Although the field below the upper chromosphere is not force-free, much less current-free, a potential field model is used for simplicity.

Field lines are calculated from starting points very close to the sources. Which sources are integrated from and how many field lines are calculated from each source is discussed later. Starting points for field lines are positioned on a hemisphere of radius δ centred on each source, where for a minimum source separation γ , say, it holds that $\delta \ll \gamma$.

If there are n field lines per source, then the hemisphere is split into p rings, with q segments per ring. This can be done in two ways such that there is always one field line positioned directly above the source and $n = pq + 1$ (Figure 2.2), or $n = pq$, such that no field line is started directly above the source (Figure 2.3).

Each starting point is calculated in such a way that each segment has the same area. In the case shown in Figure 2.2, where there is a field line directly above the source, the

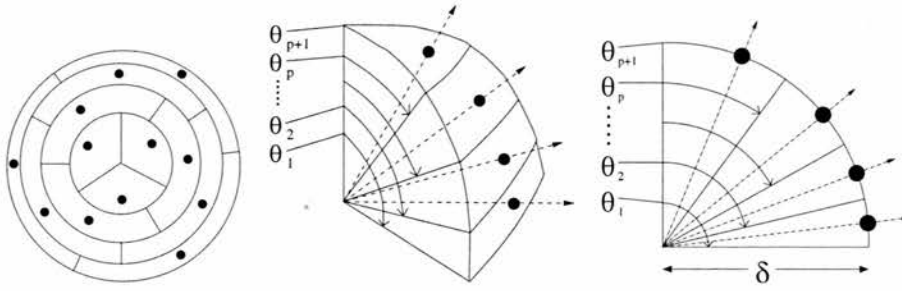


Figure 2.3: Example case showing starting points for $n = 12$; here $p = 4$ and $q = 3$, with no field line starting directly above the source.

angles shown in the figure are given by

$$\theta_1 = \frac{\pi}{2}, \quad (2.1)$$

$$\theta_2 = \cos^{-1} \left(\frac{q}{1 + pq} \right), \quad (2.2)$$

$$\theta_i = \cos^{-1} ((i - 1) \cos \theta_2), \quad 2 < i \leq p, \quad (2.3)$$

$$\theta_{p+1} = \cos^{-1} (p \cos \theta_2), \quad (2.4)$$

whereas when there is no field line directly above the source (Figure 2.3), the angles are

$$\theta_1 = \frac{\pi}{2}, \quad (2.5)$$

$$\theta_2 = \cos^{-1} \left(\frac{1}{p} \right), \quad (2.6)$$

$$\theta_i = \cos^{-1} ((i - 1) \cos \theta_2), \quad 2 < i \leq p, \quad (2.7)$$

$$\theta_{p+1} = 0. \quad (2.8)$$

In both cases, the angle ψ_i that the field line makes with respect to the vertical, with $\theta_{i+1} > \psi_i > \theta_i$, is given by

$$\psi_i = \cos^{-1} \left(\frac{1}{2} [\cos(\theta_{i+1}) + \cos(\theta_i)] \right). \quad (2.9)$$

For $n \geq 5$, the variables p and q are chosen such that the expression $p - q \geq 0$ is minimised. (For $1 \leq n \leq 4$, the value of p is fixed at one). This also determines whether or not there will be a field line situated directly above the source. Each ring is offset from the one below it by an angle $2\pi/(pq)$ so as to obtain a larger range in the directions in which the field lines point.

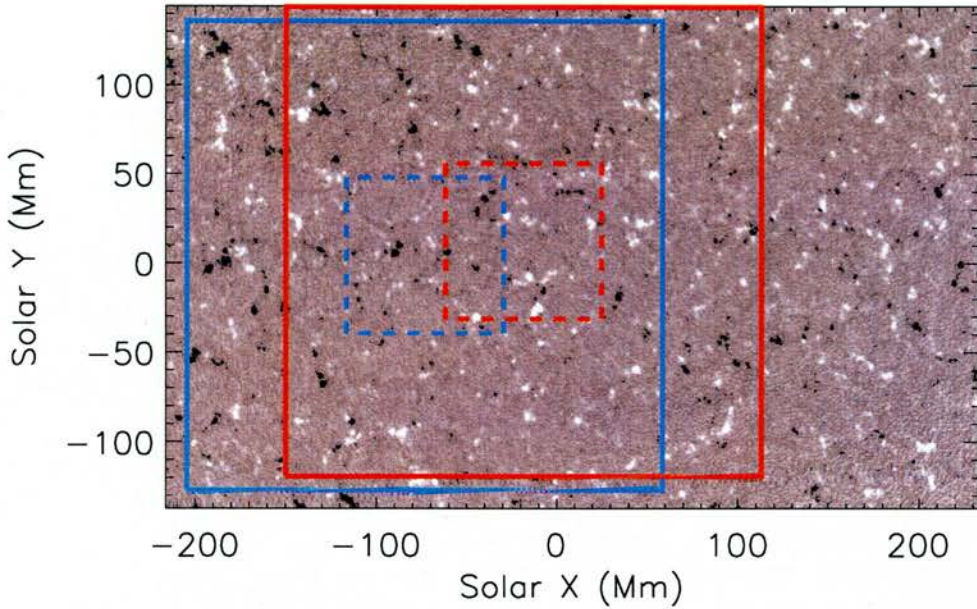


Figure 2.4: High-resolution MDI magnetogram of the quiet-Sun photosphere, taken on 13th June 1998. The red solid-line box with the interior dashed-line box indicates the balanced region studied. The blue solid-line box with the interior dashed line box indicates the unbalanced region.

2.3 Flux-Tube Characteristics

Two different regions, of size 300×300 macropixels (264×264 Mm), are picked from the full magnetogram, as shown in Figure 2.4, and the inner 100×100 (88×88 Mm) area is studied. The first region has a roughly balanced inner area (an exact flux balance is difficult to find), whereas the second region has a strong imbalance, with the ratio of positive flux to negative flux equal to 0.48 in the inner area. In both cases the entire flux inside the larger square is roughly balanced. The height of the domain in which the field lines are calculated is set at 264 Mm, equal to the horizontal size of the outer region.

For each of the two regions, m field lines are traced from each positive source of strength ϵ above 1.55×10^{17} Mx ($20 \text{ Mx cm}^{-2} \times \text{area of macropixel}$), with m equal to the integer part of ϵ/ϵ_1 (where $\epsilon_1 = 7.73 \times 10^{15}$ Mx = $1 \text{ Mx cm}^{-2} \times \text{area of macropixel}$), so that each field line represents the same amount of flux. This means that from each source 20 field lines are traced at minimum. For each field line calculated, it is assumed that all the flux within the area it represents behaves in the same way. This is not strictly true, but, provided $\min(\epsilon) \gg \epsilon_1$, i.e., there are many field lines per source, it is a plausible assumption. Since in any continuous field a flux tube may be defined as being the surface made up of field lines that pass through a given curve, it is reasonable to refer to these field lines as flux tubes. Thus, the continuous coronal field is split into a set of magnetic flux tubes that each have flux ϵ_1 – hence, from a source of strength $\epsilon = 30\epsilon_1$, say, there

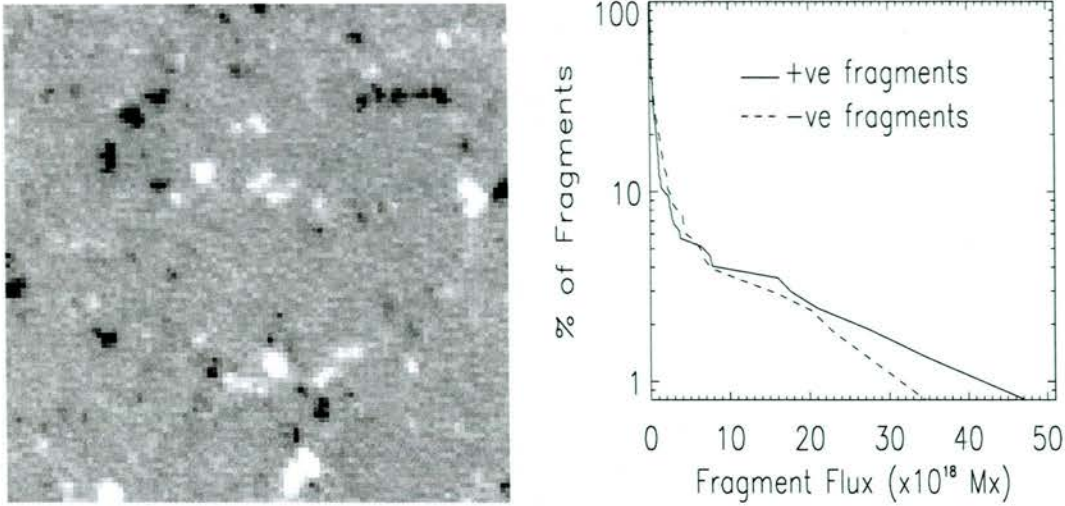


Figure 2.5: To the left is the magnetogram image of the balanced 88×88 Mm inner region that is studied. To the right, the percentage of fragments with flux over a given value is shown. The dashed line represents fragments with negative flux whilst the solid line represents fragments with positive flux.

would start 30 such flux tubes. Since field lines are allowed to leave the inner region, the distribution of lengths of field lines from both the polarities will not necessarily be the same, and so the process is repeated for field lines linking to the negative sources.

For each flux tube calculated, information is stored about (i) its footpoints, (ii) the strength of the fragments at these footpoints, (iii) the position of its maximum height and (iv) its total length. For a random subset of the total number of flux tubes calculated, the coordinates of points along each flux tube are stored to produce field line plots. The results obtained from the flux tubes are then compared in order to deduce various properties of the magnetic carpet (Sections 2.3.1, 2.3.2 and 2.5).

In order to determine the connectivity of the region (discussed in Section 2.4), discrete fragments in the magnetogram are considered and information about the fragment to which each pixel belongs is stored and used to create connectivity matrices for the fragments of each polarity. Flux tubes that leave the domain through either the top or the outer sides are flagged and subsequently discarded in the analysis. Those that leave the inner box are followed to their footpoints in the outer region.

In the following discussion, flux tubes that have been traced from positive fragments are referred to as ‘positive’ flux tubes, whilst those flux tubes traced from negative fragments are called ‘negative’ flux tubes.

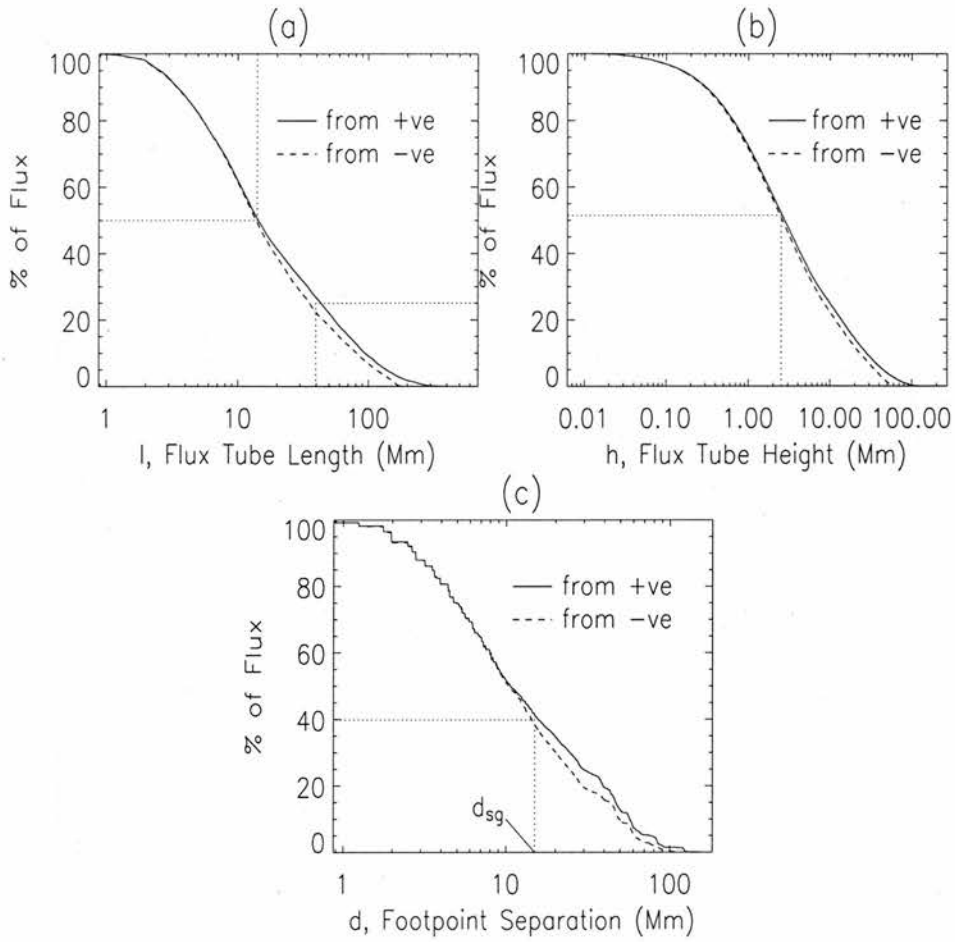


Figure 2.6: Percentage of flux tubes with (a) length greater than l , (b) height greater than h and (c) endpoint separation greater than d . In all three plots the solid lines represent positive flux tubes and the dashed lines represent negative flux tubes. Specific values are indicated by dotted lines, and d_{sg} indicates the diameter (14 Mm) of a typical supergranule cell.

2.3.1 A Balanced Inner Region

Within the balanced inner region (shown in Figure 2.5) there are 185 positive fragments which are represented by 816 point sources and 190 negative fragments represented by 802 point sources. The distribution of the strengths of these fragments is also shown in Figure 2.5 (right). For a given flux (x -axis), the y -axis gives the percentage of fragments with flux equal to or above this value. The total net flux is 24.5×10^{18} Mx in the inner region, corresponding to a mean field of 0.3 G, compared to the total absolute flux of 629×10^{18} Mx and total absolute mean field of 8.1 G. In the whole 300×300 macropixel region there are 2359 positive fragments represented by 7229 point sources and 1991 negative fragments represented by 7927 point sources.

The percentage of flux tubes with length greater than l is plotted in Figure 2.6(a)

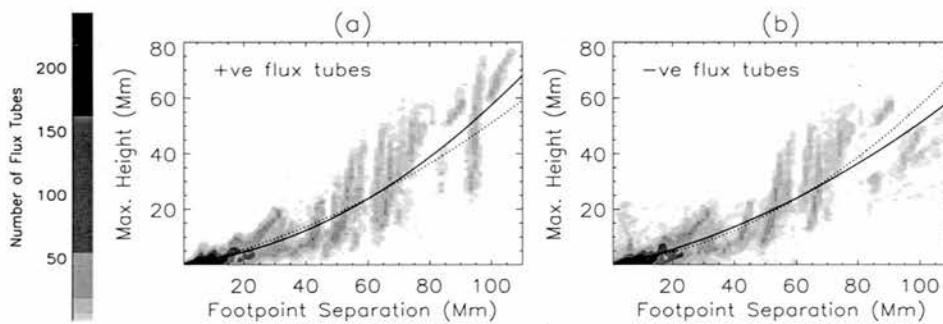


Figure 2.7: Contour plot of footpoint separation versus flux tube height for (a) positive flux tubes and (b) negative flux tubes. The lowest contour level is 1, with each subsequent contour level at 3 times the previous one. The solid line indicates the line fitted to the data in the plot and the dotted line is the line fitted to the data from the opposite polarity.

against length on a logarithmic axis. The dotted lines show that for flux tubes of both polarities, 50% are less than 14 Mm, whilst 25% are more than 35 Mm in length. Close inspection shows a mean flux tube length of around 35 Mm for the positive fragments and around 29 Mm for the negative fragments. This implies that the majority of flux from one quiet-Sun fragment closes within 1 or 2 supergranular cells. The two distributions are very similar, which is what one would expect for a balanced region. There is, however, a slight imbalance of flux in the region towards the positive polarity; the ratio of total positive flux to total negative flux is 1.08. This imbalance affects mostly the tubes of longer length, with the maximum positive flux tube length being far greater than the maximum negative flux tube length. Flux tubes with lengths up to 623.4 Mm are found by starting above positive fragments, whilst flux tubes of up to only 184.5 Mm can be traced back from negative fragments.

Naturally, some fragments, particularly those near the edge of the inner region, will be expected to connect to fragments outside the inner region. Here 21.7% of the positive flux from the inner region connects to the outer region, whilst 15.4% of the negative flux from the inner region connects to the outer region (7.5% of positive flux must connect outside the inner region due to the imbalance in flux).

Only 0.02% of flux tubes from positive fragments hit the upper boundary and only 0.02% hit the sides. None of the negative flux tubes hit the outer boundaries. It is not known whether these flux tubes represent genuine open flux or whether they would eventually connect to negative fragments in the absence of a boundary.

Another property of magnetic-carpet flux tubes worth investigating is their distribution of heights above the source plane. Figure 2.6(b) shows the percentage of flux tubes with maximum heights greater than h , against height. The field is modelled as a potential field

for simplicity, which fails near the photosphere (where gravitational effects enter) and sufficiently high in the corona (where inertial and pressure effects come into play), and also when there are Alfvénic plasma speeds or large enough currents present. Assuming the chromosphere to be of width 2.5 Mm (and accepting that taking the chromosphere and corona to be discretely separate layers is a naive assumption), it is found that 48% of the photospheric flux closes low down near the coronal base in the present approximation. Hence, only 52% of the total photospheric flux appears to reach into the corona for both positive and negative flux. Flux tubes from both polarities reach similar heights, with a mean height reached by the positive flux tubes of 9.5 Mm and a mean height for the negative flux tubes of 7.5 Mm. However, the maximum height reached by the closed positive flux tubes is 229.9 Mm, some four times higher than reached by the negative flux tubes, which is 59.5 Mm. This difference in maximum heights for the two polarities is due to the slight flux imbalance within the region.

Figure 2.6(c) shows a plot of the percentage of flux tubes with footpoints separated by more than a distance d . Around 41% of the flux from the positive concentrations extends over 14 Mm, the mean diameter of a typical supergranular cell (Hagenaar et al., 1997). If the larger ‘classical’ supergranular diameter of 32 Mm is considered Simon and Leighton (1964), then only 24% of the positive flux extends farther than this. These figures are similar for the negative concentrations, where it is found that 38% extend farther than 14 Mm and 19% farther than 32 Mm.

Figure 2.7 shows contour plots of footpoint separation against flux tube height for flux tubes of both polarities. It is clear, by merely glancing at the plots, that the maximum height of a flux tube increases as the footpoint separation is increased, which one would expect. Both plots have quadratic curves fitted to them, although the two curves vary quite significantly. This is mostly due to the slight imbalance within the region. The quadratic fitted to data for positive flux tubes has equation $0.0045d^2 + 0.12d + 0.4$, whilst for negative flux tubes the equation is $0.0023d^2 + 0.25d + 0.51$. These curves demonstrate that the relation between the footpoint separation and the maximum height of the flux tubes is not a linear one.

2.3.2 An Unbalanced Inner Region

To consider the effect of an unbalanced region of flux on the characteristics of potential flux tubes, a second region is investigated (shown in Figure 2.4). For a given flux, the percentage of fragments with flux equal to or above this value is shown in Figure 2.8.

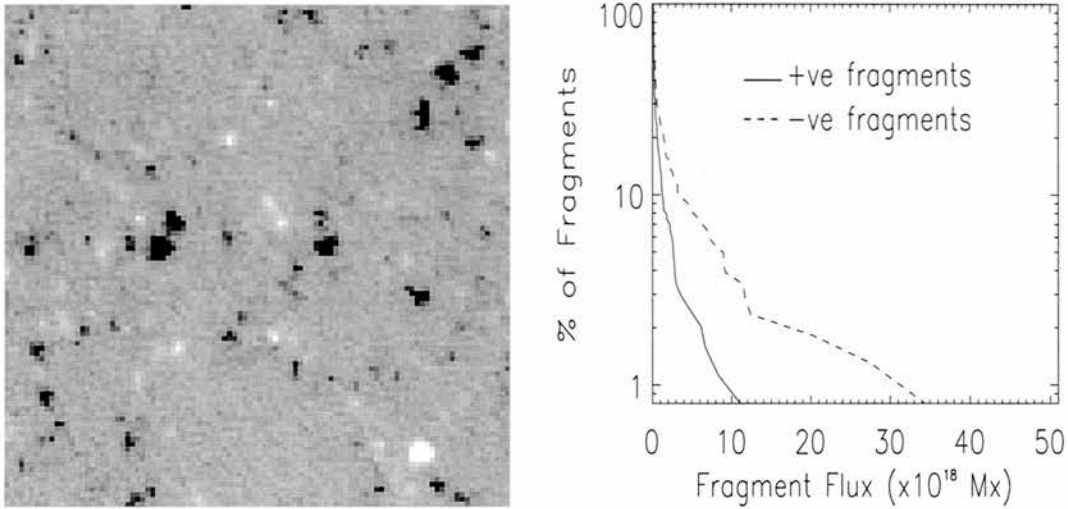


Figure 2.8: To the left is the magnetogram image of the unbalanced 100×100 macropixel (88×88 Mm) inner region studied. To the right, the percentage of fragments with flux over a given value is shown. The dashed line represents sources with negative strength whilst the dotted line represents sources with positive flux.

Here the net flux is -186.5×10^{18} Mx in the inner region, corresponding to a mean field of -2.4 G, and there is roughly twice as much negative flux as positive flux. The total absolute flux is 526×10^{18} Mx, with a total absolute mean field of 6.8 G.

Within the unbalanced inner region studied here (shown in Figure 2.8), there are 222 positive fragments, represented by 608 point sources, and 192 negative fragments, represented by 930 point sources. The distribution of the strengths of these fragments is also shown in Figure 2.8. In the whole 300×300 macropixel region, 2450 positive fragments are represented by 7543 point sources and 2019 negative fragments are represented by 8491 point sources. The analysis in the previous subsection is repeated for this unbalanced region.

Again, the percentage of flux tubes with lengths greater than l are plotted against length, (Figure 2.9(a)), with the x -axis logarithmic. The figure shows a substantial difference in the distributions of lengths of flux tubes from the two polarities for all flux tube lengths. As expected, flux tubes from the dominant (negative) polarity are generally longer than those from the minority (positive) polarity. The dotted lines show that for the positive flux tubes, 50% are longer than 9 Mm, whereas the negative flux tubes are generally longer with more than 70% having lengths of over 9 Mm and 50% with lengths over 23 Mm. For the positive flux tubes, 25% are over 17 Mm in length, whilst over 56% of negative flux tubes are over this length. Here the mean length of the positive flux tubes is only 15 Mm, whereas the mean length of the negative flux tubes is 55 Mm. This large difference in mean flux tube length is due to the flux imbalance in the inner region

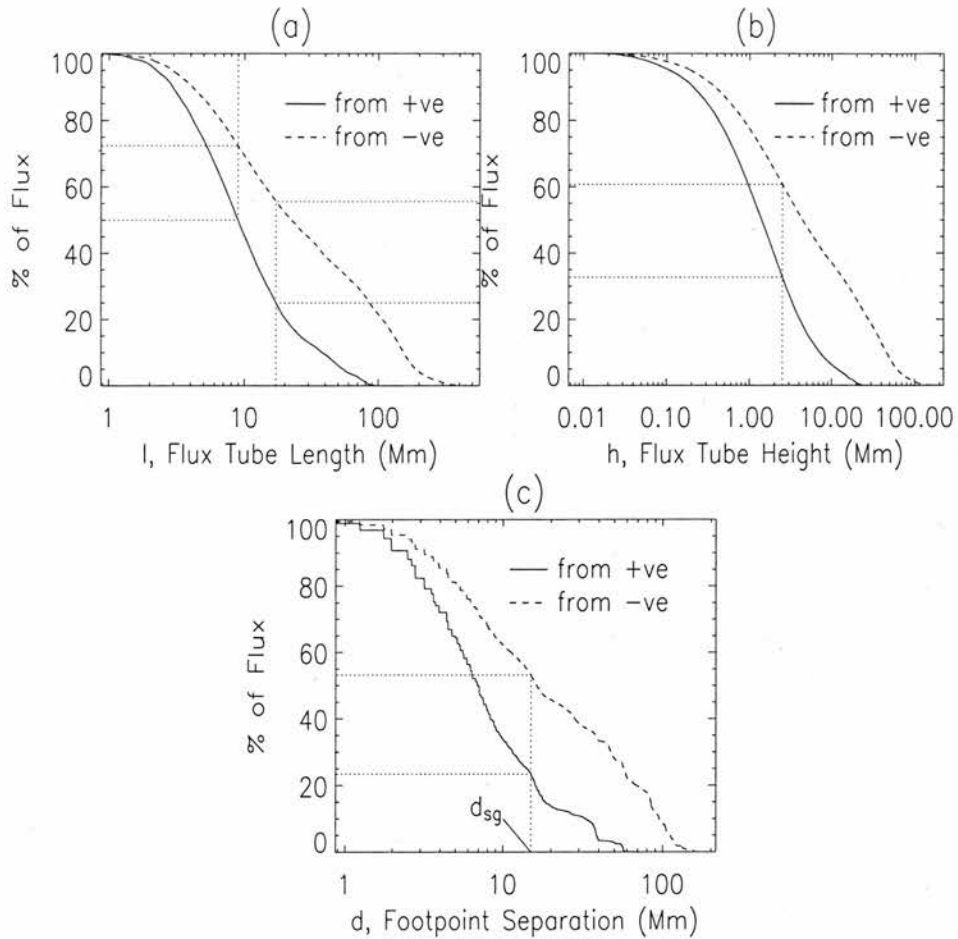


Figure 2.9: Percentage of flux tubes with (a) lengths greater than l , (b) heights greater than h and (c) footpoint separations greater than d . In all three plots the solid line represents flux tubes started from positive sources and the dashed line represents those started from negative sources. Specific values are indicated by dotted lines, and d_{sg} indicates the diameter of a typical supergranule cell.

(positive/negative flux ≈ 0.48), which results in much of the negative flux connecting to fragments outwith the inner area. The maximum length of the positive flux tubes is 100 Mm, whereas the maximum length of the negative flux tubes is far greater at 499 Mm. Here it is found that only 3.4% of the positive flux connects to fragments outside the inner region, whereas this figure is 54.0% for negative fragments. This is not surprising, since 52.4% of the negative flux from the inner area *must* connect to the outer region as a consequence of the flux imbalance. Of all the field lines calculated, none from the positive fragments nor the negative fragments in the inner region hit the outer boundaries.

For this region, it is found that the mean height reached by flux tubes from the positive fragments is 2.8 Mm, with a maximum height reached of 24.2 Mm. In contrast, flux tubes from negative fragments have a mean height of 15 Mm and a maximum height reached of 183 Mm. This is clearly illustrated in the plots showing the distribution of flux tube

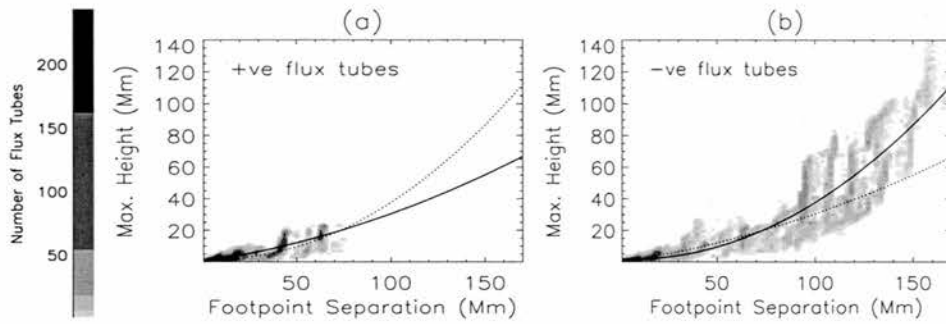


Figure 2.10: Contour plot of footpoint separation versus flux tube height for (a) positive flux tubes and (b) negative flux tubes. The lowest contour level is 1, with each subsequent contour level at 3 times the previous one. The solid line indicates the line fitted to the data in the plot and the dashed line represents the opposite-polarity flux tubes.

heights in Figure 2.9(b). Taking the chromosphere to be of width ~ 2.5 Mm, and bearing in mind the assumptions concerning the validity of this model previously discussed for the balanced region, results in 33% of flux tubes from positive fragments reaching coronal heights, whereas for flux tubes from negative fragments this figure is almost double at 61%.

Around 23% of the flux from the positive fragments extends out farther than the 14 Mm diameter of a typical supergranular cell. More than double that, 53%, of flux from negative fragments extends farther than this length. However, taking the diameter of a supergranule to be 32 Mm results in values of 10% and 37%, respectively, of the positive and negative flux tubes extending farther than a supergranule (Figure 2.9(c)).

Figure 2.10 shows slightly different behaviour for the flux tubes in the unbalanced region than in the balanced region shown in Figure 2.7. It is still generally true that the larger the footpoint separation, the greater the maximum height of the flux tube. However, now the curves fitted to the data vary much more, although this is likely to be because the range of footpoint separations and maximum heights is much smaller for the positive flux tubes than the negative flux tubes. The quadratics now have equations $0.0013d^2 + 0.18d + 0.03$ for the positive flux tubes and $0.004d^2 - 0.061d + 2.1$ for negative flux tubes. The negative quadratic appears to be a reasonable fit to the positive data and so the imbalance does not appear to have changed the relation between footpoint separation and maximum height of the flux tubes. These curves again show that the relationship between footpoint separation and flux tube height cannot be assumed to be a linear one.

The contrast in flux tube lengths obtained for this imbalanced region compared to the previous balanced region demonstrates that the flux tube length spectrum for a given region is highly dependent on the flux balance within that region. It is most likely that

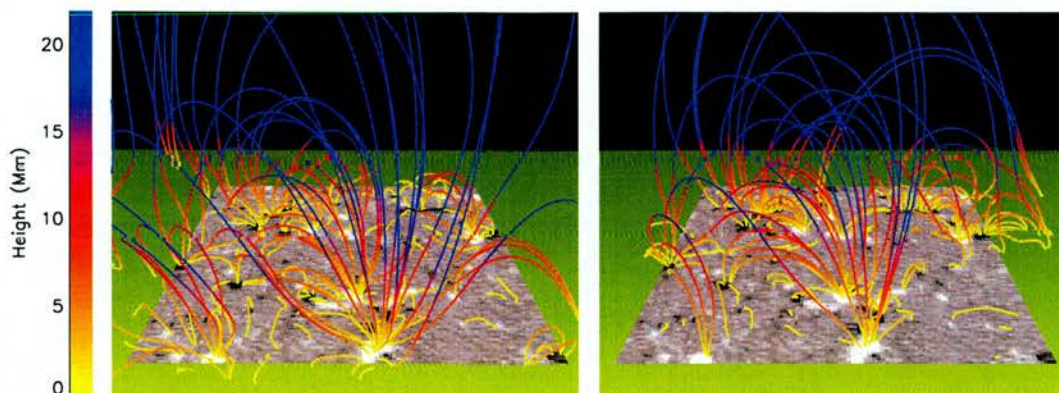


Figure 2.11: Magnetogram of the balanced region together with a subset of the field lines calculated from the positive sources (*left*) and the negative sources (*right*). Animations showing 3D rotational views about these configurations are provided on the accompanying CD (see Appendix F for details on how to access them).

longer flux tubes than those found here may be obtained in other regions observed within quiet-Sun areas, although, as the size of the region examined is increased, the maximum possible imbalance will decrease. In a given region there will be areas that have a greater local imbalance than others, so that the maximum flux tube length possible from fragments within a region will depend on the balance between the size of the flux imbalance and the area over which the imbalance occurs.

2.4 Connectivity

Having looked at the characteristics of flux tubes themselves, now the individual fragments and their connections are considered. By considering adjacent macropixels of the same polarity to be a fragment, matrices of the connectivity from each fragment are calculated and connectivity properties are thus deduced. In the following discussion, the connections of an individual positive fragment to a series of negative fragments are termed ‘positive’ connections, while those from an individual negative fragment to positive fragments are termed ‘negative’.

2.4.1 Balanced Region

For the balanced region studied, the field line plots in Figure 2.11 show fairly similar behaviour for the flux tubes from both the positive fragments and the negative fragments. The flux tubes in both plots are comparable in length, with roughly the same number of

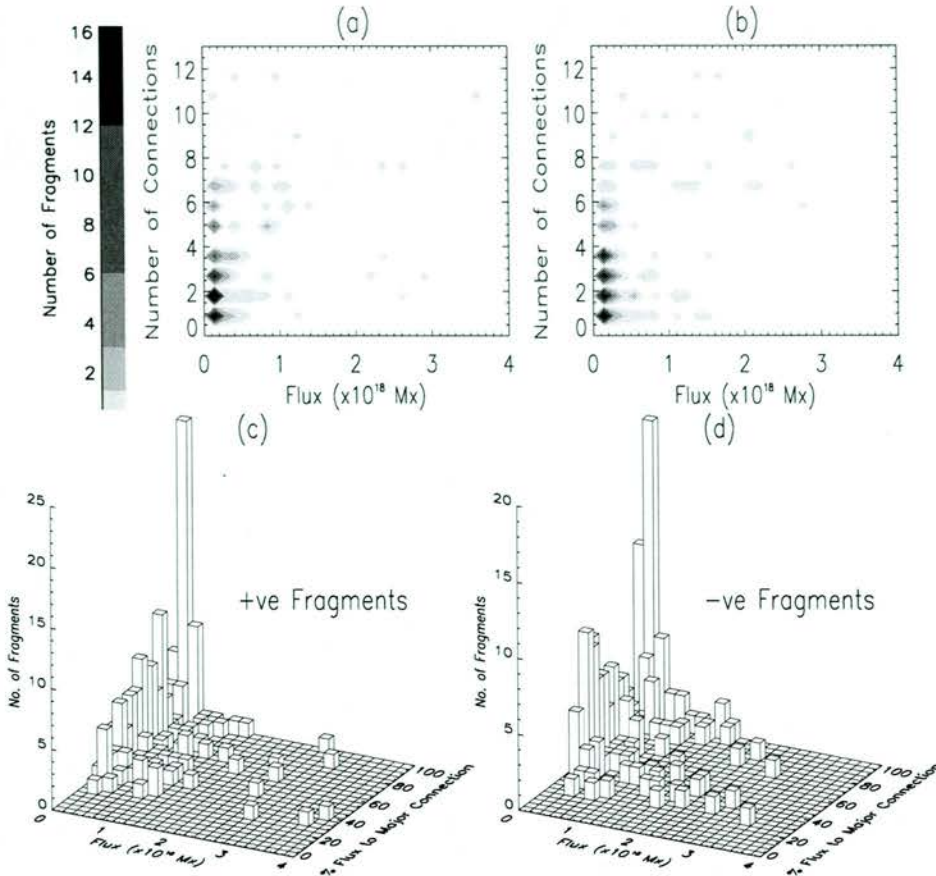


Figure 2.12: Contour plots showing the number of fragments to which a fragment of given flux connects for (a) positive fragments and (b) negative fragments. The lowest contour level is 1, with each subsequent contour level set at twice the previous one. Also shown are 3D bar graphs of fragment flux versus percentage flux to major connection for (c) positive fragments and (d) negative fragments.

flux tubes connecting outwith the inner region in both cases.

The maximum number of positive connections is 65, whilst the maximum number of negative connections is 38. For fragments of both polarities the mean number of connections is ~ 5 . Figures 2.12(a) and (b) show that connectivity for fragments of both polarities is similar, with many small fragments ($\text{flux} < 10^{18}$) having 1–7 connections. There is a slight trend for larger fragments to have more connections, although there is much scatter in the plots. Figures 2.12(c) and (d) show that the flux from the smaller fragments of both polarities often connects almost entirely to a single opposite-polarity fragment. In some cases, though, as little as 20% of the flux from the smallest of fragments connects to a single fragment. This implies a minimum of 5 connections from such fragments. Figure 2.13(a) shows that the 10% of positive fragments with the most connections have 8 connections or more, whilst the largest 10% of negative fragments have 10 connections or more. In Figure 2.13(b), each set of opposite-polarity fragments that are connected to

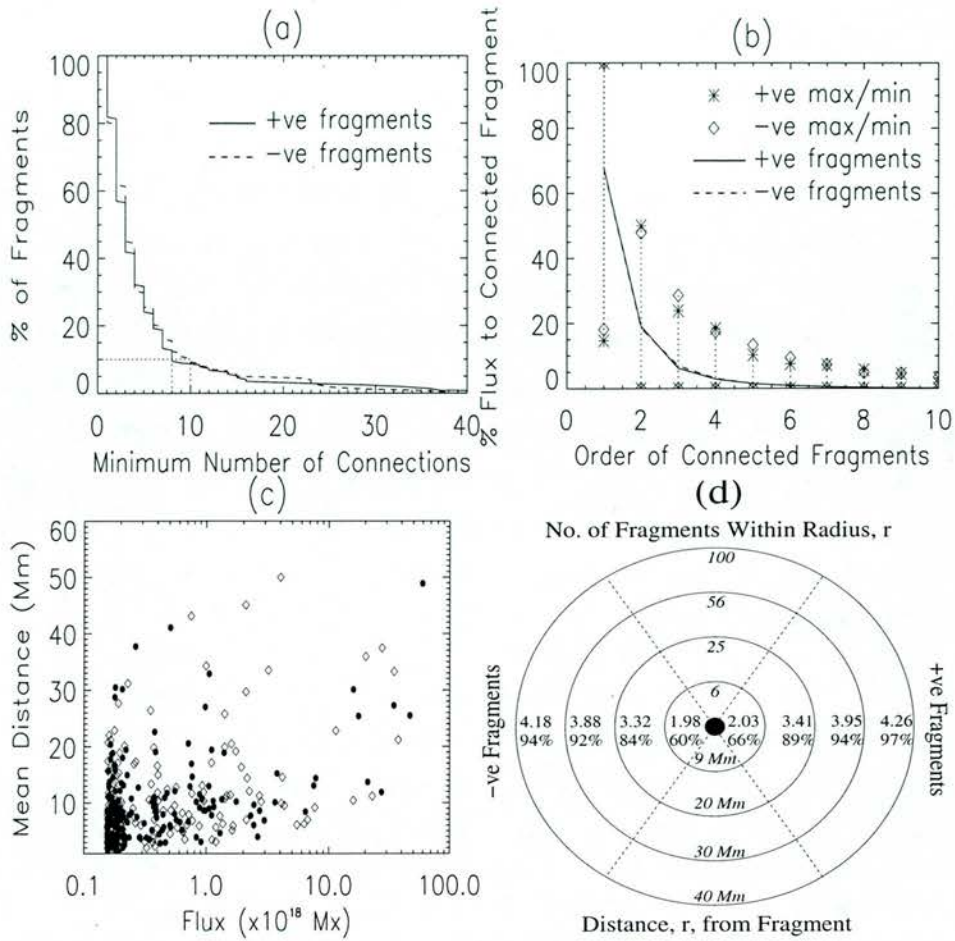


Figure 2.13: (a) Percentage of fragments against minimum number of connections of that fragment. (b) Mean proportion of flux for each fragment to which a given fragment connects. (c) Scatter plot of fragment flux versus the mean of the distances to connected fragments for positive fragments (filled circles) and negative fragments (diamonds). (d) Diagram showing distribution of flux and connections for both a typical negative fragment (left) and a typical positive fragment (right), against radius, r . The percentages show, as an average, the total amount of closed flux within a given radius, whilst the numbers show the average number of connected fragments within the given radius. The figure giving the number of fragments within a radius only includes those of the opposite polarity.

a single fragment are sorted in decreasing order with respect to the amount of connected flux. The stars (diamonds) denote the range of possible amounts of flux connected for the various positive (negative) fragments. The solid (dashed) lines give the mean flux connected to each fragment, again for the positive (negative) fragments. The two lines almost lie upon one another. From this it can be seen that the mean flux linked to the first (major) connection is 68% for both polarities. However, the range of possible flux connected is large, ranging from 15–100%. Up to 25% of the remaining flux connects to another 1–2 fragments, while the remaining 7% of flux connects to up to as many as 62 fragments for positive fragments and 34 fragments for negative ones (only the first 10

fragments are shown in Figure 2.13(b)).

The scatter plot in Figure 2.13(c) shows that, for a given fragment, the mean distance to connected opposite-polarity fragments is largely independent of the fragment flux. Smaller fragments connect, on average, to fragments distributed over a wide range of distances. However, as the fragment flux is increased, this range decreases, with the largest fragments connecting mostly to opposite-polarity fragments at relatively large distances. There is, perhaps unsurprisingly, a tendency for fragments to connect preferentially to their nearest neighbours. Indeed, 60–66% of flux closes, on average, within 9 Mm of a fragment. Although there is an average of ~ 2 connected fragments within this radius, the figures indicated suggest (by comparison with Figure 2.13(d)) that the connection with the second largest amount of flux does not necessarily lie within 9 Mm of the fragment in question. For this balanced region, the plots for both polarities of fragments are essentially the same.

Schrijver and Title (2002) found that strong fragments could connect to over 30 other opposite polarity fragments and, using an expectation value of one fragment per area of order $A \sim 2 \times 10^8 \text{ km}^2$ (Schrijver et al., 1997), they estimated that direct connections fanned out over a radius of order $r = (30 * 2 * \frac{A}{\pi})^{\frac{1}{2}} \sim 60 \text{ Mm}$.

The expectation value found here is one fragment per area of $A \sim 1.6 \times 10^7 \text{ km}^2$. Using this value, an estimate of the number of fragments within reach of a particular positive (negative) fragment is given by $I_n \pi r^2 / A$ ($I_p \pi r^2 / A$), where I_n (I_p) is the ratio of the total negative (positive) flux to the total flux of both polarities and r is the distance over which direct connections occur. This is essentially the inverse of the calculation by Schrijver and Title (2002).

The positive flux tubes have a mean footpoint separation of 22 Mm, so on average, taking I_n to be 0.48, the flux from a typical fragment extends out over an area containing ~ 44 fragments. For the maximum footpoint separation of 156 Mm, this figure is 2297 fragments. For negative fragments, with I_p equal to 0.52 and a mean footpoint separation of 19 Mm, flux extends out over an area containing ~ 36 fragments. For the maximum endpoint separation of 118 Mm, this figure is 1411 fragments. For such numbers of connections to be observed, this would require that (i) the field is sufficiently sampled and (ii) there are enough opposite-polarity fragments to provide the connections. Here, 7672 flux tubes are traced from the largest positive fragment and 4818 from the largest negative fragment, which is indeed enough to show up all the connections. Although there are 2359 positive fragments in the whole region, which is enough to provide the connections for the negative fragments, there are only 1991 negative fragments. Thus,

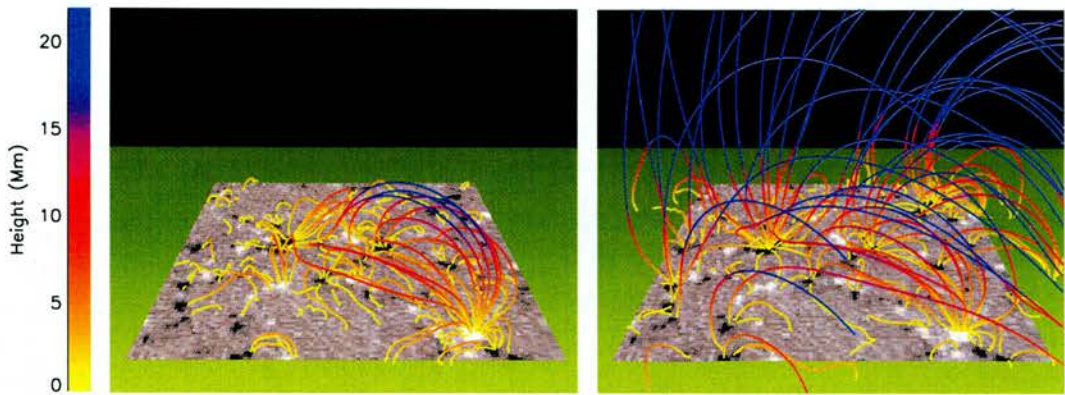


Figure 2.14: Magnetogram of the unbalanced region together with a subset of the field lines calculated from the positive sources (*left*) and the negative sources (*right*). Animations showing 3D rotational views about these configurations are also provided on the accompanying CD.

the maximum is 1991 connections for the largest positive fragment. Since the values for the number of connections found are much lower than these estimates, this indicates that fragments do not connect to all the fragments within their dome of influence. Indeed, it is likely that they are not situated in the centres of their dome of influence, but rather near the edge, and so assuming a full circle around the fragments is unrealistic.

2.4.2 Unbalanced Region

The contrast between the two field line plots in Figure 2.14 for the unbalanced region demonstrate how the flux from the negative fragments dominates the field. As a result of the imbalance of flux in favour of the negative polarity, many of the negative flux tubes must close outwith the inner region, which is clearly shown. Hardly any positive flux tubes close outwith the inner region, which is also reflected in the plot.

From the positive fragments there are at most 38 connections, with a mean of 3.7 connections. For the negative fragments, these values are roughly double, with a maximum number of connections of 75 and a mean of 6.7 connections. The contour plots in Figures 2.15(a) and (b) further emphasise this difference, showing clearly that negative fragments tend to have substantially more connections. There is again a definite trend for stronger fragments of both polarities to have more connections, whilst many of the fragments of strength less than 10^{18} Mx have 1–5 connections. Figures 2.15(c) and (d) show again that the bulk of the flux from a single fragment frequently connects to only a few other fragments. It is mostly the larger fragments that have their flux distributed more evenly over a greater number of sources. Figure 2.16(a) shows that the distribution of connections for fragments of the two polarities differ greatly. The 10% of positive fragments with

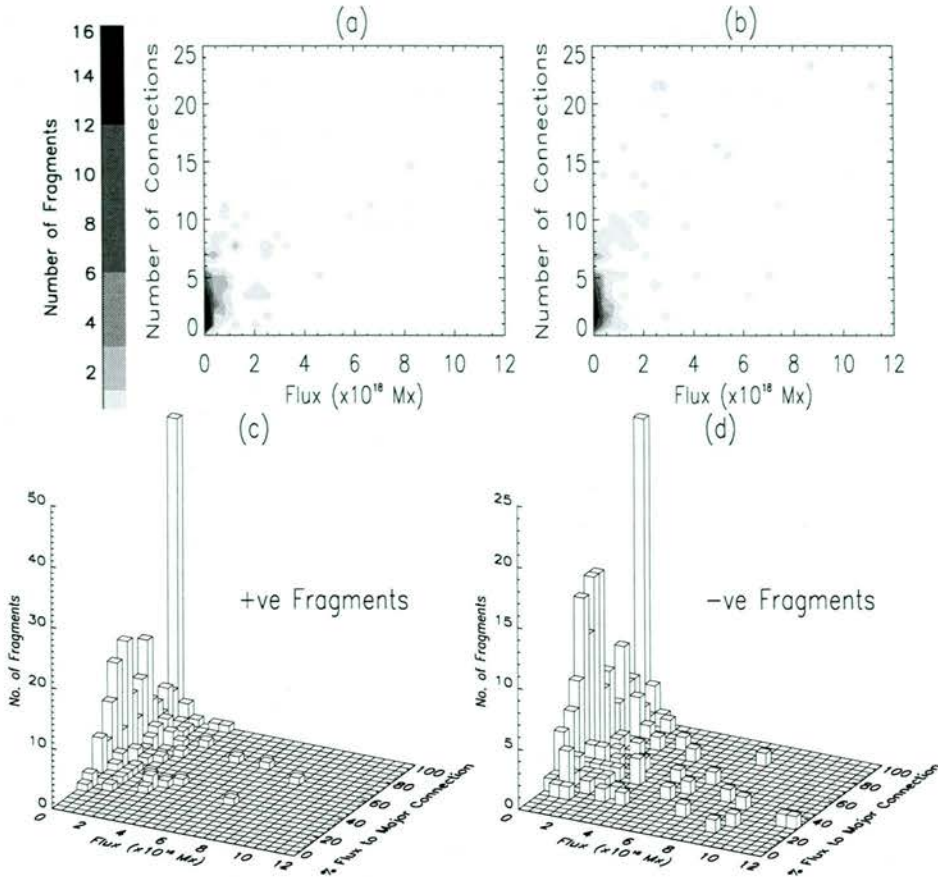


Figure 2.15: Contour plots showing the number of fragments to which a fragment of given flux connects for (a) positive fragments and (b) negative fragments. The lowest contour level is 1, with each subsequent contour level set at twice the previous one. Also shown are 3D bar graphs of fragment flux versus percentage flux to major connection for (c) positive fragments and (d) negative fragments.

most connections have a minimum of 7 connections or more, whereas for the negative fragments the top 10% with the most connections have 17 connections or more. This demonstrates that the dominant polarity in an unbalanced region has more connections than the minority polarity, as one would expect. Despite this, however, Figure 2.16(b) shows that the mean flux to the major connection for both polarities lies at around 65%, with up to 27% of flux connecting to another 1 or 2 fragments and the remaining $\sim 8\%$ of flux connecting to up to a possible 34 further fragments for the positive fragments and 71 fragments for the negative fragments.

For a given fragment, the mean distance to connected fragments is again effectively independent of the fragment flux (Figure 2.16(c)). The positive (minority) polarity fragments connect on average to negative fragments over a shorter range than the negative fragments. There is much evidence from Figure 2.16(d) for both polarities suggesting that a fragment connects preferentially to its nearest neighbours. 59–69% of flux closes,

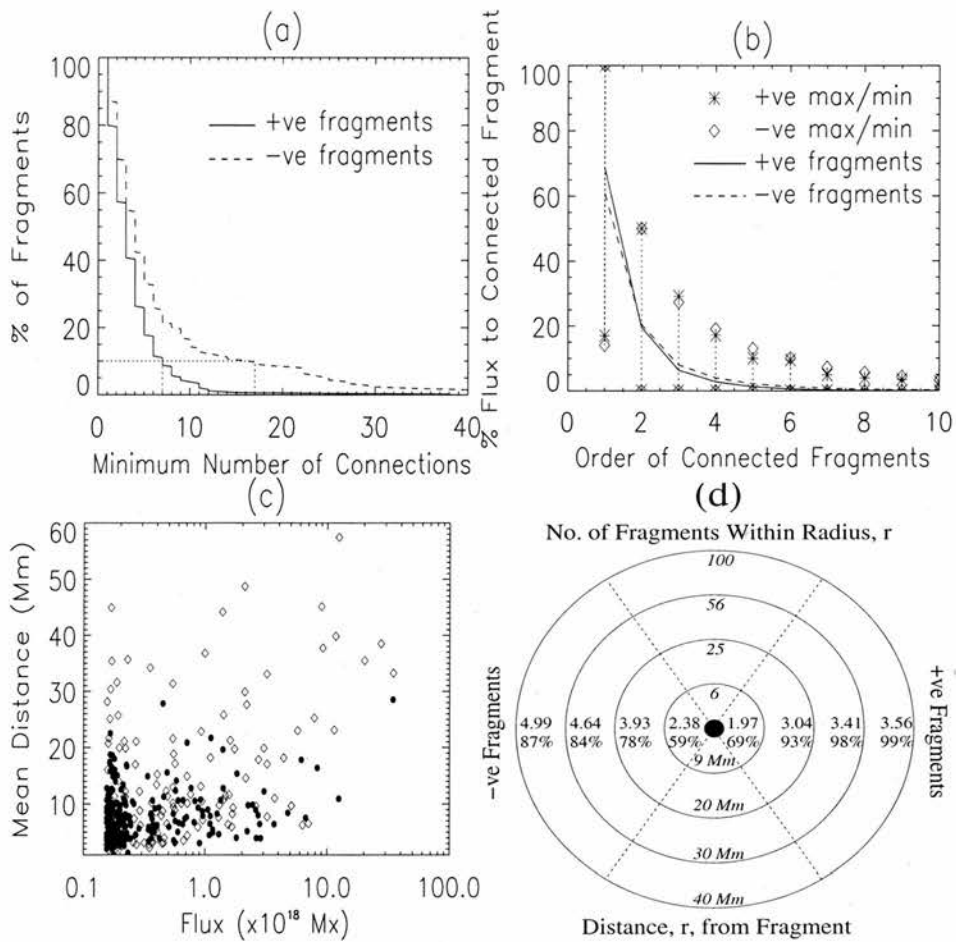


Figure 2.16: (a) Percentage of fragments against minimum number of connections from that fragment. (b) Mean proportion of flux for each fragment to which a given fragment connects. (c) Scatter plot of fragment flux versus the mean of the distances to connected fragments for positive fragments (filled circles) and negative fragments (diamonds). (d) Diagram showing distribution of flux and connections for both a typical negative fragment (left) and a typical positive fragment (right), against radius, r . The percentages show, as an average, the total amount of closed flux within a given radius, whilst the numbers show the average number of connected fragments within the given radius. The figure giving the number of fragments within a radius only includes those of the opposite polarity.

on average, within 9 Mm of a fragment. Again, the figures shown suggest that the connection with the second largest amount of flux does not necessarily lie within 9 Mm of the fragment in question.

2.5 Properties of Fragments

So far the distribution of flux tube heights above the source plane has been described, so now the attention is turned to the properties of the fragments that produce these flux

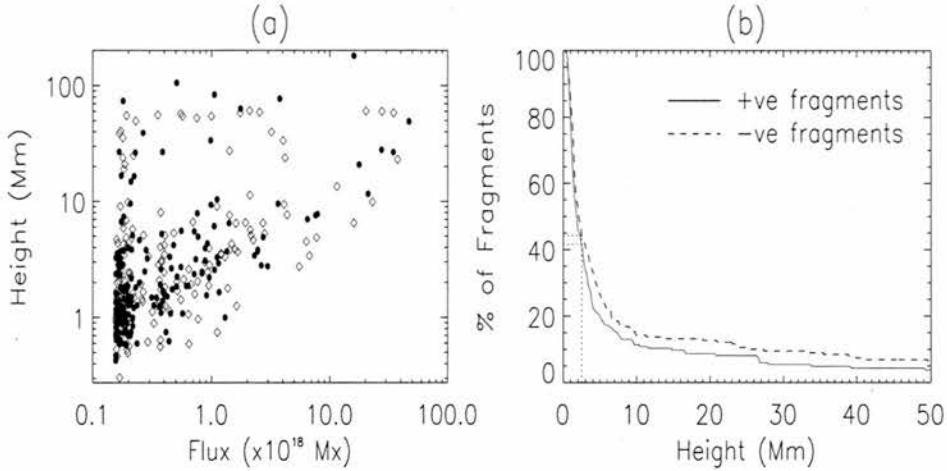


Figure 2.17: (a) Scatter plots showing fragment flux versus maximum height reached by flux from that fragment for positive fragments (filled circles) and negative fragments (diamonds). (b) Plot showing, for a given height, the percentage of fragments with flux reaching that height (or higher).

tubes. Although one might expect only the larger fragments to contribute flux to the field at larger heights, it is found instead that at a given height the field is comprised of flux from fragments over a wide range of sizes.

2.5.1 Balanced Region

The scatter plot in Figure 2.17(a) shows the maximum heights reached by flux from fragments of both polarities. The behaviour is similar for both positive and negative fragments; only the flux from smaller fragments closes entirely at low heights, although many small fragments have some proportion of their flux reaching relatively large heights. The fact that in the lower-right triangle of the plot there are no points means that larger fragments will always have some of their flux reaching the larger heights. Figure 2.17(b) shows that the 52% of flux from fragments of both polarities that reaches coronal heights (i.e. above 2.5 Mm) is produced by around 43% of the fragments. Thus, flux from 57% of all fragments does not reach the corona. Fragments that close entirely under 2.5 Mm are small (under 2×10^{18} Mx), each accounting for under 1% of the total unsigned flux within the region.

2.5.2 Unbalanced Region

The graph in Figure 2.18 showing the maximum heights reached by flux from fragments of both polarities in the unbalanced region displays the same characteristics as fragments

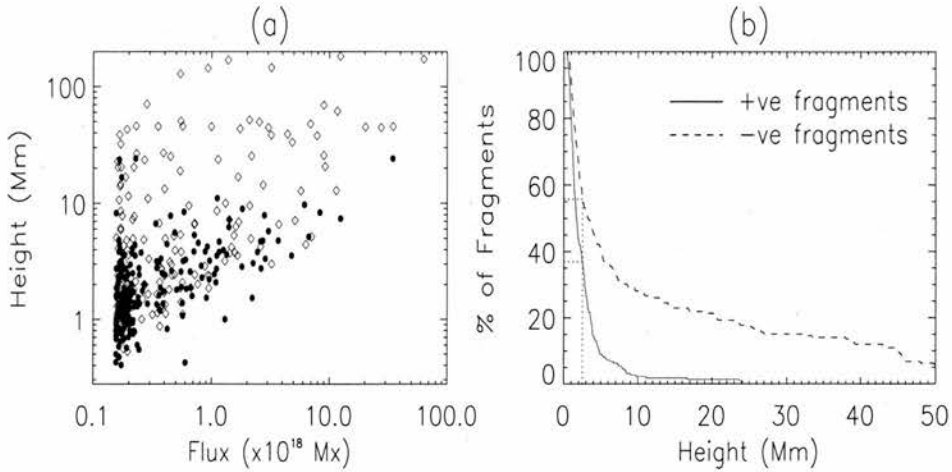


Figure 2.18: (a) Scatter plots showing fragment flux versus maximum height reached by flux from that fragment for positive fragments (filled circles) and negative fragments (diamonds). (b) Plot showing, for a given height, the percentage of fragments with flux reaching that height (or higher).

in the balanced region, with the figures adjusted accordingly (since positive flux tubes reach a mean height of only 2.8 Mm compared to 24.2 Mm for negative flux tubes). Again, only the flux from the smaller fragments may close entirely at relatively low heights, with larger fragments always having some proportion of their flux reaching larger heights. Figure 2.18(b) shows that the 61% of negative flux that reaches a height of 2.5 Mm or over is produced by 56% of the negative fragments, whilst the 33% of positive flux that exceeds this height is produced by 37% of the positive fragments. Positive fragments whose entire flux closes below 2.5 Mm have flux under 3×10^{18} Mx (less than 2% of the total positive flux in the inner region), whilst negative fragments whose entire flux closes below 2.5 Mm have flux less than 10^{18} Mx (less than 1% of the total negative flux).

2.6 Conclusions

This study of flux tube characteristics and fragment connections from an MDI magnetogram represented by a series of point sources (for each pixel over 20 G) and extrapolated into the corona using a potential field has revealed several interesting properties. The distribution of lengths of flux tubes determined by examining both the flux that leaves the positive fragments and the flux that closes down on the negative fragments is highly dependent on the total flux imbalance within the region of interest. Any flux imbalance will be mainly noticeable at the higher end of the distributions for both polarities. Even the quiet-Sun regions studied here are found to produce flux tubes that are 100 Mm long. Indeed, roughly 10% of the flux in both cases is contained in such loops. Furthermore,

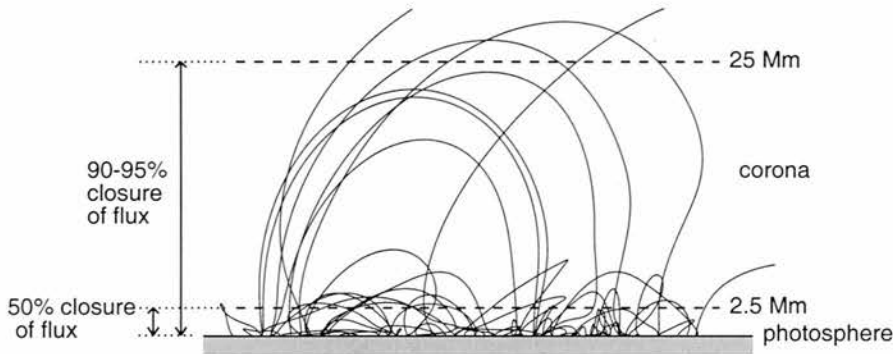


Figure 2.19: Side view of a typical 3D magnetic carpet field: 50% of flux closes below 2.5 Mm, whilst 5–10% of flux extends above 25 Mm.

it is found that much of the flux from the quiet Sun is contained in low-lying flux tubes. This means that only 50% of the flux that threads the surface of the Sun extends further than 2.5 Mm above the surface and only 5–10% extends further than 25 Mm, as shown in Figure 2.19. Thus, assuming a minimum coronal height of 2.5 Mm, all these low-lying loops never reach the corona. Hence, the magnetic field strength in the corona does not just fall off as $1/R^3$ in accordance with the expansion of the volume into which it is extending, but it falls off much faster due to the closure of magnetic field at lower heights. Analysis of the footpoint separation of the flux tubes shows that about 15% of the total flux connects to fragments that are within 5 Mm of each other. That is, they are connected to fragments that are probably in the same supergranular lane as themselves.

Typically 50% of the fragments contribute flux to the field above 2.5 Mm. Fragments whose entire flux closes below this height are small (flux $< 2 \times 10^{18}$ Mx), although many smaller sources have some of their flux reaching larger heights. Larger fragments, in contrast, will always have some of their flux reaching relatively large heights.

For a balanced region, similar positive fragments and negative fragments will have, on average, the same number of connections. Here a mean of 5 connections per fragment was found. For an unbalanced region, fragments of the dominant polarity will have more connections, on average, than those from the minority polarity. Here the total flux of both polarities varied by a factor of ~ 2 , and fragments of the dominant polarity had around twice as many connections, approximately 7, as the minority-polarity concentrations.

Despite the fact that flux from a particular fragment may be expected to extend out over an area containing many opposite-polarity fragments, the results obtained here show that the majority of these will not connect to the fragment in question. There are two reasons for this. Firstly, the estimates in this study assume that a fragment is situated in the centre of its dome of influence, whereas in practice it is more likely to be situated

nearer the edges. Indeed, the area over which flux from a given fragment extends is also highly unlikely to be circular. Secondly, many fragments within the area often connect entirely to other fragments. Thus, when calculating the field, the contribution from such fragments will cancel with the flux from the fragments to which it connects, resulting in many neighbouring fragments being effectively 'hidden' from the given source. So, despite the multitude of fragments, many features of the topology of a field produced by a small set of sources will be present here. The field produced by the many quiet-Sun fragments may be considered, to a certain extent, to be made up of a superposition of the fields produced by many low-order systems of only a small number of fragments.

The connectivity analysis performed here is in good agreement with the results obtained by Schrijver and Title (2002). Both studies show, in particular, that:

1. Although there is a trend, which shows up in all cases studied here, for stronger fragments to be connected to more opposite-polarity fragments, there is at any fragment strength a wide range of possible connections. Even the smallest fragments can have up to 7 connections, and the largest fragments can have between 10 and 60 connections.
2. Fragments show, perhaps unsurprisingly, a preference towards connecting to nearby opposite-polarity fragments. On average, roughly 60–70% of flux from a given fragment connects to an opposite-polarity fragment within a 9 Mm radius. However, some connections may span several supergranular diameters.
3. Despite the vast number of possible connections, the bulk of the flux from a typical fragment is here found to be divided such that (i) 60–70% connects to one opposite-polarity fragment (ii) 25–30% goes to a further 1 to 2 opposite-polarity fragments and (iii) any remaining flux may connect to as many as another 50 or more other opposite-polarity fragments. The figures obtained by Schrijver and Title (2002) are (i) 50% of flux goes to the major connection (ii) 40% goes to another 2–6 near fragments and (iii) the remaining 10% may connect to up to 25 further fragments.
4. There is evidence for nesting of isolated flux domains, bounded entirely by the fan surface from a single null point. Schrijver and Title (2002) observe this directly, whereas in this study it is inferred from knowledge that some fragments only connect to one opposite-polarity fragment.

Differences in exact figures will be due to the different methods of modelling the quiet-Sun photospheric fragments.

From this study it can be seen that potential field extrapolation and knowledge of connectivity within a region may provide useful information as to which fragments are related to events observed higher up in the solar atmosphere.

Chapter 3

A Categorisation of the Building Blocks of Coronal Magnetic Fields

夢	兵	夏	Summer grasses...
の	と	草	Traces of dreams
跡	も	や	Of ancient warriors
	か		

松尾芭蕉

MATSUO BASHO (1644–1694)

3.1 Introduction

The previous chapter demonstrated how the quiet-Sun magnetic flux that pierces through the photospheric surface in many discrete fragments is subsequently tangled up into complex regions of interconnecting flux. This in turn gives rise to a wide variety of interesting topological features. Thus, in order to capture something of the complexity of such fields, three-dimensional models need to include information concerning the topology of the magnetic field.

Up until a few years ago, relatively little was known of the topologies possible in three dimensional fields. However, much recent work has gone into classifying the configurations that arise from simple point-source potential-field models, and how some states may bifurcate into other states. In these models, the photospheric fragments are approximated by point sources and the resulting coronal field has no current. Such studies of the configurations arising from a handful of sources have proven very fruitful. Brown and Priest (1999b), for example, completely classified the topological behaviour resulting

from three sources, whilst Beveridge et al. (2002) explored the topologies possible with two dipoles. Other topological studies include Inverarity and Priest (1999), Longcope (1996), and Bungey et al. (1996). These studies have provided a greater understanding as to what might be expected as higher-order systems are considered.

As configurations with a greater and greater number of sources are considered, however, complete classification of the possible topological configurations becomes impractical. Thus, perhaps a better way of understanding such fields would be to look at the general properties of the domains themselves. This is what is investigated here.

In Section 3.2, the two fundamental building blocks of three-dimensional potential fields are introduced. The following section, Section 3.3, presents an algorithm for locating and tracing separator curves. Section 3.4 then considers a magnetic field extrapolated from observed data; after applying the topological equations of Longcope and Klapper (2002), the properties of photospheric domains and coronal domains are examined. A description of the domain structures associated with upright nulls is then given in Section 3.5, followed by a concluding discussion in Section 3.6.

3.2 Two Key Building Blocks of 3D Fields

Previous work by Lau and Finn (1990), Longcope (2001) and Longcope and Klapper (2002) has suggested that complex coronal configurations are made up of only two structurally stable building blocks, namely:

(i) an isolated domain, bounded by a single, unbroken fan surface such that all the fan field lines connect to a single source. Figure 3.1 shows how all the field lines from a small source on the right are bounded by a separatrix in the shape of a dome on which lie both a null point and a large source.

(ii) a separator-ring domain, bounded by fan sectors from several fan surfaces (a fan sector is a section of a fan surface for which all of the field lines connect to a common source). Figure 3.2 shows a pair of separatrix cones, one with a positive source at its apex, the other with a negative source at its apex. The two cones join along a closed curve of separators. This type of domain generally receives the most attention, since separators are believed to be important sites for reconnection (see discussion in Section 1.5).

It is worth noting here that during a bifurcation, such as the global separator bifurcation with two dipoles (Beveridge et al., 2002), where a domain of the second type changes to a domain of the first type (i.e. when going from from an intersecting state to a detached

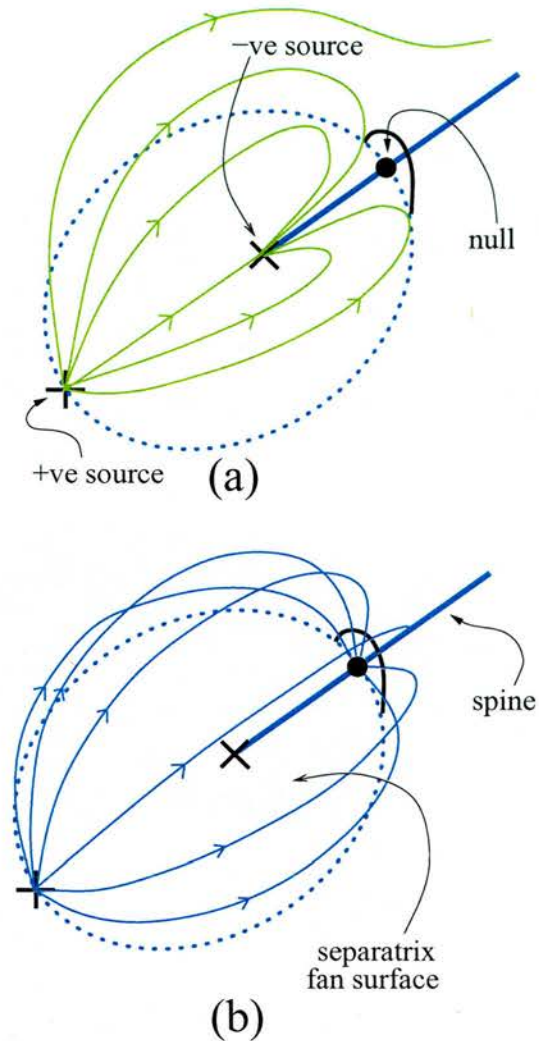


Figure 3.1: An isolated domain. A selection of field lines is shown in (a), and field lines lying in the separatrix surface are shown in (b).

state or vice-versa), a third, structurally unstable type of domain may be obtained. This domain is bounded by the fan surface from only one null, which is unbroken but for one curve in the $z = 0$ plane, where a spine field line and a planar separator make up part of the bounding surface, as shown in Figure 3.3.

Domain structures may be categorised further, however. For example, some of the domains that are encircled by a closed circuit of separators require the use of the symmetry in the $z = 0$ plane and the resultant mirror corona to complete the circuit ('photospheric' domains (alternatively known as planar domains)), whilst others may have their engirdling ring of separators entirely above the $z = 0$ plane ('coronal' domains). In order to address these points, an algorithm is presented in the next section for tracing separator curves. This is an absolute necessity for identifying individual domains. The subsequent

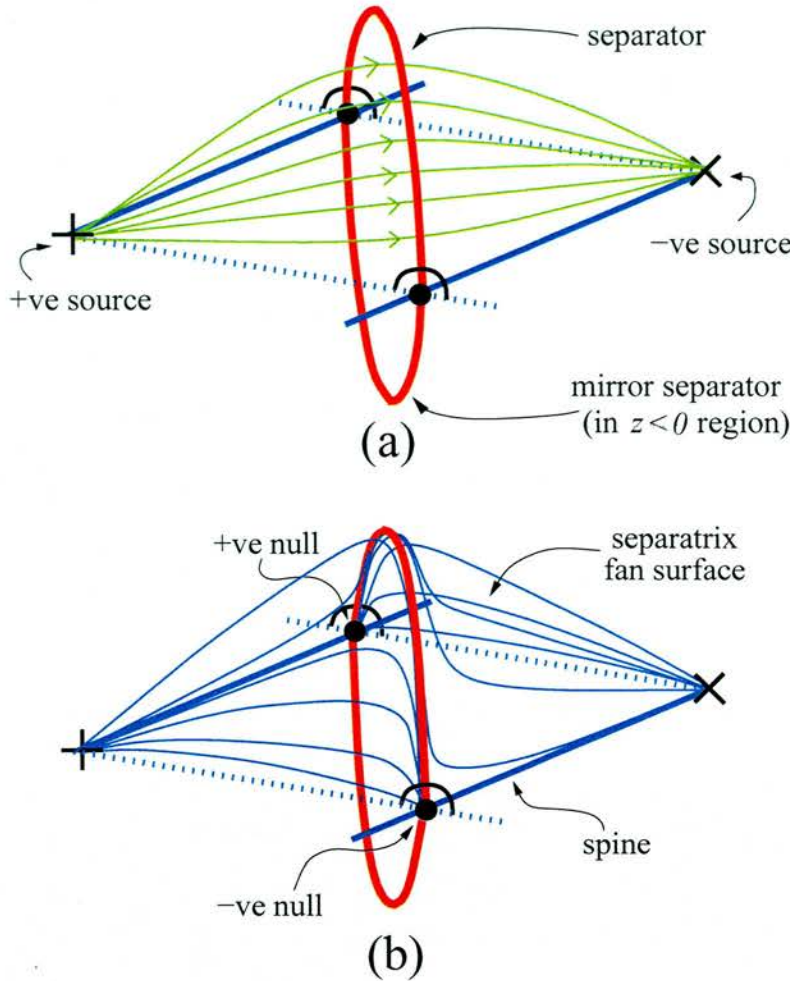


Figure 3.2: A separator-ring domain. A selection of field lines within the domain is shown in (a), and the field lines lying on the separatrices are shown in (b). The separatrix boundaries of the domain are two conical fan sectors, which join along a closed ring of separators. Since this example is a photospheric domain, the domain is symmetric in the $z = 0$ plane, therefore the separator in the mirror corona (the region $z < 0$, which is the reflection of the region $z > 0$) completes the separator circuit.

sections demonstrate how various domain structures occur in practice.

3.3 Locating Separators

The main problem with following the path of separator field lines is that in the fan plane of the null from which the integration is started, the field generally diverges away from the separator. This problem is most pronounced in the cases when the magnitude of the component of the field perpendicular to the separator, B_{\perp} , is much greater than the magnitude of the component tangent to the separator, B_{\parallel} (i.e. $|B_{\perp}| \gg |B_{\parallel}|$). However,

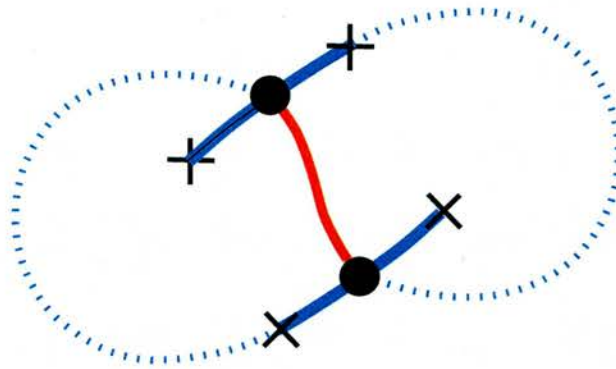


Figure 3.3: Point of bifurcation for global separator bifurcation with two dipoles, as seen from above. Null points are shown as black filled circles, positive sources are indicated by plus signs, and negative sources are indicated by crosses. Spine field lines are shown as solid blue lines, whilst fan field lines are the dotted lines. The red line is a separator.

one fortunate consequence is that when attempting to track the separator, the field only diverges in one direction in the plane perpendicular to the separator. Moreover, the field orthogonal to this direction in the plane perpendicular to the separator actually converges towards the separator. In the cases when $|\mathbf{B}_{\parallel}| \gg |\mathbf{B}_{\perp}|$, field lines generally follow the path of the separator and there is little divergence away from the separator.

In order to locate separators in a potential magnetic field, the fan plane of each null is first scanned for changes in the field-line connectivity. For each null positioned at \mathbf{r}_0 , a ring centred on \mathbf{r}_0 and lying in the fan plane of the null is taken, with radius small enough that the ring does indeed lie within the null's fan plane. 1000 field lines are then computed, starting from equally spaced points on the circumference of the ring (of course, when examining prone nulls, the section of the fan plane that lies below the $z = 0$ plane is not scanned, which by symmetry is the mirror image of the region $z > 0$). For each field line in turn, the source to which its endpoint connects is noted. If it is found that a particular field line is connected to a different source than that of the previously calculated field line, then there is at least one separator lying between the two field lines in the fan plane (see Figure 3.4(a)). Hence, if the field line starting from an angle θ_A about the ring is connected to source A , and the field line starting from an angle θ_B is connected to source B , then a field line from an angle $\theta_C = (\theta_A + \theta_B)/2$ is calculated, which in turn connects to source C , say. Naturally, if C is the same source as A , then θ_A is replaced with θ_C , and likewise θ_B with θ_C if $C = B$. However, in the case that source C is neither the same source as source A nor source B , then there must be more than one separator field line lying between θ_A and θ_B . Thus, this procedure of bisection must be performed recursively, so that both separators are followed. The process of bisection is repeated until $|\theta_A - \theta_B| < \epsilon_{\theta}$, where ϵ_{θ} is just above machine precision.

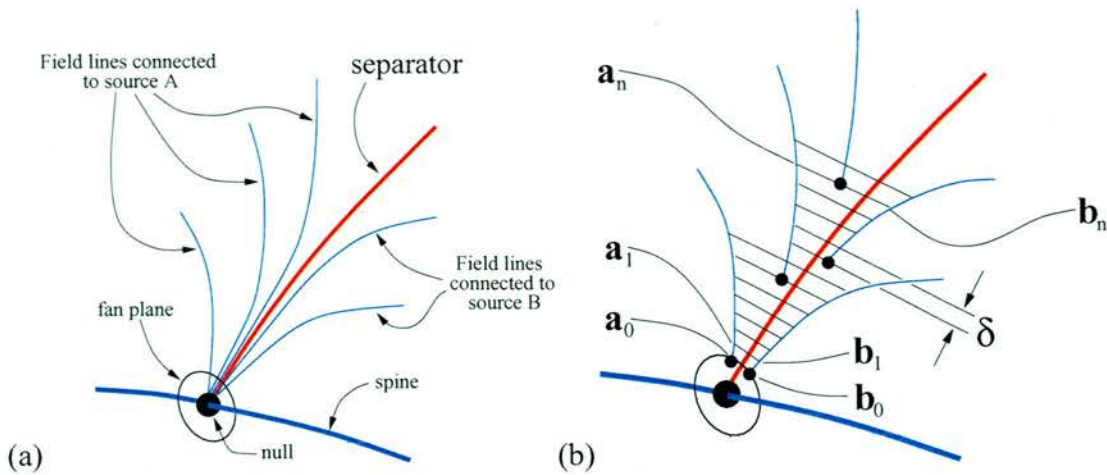


Figure 3.4: (a) Sketch of field lines about a typical separator curve. (b) Illustration of the method by which separator curves are traced.

3.3.1 Tracing Separator Curves

With two starting points a_0 and b_0 , given by θ_A and θ_B , the aim is always to have two field lines between which the separator is bounded. Thus, two field lines are calculated from the starting points, a_0 and b_0 , but this time the points by which the method of integration approximates the curves are stored.

The next step is to proceed simultaneously along both the field lines by an amount δ , i.e. say from a_0 to a_1 and from b_0 to b_1 , respectively. Since each field line is approximated by a series of points, this amounts to proceeding along the straight lines adjoining consecutive points. A check is then made to see whether or not $|a_1 - b_1| < \epsilon_S$, where ϵ_S is small, much less than the typical source separation. If this is the case, then a further distance of δ is traversed along the bounding field lines from a_1 to a_2 and from b_1 to b_2 . The process continues on in this manner whenever $|a_n - b_n| \leq \epsilon_S$; however, if when moving from a_n to a_{n+1} and from b_n to b_{n+1} , it is found that $|a_{n+1} - b_{n+1}| > \epsilon_S$, then it is necessary to move back to a_n and b_n and calculate a field line from the point $c = (a_n + b_n)/2$, which connects to the source C . If the source C corresponds to the source A , then the old field line connected to A is replaced by the new field line, and similarly the old field line connected to B is replaced by the new field line if $C = B$. This process is sketched in Figure 3.4(b). Like the earlier scenario, though, the new field line may connect to neither A nor B . This means that there are (at least) two separators between a_n and b_n , and therefore this procedure must also be recursive, so that it is possible to follow both separators. This often happens since pairs (or even groups) of separators may be extremely close to one another, sometimes infinitesimally close, in the vicinity of

a null, only to split at a distance from the null.

The method outlined above is repeated until either the magnetic field drops below a threshold value, or progress ceases to be made spatially, indicating that the algorithm has arrived in the vicinity of a null. At such a point, a root-finding method is deployed, with the current position as an initial guess. If it is found that the current position is not in the neighbourhood of a null, then the iterations are continued and the root finder is applied again later on.

At each step n , a point $\mathbf{m}_n = (\mathbf{a}_n + \mathbf{b}_n)/2$ is defined. The difference $|\mathbf{m}_n - \mathbf{m}_{n-1}|$ is then calculated and added to a running total, δs . Whenever δs peaks above a threshold value, δs_{max} , the variable δs is then reset to zero and the current coordinates are stored in a position vector. Thus, although it may take very many increments δ to calculate the separator, only a sensible number of points are stored that smoothly trace the course of the separator.

In practice, it is quite beneficial to allow δ to vary depending upon the divergence of the field lines from the separator. For instance, if there is little divergence from the separator, it may be desirable to make δ relatively large, so that the algorithm hurries along the bounding field lines as quickly as possible, whereas when there is much divergence from the separator, it makes sense to have δ small so that as much information as possible may be obtained from a bounding field line before discarding it and performing the computationally expensive process of calculating a new one.

3.4 Classification of Magnetic Domains: An Extrapolation with no Upright Nulls

The same magnetogram region from 13 June 1998 as used for the balanced region study in Chapter 2 is analysed here. Here, though, all pixels below 20 Mx cm^{-2} are treated as noise and therefore ignored, and fragments that are comprised of less than 10 pixels (each pixel is $0.88 \times 0.88 \text{ Mm}$) are also ignored, leading to a region comprised of just 15 positive fragments and 18 negative fragments in total. With each fragment comprising 10 pixels or more, a point source is placed at the centroid of each fragment, which is calculated with respect to the positions and strengths of the pixels within the fragment. (See Section 1.4 for more details on the use of potential fields emanating from point sources). Figure 3.5 shows an image of the magnetogram region studied.

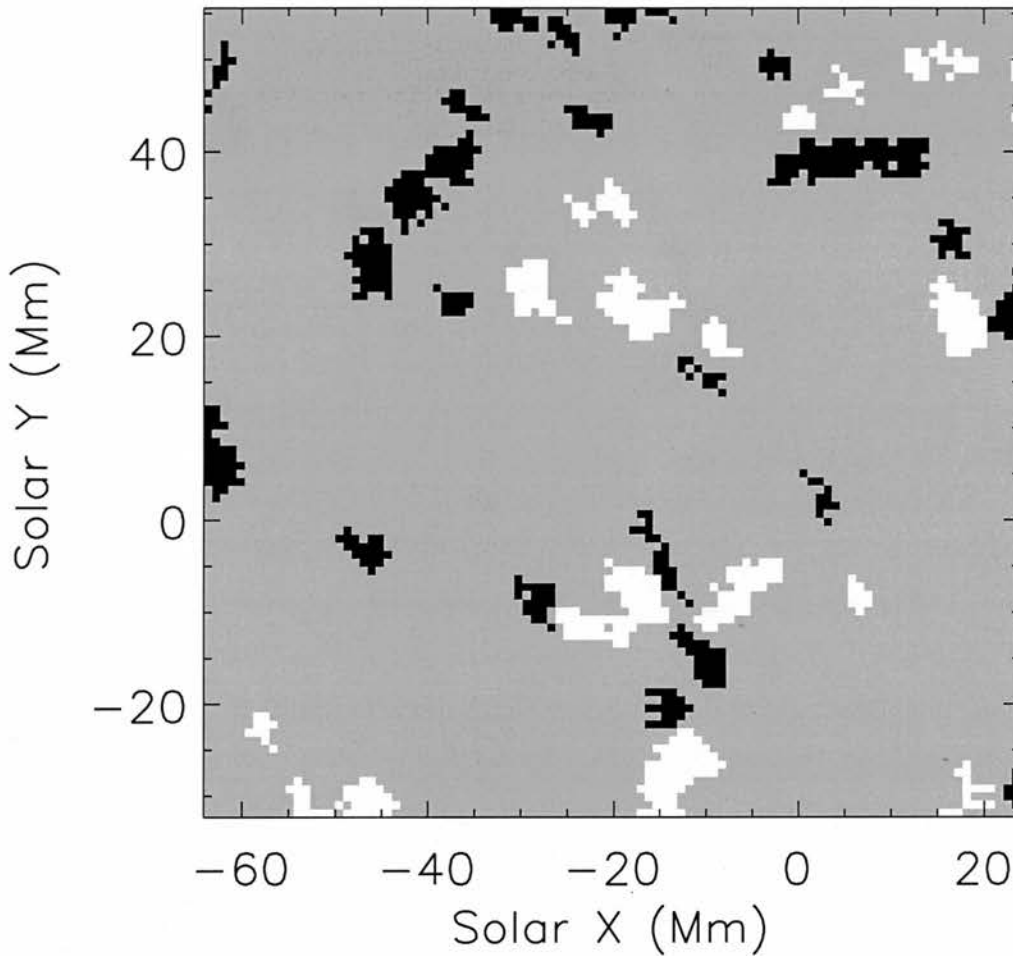


Figure 3.5: The magnetogram image of the 88×88 Mm inner region that is studied. Black regions represent negative flux, white regions represent positive flux, and grey is neutral.

3.4.1 Topology Equations

It is often useful to consider magnetic charge topology in terms of graph theory. The complete set of vertices possible comprises positive sources, negative sources, positive nulls and negative nulls, whilst every edge represents a connection between pairs of vertices belonging to the sets described above.

Longcope and Klapper (2002) studied the connectivity of the potential fields that arise from an arbitrary distribution of discrete sources. By using the Euler characteristics (Inverarity and Priest, 1999), and applying standard results from graph theory, they showed that the number of flux domains, N_d , in a field containing no upright nulls may be defined as

$$N_d = N_\gamma - N_0^\gamma + N_s, \quad (3.1)$$

where N_γ is the number of separators in the configuration, N_0^γ is the number of non-upright nulls (i.e. coronal or prone) with connected separators, and N_s is the total number of sources.

Longcope and Klapper (2002) also used graph theory to obtain expressions for the number of domains that have footprints (upright nulls must be excluded from these calculations too, as must null points which give rise to isolated domains (along with the sources whose entire flux is enclosed by such nulls)). Using Euler's relation $f = e - v + 2$, which relates the number of faces f (here N_{fp} , the number of footprint domains (if a domain has a footprint, then the pair of sources linked by that domain share field lines that lie in the $z = 0$ plane)), the number of edges e (here $4N_0^P$, with N_0^P denoting the number of prone nulls with connected separators) and the number of vertices v (here $N_s + N_0^P$), they obtained that the number of footprint domains is

$$N_{fp} = 3N_0^P - N_s + 2. \quad (3.2)$$

Furthermore, it may also be shown from the Euler characteristics that $N_0^P = N_s - 2$ for a field with no upright nulls; making use of this relation, Equation (3.2) simply becomes

$$N_{fp} = 2N_0^P. \quad (3.3)$$

In the example here (the domain footprints of which are shown in Figure 3.6), there are 15 positive sources (one of which, P4, is nested within an isolated domain) and 18 negative sources (one of which, N16, is also nested within an isolated domain). A negative balancing source located at an infinite distance from the sources is counted as a 19th negative source so that the system may be considered to be in perfect flux balance. Searching in the source plane reveals 16 prone positive nulls (one of which gives rise to an isolated domain) and 16 prone negative nulls (one of which also gives rise to an isolated domain), with no upright nulls present. Searching the volume throws up 2 negative nulls in the corona and 2 negative nulls in the mirror corona. These figures are consistent with the Poincaré-Hopf theorem (Milnor, 1965; Inverarity and Priest, 1999), which states that if there are N_0^B positive nulls and N_0^A negative nulls in a volume, then

$$N_0^B - N_0^A = N_s^+ - N_s^-, \quad (3.4)$$

where N_s^+ and N_s^- are the numbers of positive and negative sources, respectively.

By using the algorithm outlined in the previous section, 104 separators are found here

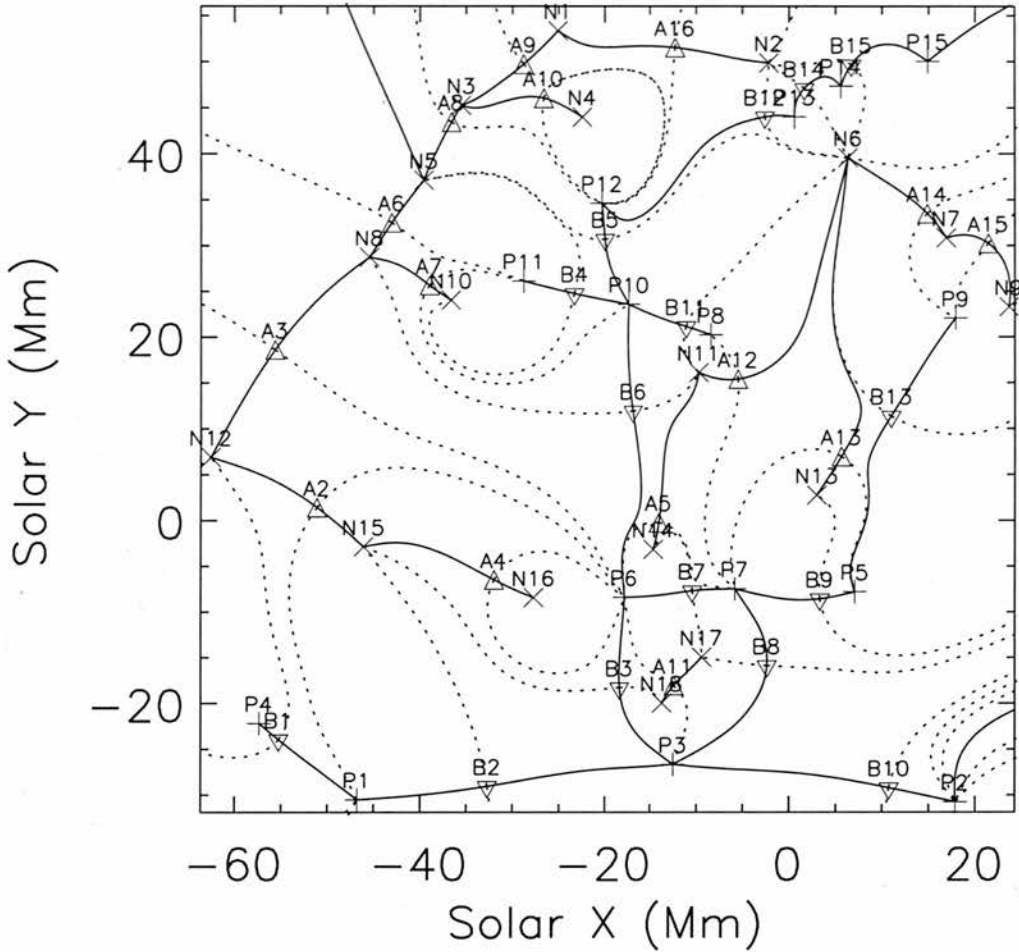


Figure 3.6: Domain footprints of the region. Positive sources are indicated by plus signs and negative sources are represented by crosses. Downward-pointing triangles are positive nulls; upward-pointing triangles are negative nulls. The dotted curves are planar fan field lines, whilst the solid curves are spine field lines.

(52 above the source plane, and 52 below); thus $N_\gamma = 104$. Removing the nulls and sources associated with isolated domains gives $N_0^B = 15$, $N_0^A = 19$ (15 in the plane, 2 in the corona and 2 in the mirror corona), $N_s^+ = 14$ and $N_s^- = 18$. The values for N_0^P , N_0^γ and N_s are therefore 30, 34 and 32, respectively. Applying Equation (3.1) implies a total of 81 domains in the region $z \geq 0$ (given by $N_{fp} + (N_d - N_{fp})/2$), whilst Equation (3.3) suggests that 60 of them should be expected to have footprints (of course, these figures exclude isolated domains). However, by constructing a connectivity matrix using the connectivity of the spine and fan field lines of each null, only 79 connections are found, 59 of which are planar. This means that there are two instances where a pair of sources is connected by more than one domain. These so-called “multiple domains” are discussed further in Subsection 3.4.3. The complete connectivity matrix is given in Table 3.1.

	P1	P2	P3	P4	P5	P6	P7	P8	P9	P10	P11	P12	P13	P14	P15
N1	—	F	C	—	—	C	—	—	—	C	—	F	—	—	—
N2	—	F	C	—	—	C	C	—	—	C	—	F	F	F	F
N3	—	F	C	—	—	C	—	—	—	C	—	F(2)	—	—	—
N4	—	—	—	—	—	—	—	—	—	C	—	F	—	—	—
N5	F	F	C	—	—	C	—	—	—	F	F	F	—	—	—
N6	—	F	C	—	F	C(2)	F	F	F	F	—	F	F	F	F
N7	—	F	C	—	C	—	C	—	F	—	—	—	—	—	—
N8	F	—	C	—	—	F	—	—	—	F	F	—	—	—	—
N9	—	F	F	—	F	—	F	—	F	—	—	—	—	—	—
N10	—	—	—	—	—	—	—	—	—	F	F	—	—	—	—
N11	—	—	—	—	—	F	F	F	—	F	—	—	—	—	—
N12	F	—	C	F	—	F	—	—	—	—	—	—	—	—	—
N13	—	—	—	—	F	—	F	—	—	—	—	—	—	—	—
N14	—	—	—	—	—	F	F	—	—	—	—	—	—	—	—
N15	F	—	F	—	—	F	—	—	—	—	—	—	—	—	—
N16	—	—	—	—	—	F	—	—	—	—	—	—	—	—	—
N17	—	—	F	—	—	F	F	—	—	—	—	—	—	—	—
N18	—	—	F	—	—	F	—	—	—	—	—	—	—	—	—
∞	F	F	F	—	—	—	—	—	—	—	—	—	—	—	—

Table 3.1: Connected pairs. F indicates that the given domain has a footprint; C indicates that the domain is purely coronal. Pairs of sources that are connected by more than one domain are indicated by a figure in brackets.

3.4.2 Photospheric Separator-Ring Domains

Examples of domain structures are shown in Figure 3.7. The two plots demonstrate how a given circuit of separators (here going from B9 to A13 and back to B9 via the mirror corona) may engirdle more than one domain. Figure 3.7(*top*) is similar in appearance to the sketch in Figure 3.2(b), and in this scenario the two sources are positioned such that they straddle the closed separator loop. Thus, field lines within the domain pass through the closed curve of separators when connecting the positive source to the negative source. However, Figure 3.7(*bottom*) is a distortion of this, so that the two opposite-polarity sources do not straddle the separator loop and instead both lie on the same side of the separator ring. In such a scenario, although it is topologically equivalent to the straddled domain discussed above, field lines within the domain do not pass through the separator ring when connecting the positive source to the negative source.

A loop of separators that encircles a domain, however, need not only visit just two nulls. Indeed, unless a coronal null connects to another null by more than one separator above the $z = 0$ plane, then any domain that has a coronal null as one of its vertices must

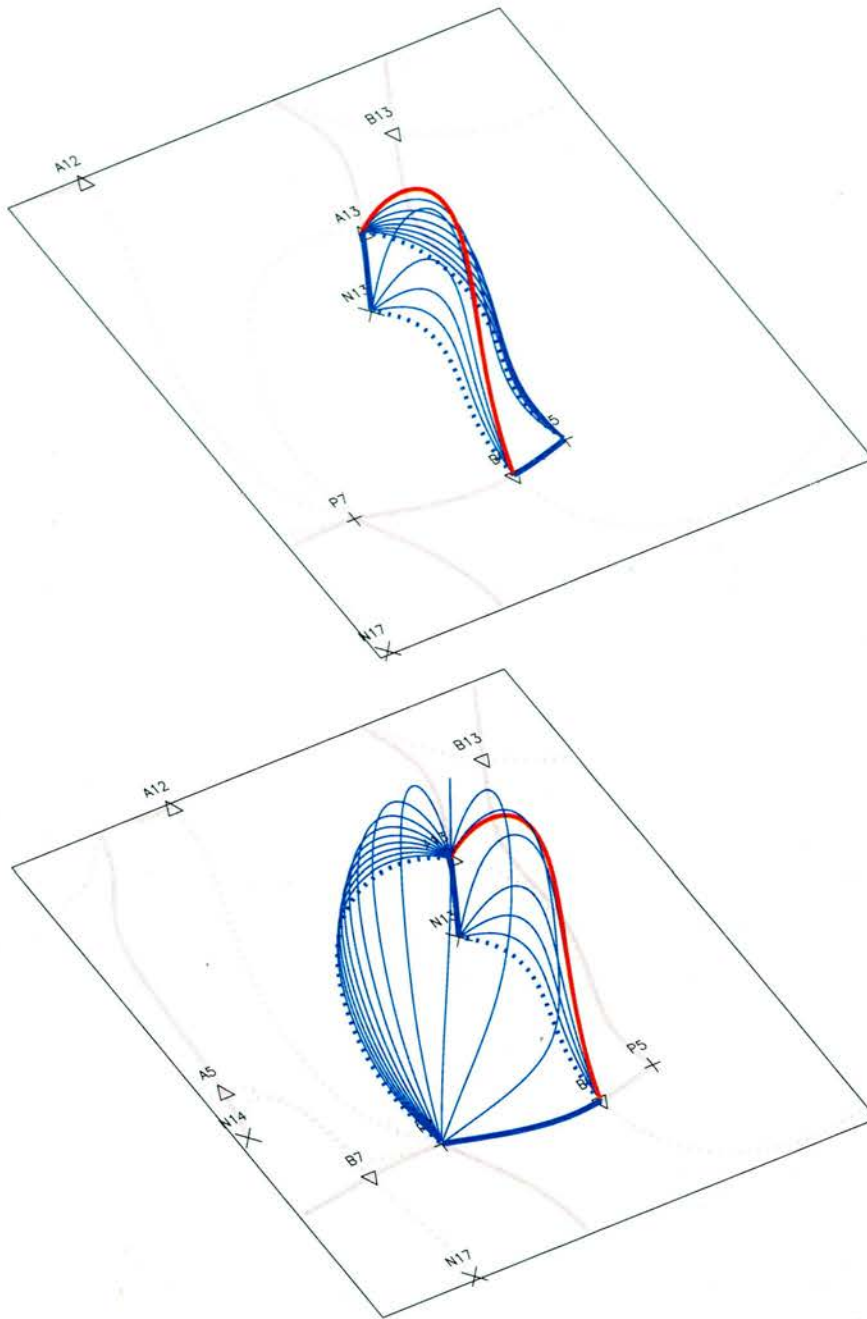


Figure 3.7: Plots of the domains that connect P5 to N13 (*top*) and P7 to N13 (*bottom*). The thin blue curves are fan field lines, the thick blue curves are spine field lines, and the red curves are separator field lines. The dotted blue curves are the planar fan field lines. Domain footprints for the surrounding region are also shown in grey. Animations showing 3D rotational views about these configurations are provided on the accompanying CD (see Appendix F for details on how to access them).

have more than two nulls visited by its separator ring.

Figure 3.8 shows the domain linking source P6 to source N12. This domain exhibits a curious property; it appears to be encircled by two rings of separators. One such ring is

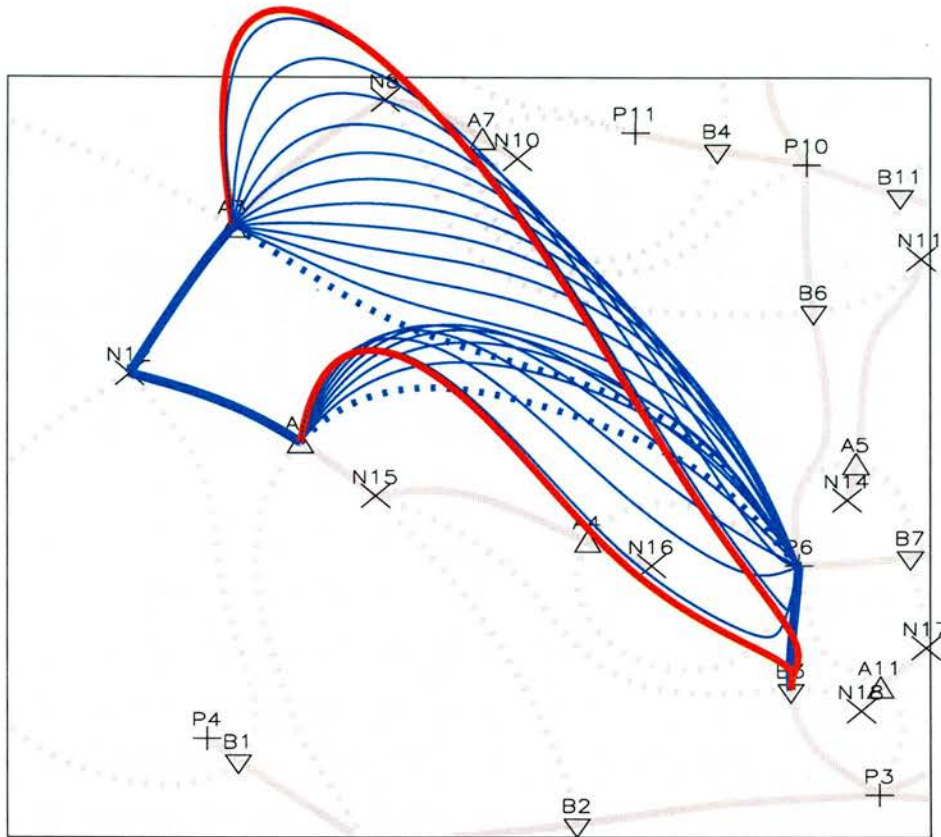


Figure 3.8: The domain linking P6 to N12; the closed ring of separators is distorted so that it touches itself at B3. An animation showing a 3D rotational view about this configuration is also available on the accompanying CD.

the circuit $B3 \rightarrow A2 \Rightarrow B3$, where ‘ \rightarrow ’ indicates that the separator above the plane $z = 0$ is traversed, whilst ‘ \Rightarrow ’ indicates that the corresponding separator in the mirror corona below the $z = 0$ plane is traversed. The other separator loop is the circuit $B3 \rightarrow A3 \Rightarrow B3$. However, since these two circuits share a common null, i.e. B3, then it may be argued that there is only one separator ring, which is the circuit $A3 \rightarrow B3 \rightarrow A2 \Rightarrow B3 \Rightarrow A3$. In such case, the field lines connecting P6 to N12 pass through the single separator loop, and the double visit to B3 in the separator circuit means that the loop is distorted such that it kisses itself at B3. Such domains are not uncommon; indeed, there are several other examples of them in the region studied here.

Whereas a domain of the type illustrated in Figure 3.2 has a footprint with a vertex of each of the four types on its boundary, domains that have two encircling separator curves have a positive source and a negative source, but two nulls of the same type on the boundary of their footprint. However, a photospheric domain with a coronal null as part of its separator circuit may also have such a photospheric footprint, and so domains with two engirdling separator curves may not be identified by their footprints alone.

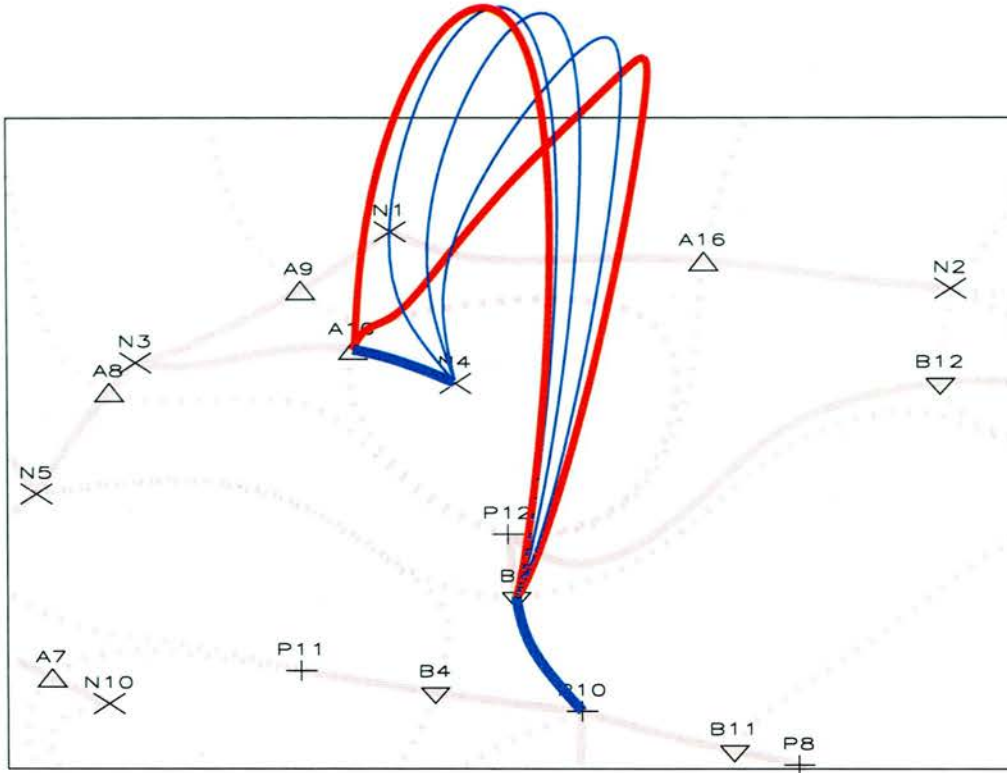


Figure 3.9: Plot of the domain linking P10 to N4. Fan field lines from A10 that connect to P10 and form part of the boundary of the domain have been omitted for clarity. An animation showing a 3D rotational view about this configuration is also available on the accompanying CD.

It may be noted that in Figure 3.8 the fan sector from B3 is not shown; this is because in non-symmetric states, computing fan field lines from equally spaced points on a small ring within the fan plane of a null only partially outlines the fan surface. This is due to the fact that, in the lack of symmetry, the field strength is not uniform on the ring about the null, so that field lines swiftly diverge from the regions of weak field. The result of this is that fan field lines can often cluster together in clumps, and thus only part of the separatrix is shown. This is discussed further in Chapter 4.

3.4.3 A Multiply Connected Pair of Sources

Close inspection of Figure 3.6, around the point $(-30, -10)$, shows the typical footprint of an isolated domain which is bounded entirely by an unbroken fan from a single null, with a source lying within the domain (here it is the fan from null A4 that completely encloses all the flux from source N16). In such cases, a neighbouring domain has two footprints, separated by a spine from the null with the unbroken fan (for example, there are two regions in the $z = 0$ plane that connect source P6 to source N15).

Upon first encountering the footprint at around $(-20, 40)$ in Figure 3.6, it is tempting to conclude that the domain linking P12 with N4 is one of the nested domes described above. However, by scanning the fan plane of A10, one finds a change in connectivity of the fan field lines from P12 to P10, then a change back to P12. Thus, the fan from A10 breaks through the fan from B5, only to break through it again, therefore allowing a sliver of flux from P10 to connect to N4 (see Figure 3.9). The two distinct separators that link B5 to A10 provide the encompassing ring of separators, which the field lines from P10 clearly pass through in order to connect to N4. This also means that there are some field lines from N4 that pass near B5 and along one of its spines to P12.

When a pair of nulls is connected by two or more discrete separators (neglecting separators in the mirror corona, that is), then this is an indication that a pair of sources is linked by more than one domain. This is the case here, and there are two separate domains that link the source P12 to N3 (their footprints can be seen in Figure 3.6). These two domains are in fact of the type that appear to have two engirdling separator loops.

3.4.4 Coronal Domains

Since much of the flux in a magnetic field emanating from a multitude of mixed-polarity sources closes down at low altitudes, the majority of the flux is concealed within the low-lying chromospheric or low coronal domains. However, the remaining flux that is contained within coronal domains is also of vital importance, as the magnetic flux in these higher domains may channel energy up into the Sun's outer atmosphere.

In contrast with the findings of Subsection 3.4.2, where some domains with non-straddled separator rings were found, the flux in a coronal domain always passes through its engirdling separator ring, since the closed curve of separators exists entirely above the $z = 0$ plane. As is the case with photospheric domains, the closed curve of separators that encircle a coronal domain may contain only planar nulls or a combination of planar nulls and coronal nulls. However, it is also possible that the engirdling separator curve of a coronal domain may contain only coronal nulls, which of course is not possible with photospheric domains.

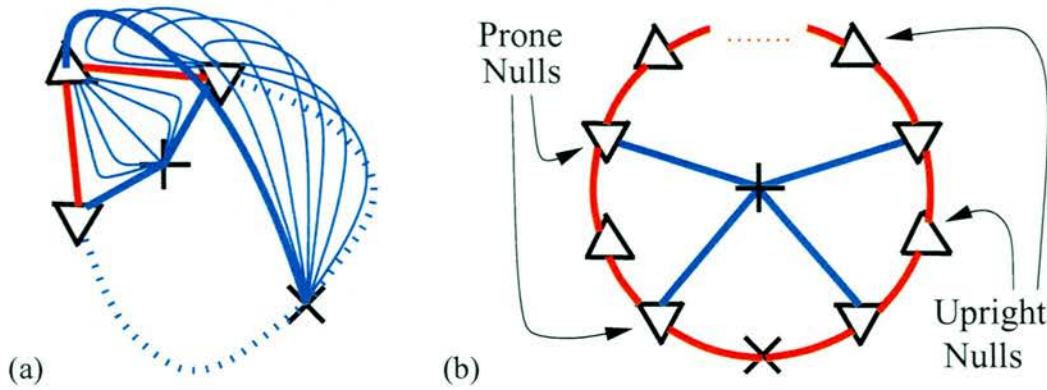


Figure 3.10: (a) Sketch of an isolated domain bounded by fan surfaces from two positive prone nulls. (b) Illustration of how an isolated domain with many prone and upright nulls on its boundary may exist. The spines from the prone nulls connect to the positive source.

3.5 Magnetic Fields Containing Upright Nulls

Magnetic domains about upright null points fall into two distinct categories; those that are photospheric, with a clear connecting path between the domain sources in the $z = 0$ plane, and those that are semi-coronal in that, despite having field lines in the photospheric plane, they require the volume above the plane $z = 0$ in order to connect a given pair of sources. The distinction does not stop there, though, since it turns out that photospheric upright-null domains are actually isolating domains that entirely enclose the flux from one of the domain sources, whereas semi-coronal upright-null domains are separator-ring domains.

3.5.1 Photospheric Domains about Upright Nulls

Figure 3.10(a) illustrates how the flux from a given source, here positive, may connect entirely to another source through a photospheric upright-null domain. The fan surfaces from two prone nulls form the boundary of the domain, both unbroken but for two distinct separator field lines that link the two prone nulls to the upright null. The two prone fan surfaces are separated by the spine from the upright null, which connects to the negative source.

In theory, more complicated domains of this type could exist, characterised by a ring in the photosphere of, say (without loss of generality), p positive prone nulls interspersed with $u \equiv p - 1$ upright nulls, with a negative source between the two positive prone nulls that have no upright null between them (shown in Figure 3.10(b)). The spines from the prone nulls would connect to a positive source situated in the centre of the configuration,

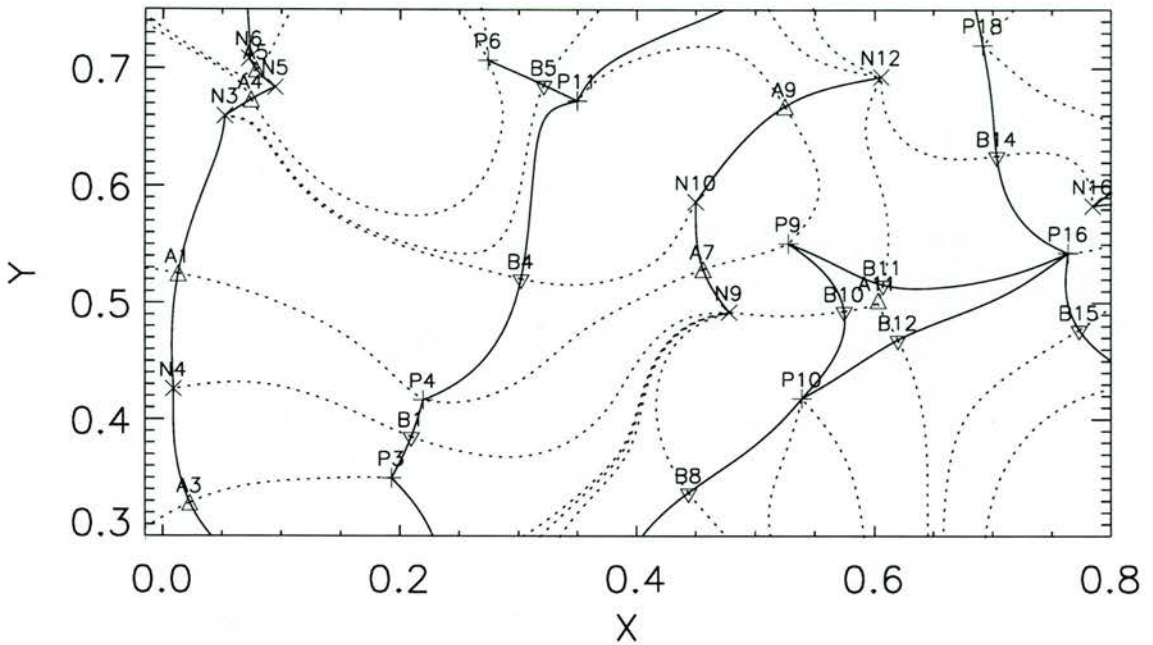


Figure 3.11: Domain footprints for the region containing an upright null, A11, located at (0.6,0.5).

and the spines from the upright nulls would connect to the negative source. Whilst such configurations are topologically possible, they are undoubtedly extremely rare in practice.

3.5.2 Semi-Coronal Domains

The magnetogram region studied so far contains no upright nulls. Thus, in order to study the properties of semi-coronal upright-null domains in complex magnetic fields, a source configuration that gives rise to an upright null is randomly generated. 36 sources are randomly scattered in a unit square (18 of each polarity), and each source is allocated a random strength. One set of sources is then multiplied by a single flux-balancing factor. This process is repeated several times until a region containing an upright null is found. The domain footprints for the region about the upright null are shown in Figure 3.11.

Figure 3.12 shows the skeleton of a semi-coronal upright-null domain around the upright null located at (0.6,0.5), which connects P10 to N3. The domain footprints about an upright null will generally contain a source, two similar polarity nulls, and an opposite polarity null (the upright one) on its boundary (note that photospheric upright-null domains that enclose a single source have two footprints, one of which adheres to this description). The two nulls of similar polarity, here B10 and B12, are connected to the upright null, here A11, by separators. Since the domain studied here is semi-coronal, a further null, here A1, of the same polarity as the upright null must connect to the two

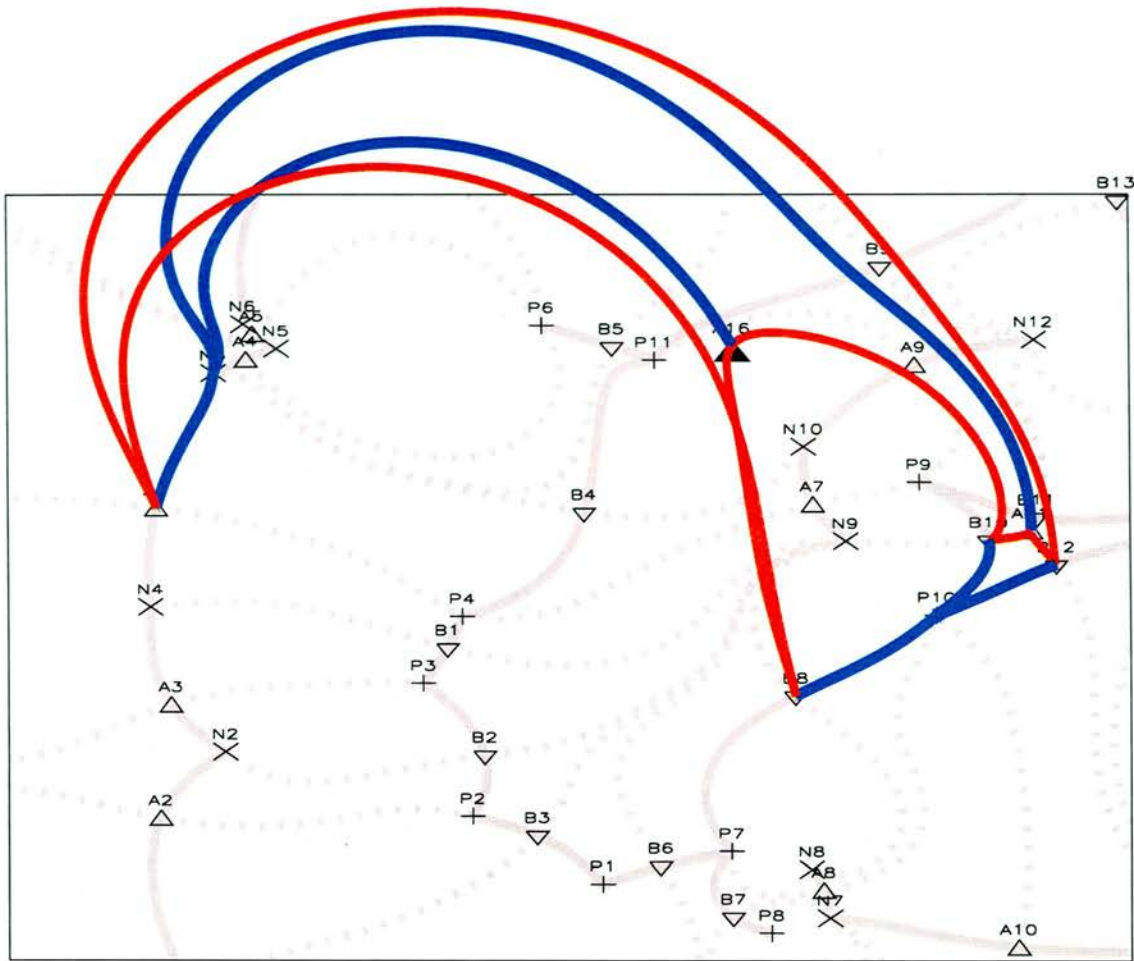


Figure 3.12: Structure of a domain about a typical upright null. The coronal null A16 is represented by the filled upward-pointing triangle. Fan sector field lines have been removed for clarity. An animation showing a 3D rotational view about this configuration is also available on the accompanying CD.

similar-polarity nulls B10 and B12, in order to complete the circuit. In this particular example, B10 does not connect directly to A1, but instead connects to the coronal null A16, which connects to B8, which in turn connects to A1. Thus the complete separator circuit is $B10 \rightarrow A16 \rightarrow B8 \rightarrow A1 \rightarrow B12 \rightarrow A11 \rightarrow B10$. The other two domains about the upright null shown here are structured in a similar way.

Such domains are peculiar in that, although they are not purely coronal, since they have part of their separator circuits in the photospheric plane, the separator circuit does not dip below the $z = 0$ plane, as it would do with regular photospheric domains. Since there is no direct connection through the photosphere from P10 to N3, the domain subsequently takes on somewhat of a loop-like structure.

Whilst the upright null here is at the confluence of three domains, a general upright

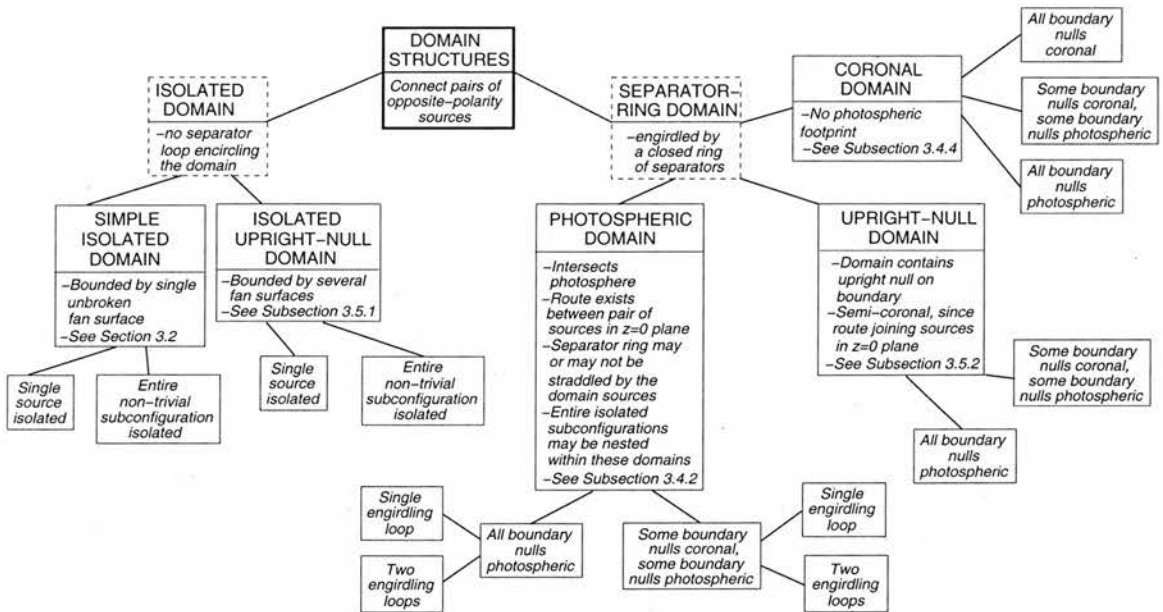


Figure 3.13: Classification of domain structures with respect to their various distinct properties.

null may be at the confluence of a great deal more, so that, although a prone null may have a maximum of four connections in the source plane (two spine field line connections and two connections from the fan field lines lying in the $z = 0$ plane), an upright null may have substantially more connections in the photospheric plane. Beveridge et al. (2003) showed how upright nulls affect planar connectivity, likening it to river valleys in a geographical contour map, where the contours are of the potential F for which $\nabla F = \mathbf{B}$. In such a scenario, the planar separators connected to the upright null follow valleys of the potential and the upright nulls lie at local minima.

3.6 Conclusions

An algorithm has been presented here for locating separator fields lines in general three-dimensional potential fields of arbitrary complexity. Such an algorithm is an invaluable tool in the process of identifying the boundaries of magnetic domains in a model field based on observed magnetogram data.

The potential field arising from a sufficiently complicated point-source model of the mixed-polarity quiet Sun consists of many intricately entwined domain structures, connecting pairs of opposite-polarity sources.

Previous authors have observed that these domain structures may be broadly categorised into two classes, namely, the isolated dome domain, where a single unbroken fan

surface encloses a source and all its flux, and the separator-ring domain, which is bounded by sectors from several fan surfaces and encircled by a closed curve of separators. It has been established here, however, that these descriptions overly simplify the matter, since the various domain structures that exist may be classified in far greater detail depending upon their geometrical and topological traits. Figure 3.13 summarises the various domain structures and their properties.

It has also been demonstrated here that the number of domains in a system is not necessarily the same as the number of connected pairs, since two instances have been found where a pair of sources is connected by more than one domain. Along with the example in Subsection 3.4.3 of a separator-ring domain with a footprint similar to that of an isolated domain, this unfortunately proves futile any attempts to create a general scheme that uses the domain footprints and knowledge of the presence of coronal nulls in order to deduce the whereabouts of separators, which are notoriously awkward to trace.

Understanding the structure of the building blocks of complex magnetic topologies, along with the bifurcations that may mutate them, is crucial to the understanding of the Sun's magnetic field. It will be interesting in the future to see the role that various magnetic structures play in the dynamical processes ever present in the Sun's atmosphere.

Chapter4

Separators in Quiet-Sun Magnetic Fields[†]

盗	と	盗	The thief
の	り	人	Left it behind
月	の	に	
	こ		The moon at the window
	さ		
	れ		
	し		

大愚良寛

"TAIGU" RYOKAN (1758-1831)

4.1 Introduction

As has been seen already in Chapter 1, the gas pressure in the Sun's corona is much less than the magnetic pressure, leading to the belief that the magnetic field, which, in the quiet Sun, emerges through the photosphere in well-separated magnetic flux fragments, expands to fill the entire coronal volume. Hence, many dynamic processes in the solar atmosphere occur as a result of the presence of the dominant magnetic field. However, brightenings are observed in X-rays of coronal plasma along only a few field lines, so attention has turned to the topological structure of the field to try and explain the observations.

One particular topological feature that is a prime suspect in the quest to pin down the precise location of coronal heating is the magnetic separator. Whilst steep field gradients at null points may produce enhanced current densities that result in coronal heating (Titov and Priest, 1993), studies have shown that separators are likely to be sites of intense

[†]The work in this chapter has been accepted for publication in Solar Physics (Close et al., 2004b).

heating (Galsgaard et al., 2000; Priest and Titov, 1996). Although the statistics of nulls present in mixed-polarity fields are now fairly well understood, only recently have studies begun to provide an insight into the statistical properties of separators in complicated magnetic structures (see, for example, Beveridge et al., 2003 and Welsch and Longcope, 1999). One of the main reasons for the relatively few studies of separator statistics is the fact that separators are so awkward to trace, even for the most simple method of extrapolation, i.e. potential field extrapolation. A good understanding of the number density of separators in quiet-Sun fields is, however, of crucial importance if meaningful estimates of coronal heating due to separator reconnection are to be obtained.

Here, the aim is to analyse the density and character of separators found in quiet-Sun fields. Section 4.2 outlines how model fields similar to those of Schrijver and Title (2002) are obtained. The results of this Monte Carlo simulation are then presented in Section 4.3, whilst Section 4.4 analyses fields based on observed data. A concluding discussion is presented in Section 4.5.

4.2 An Exponential Distribution of Source Strengths

In order to examine the density of separators in potential magnetic fields, a plane is first sprinkled with point sources which provide the nulls from which separator statistics are then derived. Each point source here represents a whole fragment; the advantages of such a representation are discussed in Section 1.4. (Details regarding the use and applicability of potential fields are also given in Section 1.4).

In creating these random fields, the algorithm of Schrijver and Title (2002) is followed. Point sources are randomly positioned on a plane within a unit square, subdivided into 9 smaller squares. Within each subdivision, 16 sources of each polarity are randomly positioned, with strengths ranging from 0.5 to 5 in arbitrary units. This is chosen to coincide with the distribution observed by Schrijver et al. (1997) for the quiet-Sun network, although recent work by Parnell (2002) has suggested that a Weibull distribution, which involves both a power law and an exponential, provides both a statistically good fit to the data and a physically reasonable prediction for the absolute flux density.

Only situations for which there is an overall flux balance are considered, so one polarity is multiplied by a single flux-balancing factor.

Null points are found in each of the 200 simulated fields by first searching for minima of $|\mathbf{B}|$ in a $100 \times 100 \times 50$ grid positioned over the central $\frac{1}{3} \times \frac{1}{3} \times \frac{1}{6}$ region of the

source plane. The precise positions of the nulls are found by using a Brodyn root-finding algorithm. In order that all nulls may be resolved, sources may not lie closer than 0.02 units.

For each null at position \mathbf{r}_i , say, the eigenvectors of the derivative matrix \mathbf{M} , for which $\mathbf{B} = \mathbf{M} \cdot \mathbf{r}_i$ in the vicinity of the null, are calculated by maximising and minimising the function

$$K_i = \frac{\mathbf{B}(\mathbf{r}_i + \delta\mathbf{r}) \cdot \delta\mathbf{r}}{|\mathbf{B}(\mathbf{r}_i + \delta\mathbf{r})||\delta\mathbf{r}|} \quad (4.1)$$

on the surface of a small sphere of radius $|\delta\mathbf{r}|$ centred on the null point. K_i takes its maximum value of 1 when the field \mathbf{B} is in the same direction as the vector $\delta\mathbf{r}$, whilst it takes the value -1 when \mathbf{B} and $\delta\mathbf{r}$ are antiparallel. Taking the cross product of the two vectors $\delta\mathbf{r}_1$ and $\delta\mathbf{r}_2$, say, which give $K_i = 1$ and $K_i = -1$, gives a third direction, $\delta\mathbf{r}_3$, say. The two similar-signed vectors define the fan of the null, with the remaining vector corresponding to its spine. If the value of K_i given by the spine vector is 1, then the null is negative; if $K_i = -1$, the null is positive.

With knowledge of the orientation of the fan planes and spine field lines, it is then possible to begin the search for separator field lines.

4.3 Monte Carlo Simulation

Having followed the same method as Schrijver and Title (2002), for distributing sources on the source plane, similar results are found for the density of nulls; 1.090 ± 0.006 nulls per charge are found, of which 1.001 ± 0.005 nulls per charge (around 92%) lie in the source plane, with 0.089 ± 0.004 situated above the source plane. (A histogram of their heights is shown in Figure 4.1). The number of prone nulls that occur is also examined, and a total of 0.0023 ± 0.0006 upright nulls per charge are found. This is quite close to the figure of Beveridge et al. (2003), who found a slightly lower value of 0.0018 ± 0.0007 for an exponential distribution in perfect flux balance; however, they obtained their result by averaging over 1000 realisations, whereas only 200 are considered here.

A complete mapping of the connectivity of a potential field arises from complete knowledge of the connectivity of the spine and fan field lines associated with magnetic null points. In the plane, a prone null may have a maximum of four connections (two spine field-line connections and two connections from the fan field lines lying in the $z = 0$ plane). An upright null, though, may have substantially more connections in the

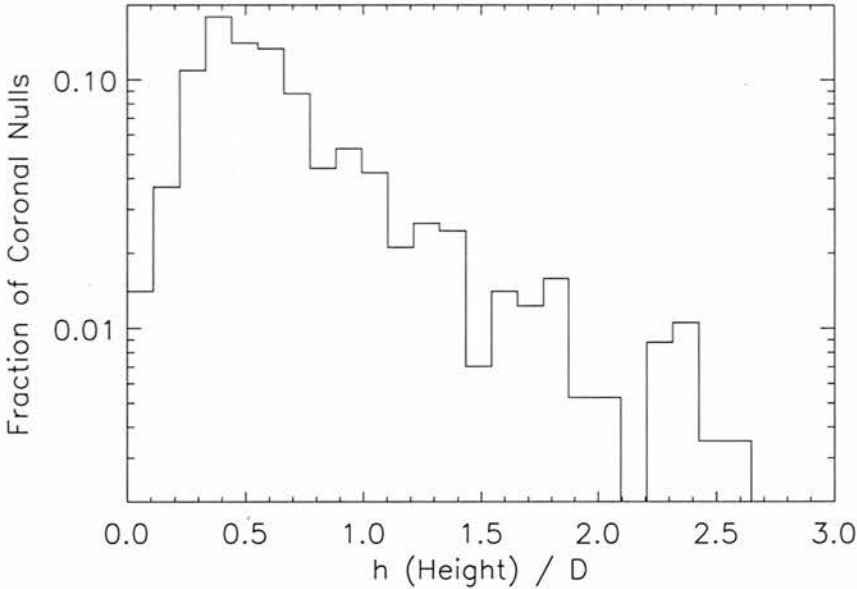


Figure 4.1: Histogram of heights of coronal null points above the source plane, with the heights normalised to the mean source separation, D .

photospheric plane. However, by analysing the connectivity about separators associated with upright nulls, it is found here that, although the number of connections varies from 2 to 7, the average is 3.33 ± 0.35 connections per upright null. Thus, these findings predict that, on average, upright nulls actually have fewer connections than prone nulls. This is not likely to be the case, however, in fields consisting of sources of a single polarity, where a great many separator field lines tend to bunch together to form trunks that connect to upright nulls (Beveridge et al., 2003).

A prone null may lie at the confluence of a maximum of four domains that have photospheric footprints. In a scenario where there are only prone nulls, each with a maximum of only one connected separator above the source plane, there are no coronal domains and the number of photospheric domains is equal to the total number of domains in the configuration. However, when there is more than one separator connected to a given null, each extra separator has an associated coronal domain with no photospheric footprint. Thus, the connectivity of field lines in the plane will not generally show up the full picture. One would expect to find an average of around 3–4 planar connections per null, since isolated dome domains (in which the entire separatrix surface from a single null forms a closed dome enclosing a single source (see Chapter 3), meaning that the given null has only three photospheric connections) are also observed in even the most complex of configurations (e.g., Schrijver and Title, 2002; see also Chapter 2). In the plane, connectivity statistics for sources should therefore be quite similar to connectivity statistics for photospheric nulls, since the number of photospheric nulls is roughly of the order of the number of

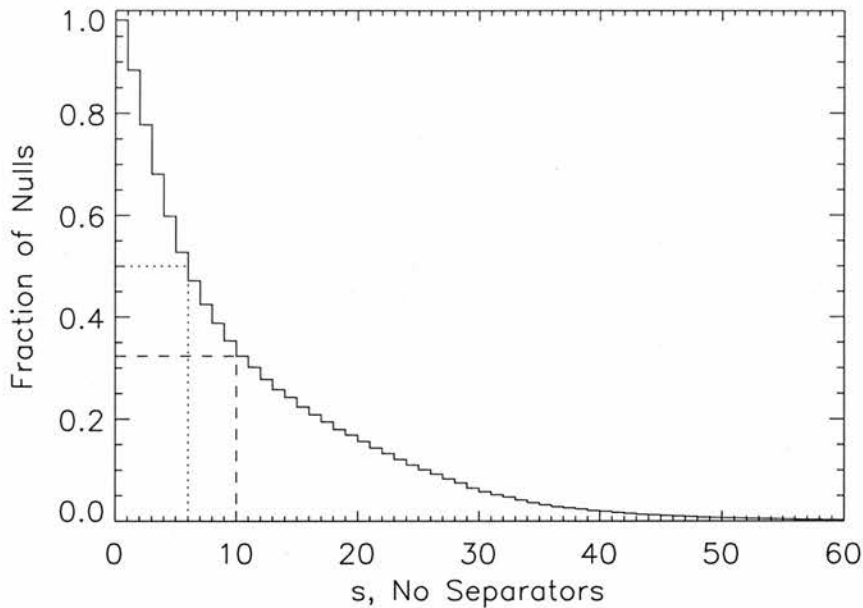


Figure 4.2: Fraction of nulls with number of separators greater than s . Specific values are indicated for the fraction 0.5 (*dotted line*) and for the mean number of connected separators (*dashed line*).

sources.

4.3.1 Separator Densities

Brown and Priest (1999a) examined both how separators are created and destroyed and what the topological conditions are for their existence. They not only showed how two separatrix surfaces intersect to form a stable separator, but also how two neighbouring separators can interact and merge into a single separator.

Here the question: how many separators should one expect to exist in a complex magnetic configuration? is explored. This query is approached by examining the number of separators connected to the nulls present in the model magnetic fields studied here. In such configurations, where there are 32 sources and around 34.9 null points in the inner region, an average of 176.2 separators are found. (Separators are located and traced using the algorithm outlined in Section 3.3). This corresponds to 10.1 ± 0.13 separators connected to each null. Figure 4.2 shows the fraction of nulls with numbers of connected separators totalling s or more. Although the average number of separators per null is around 10.1, 50% of nulls have less than 6 connected separators, with only the top 32% of nulls having more than 10 connected separators. Thus, although the average number of separators per null is quite high, it is the contribution from only a handful of nulls with a

great many connected separators that results in such a high average number of separators per null. The maximum number of separators found to be connected to any particular null is 100.

At this point, the largely unexplored concept of multiple domains must be addressed. Multiple domains, as discussed in Chapter 3, occur when two or more distinctly separate domains link a common pair of sources. Hence, if $N_m - 1$ of the N_m domains that link the pair of nulls are removed, then they will still be linked. Such domains have been absent from configurations arising due to only a handful of sources. Here, by noting the startpoints and endpoints of each separator, pairs of nulls that are connected by more than one separator are identified. Each ‘extra’ (or ‘multiple’) separator field line connecting a pair of nulls indicates the presence of a multiple domain, and this is used to gain a measure of the frequency of occurrence of multiple domains. An average of 1.04 ± 0.04 such domains are found to be associated with each null, which in turn corresponds to around 1.13 multiple domains per source. Thus, there are more domains present in a complex configuration than one could glean by merely examining the connectivity of field lines alone.

Of course, the above figures can be subdivided according to whether the null in question is photospheric or coronal. In doing so, 9.9 ± 0.13 separators per photospheric null are found, with 1.07 ± 0.04 corresponding to multiple domains. The figure for coronal nulls is 12.42 ± 0.46 separators per null, with 0.72 ± 0.15 corresponding to multiple domains. Of course, each separator connects a pair of opposite-polarity nulls, so the total number of separators is equal to half the sum of the number of separators connected to each null. In the case of prone nulls, the region of the fan plane situated below the $z = 0$ plane is not considered, and since the majority of photospheric nulls are prone, each photospheric null actually has around 19.8 separators connected to it. So on average, if real and mirror separators are considered, then photospheric nulls have more connected separators than coronal nulls.

4.3.2 Density of Topologically Distinct Regions

Subtracting the number of separators corresponding to multiple domains from the total number of separators leaves 9.06 separators per null. For every coronal null and upright null, each of these separators indicates the presence of a connection from that null’s fan plane to a distinct source. For prone nulls, on the other hand, the number of fan plane connections for each null in turn is equal to the number of separators connected to that

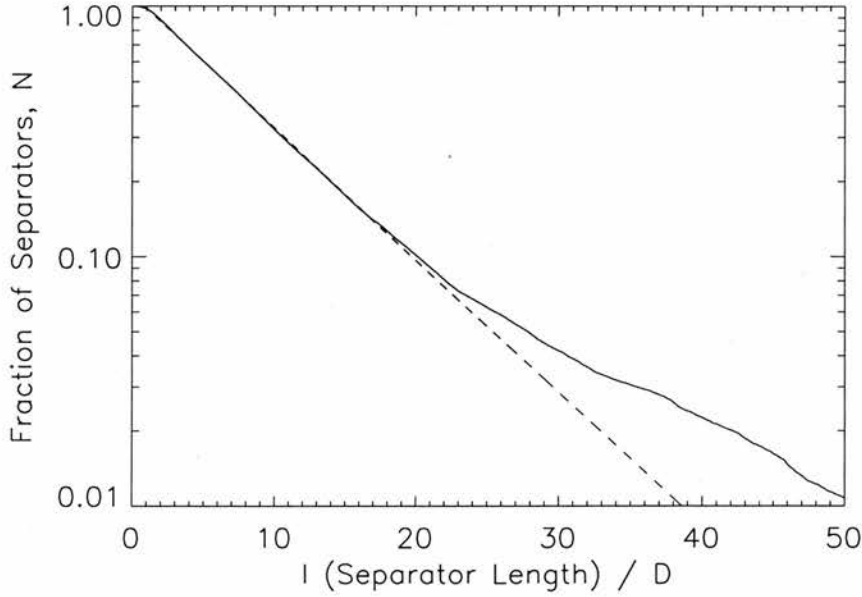


Figure 4.3: Fraction of separators with length greater than l , normalised with respect to the mean source separation, D . The dashed line represents the function $y = 1.11 \exp(-0.12l/D)$ and is fitted to the shortest 90% of separators.

null plus one and minus the number of connected upright nulls. So the total number of connections between null fan planes and sources, C_{ns} , is equal to

$$C_{ns} = C_{cs} + C_{us} + C_{ps} + N_p - C_{us} = C_{cs} + C_{ps} + N_p, \quad (4.2)$$

where C_{cs} is the total number of non-multiple separator field lines associated with the coronal nulls (where ‘non-multiple’ means that only one separator is counted per pair of connected nulls), C_{us} is the total number of non-multiple separator field lines associated with the upright nulls, C_{ps} is the total number of non-multiple separator field lines associated with the prone nulls and N_p is the number of prone nulls. Note that an upright null cannot connect to another null by any more than one separator field line. In the case here, $C_{ns} = 69\,570$, which corresponds to an average of 9.97 fan plane connections per null. This in turn corresponds to roughly 10.9 connections per source. Schrijver and Title (2002) found an average of 8 connections per source. Their method of sampling the field, by which they plotted a great many field lines from a small hemisphere centred on each source, likely missed the small domains that fill tiny sections of space and account for a minuscule fraction of the total flux; however, their routine has the advantage that it can readily provide statistics on the apportionment of flux among the larger domains in the field.

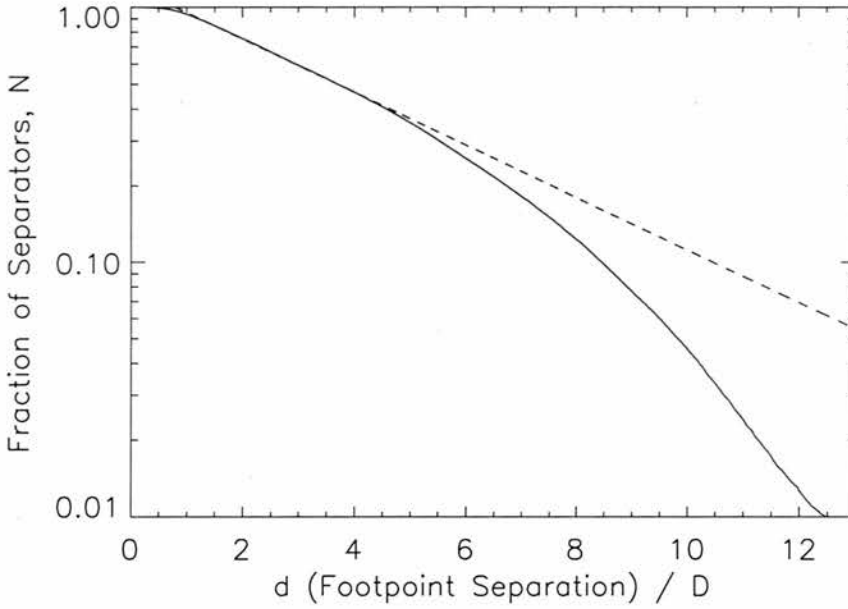


Figure 4.4: Fraction of separators with footpoint separation greater than d , normalised with respect to the mean source separation, D . The dashed line represents the function $y = 1.21 \exp(-0.24d/D)$ and is fitted to the shortest 60% of separators.

It is found that $1.8\% \pm 0.69\%$ of nulls have no separators connected to them. This is of particular interest because, as seen in Chapter 3, there are, broadly speaking, only two types of domain that are present in potential magnetic fields, namely isolated domains that are bounded by a single unbroken fan, and separator-ring domains that are engirdled by a closed curve of separators. Thus, the findings here suggest that less than 2% of nulls give rise to domains of the former type.

The fraction of separators with length greater than l is plotted in Figure 4.3 on a logarithmic scale against length. The length distribution is normalised to the mean separation D between the sources, giving a mean length of $9.5D$. However, if only the shortest 90% of separators are considered, the mean length is $7D$. It is found that the distribution of the lengths is approximately $N(l) \propto \exp(-0.12l/D)$. Only the shortest 90% of separators found are considered, since the longest separators are biased by boundary conditions, and therefore overstretch the validity of the model.

Schrijver et al. (1997) found a typical expectation value of one network concentration per area of order $A \sim 2 \times 10^8 \text{ km}^2$ for the quiet Sun. This corresponds to a value of around 14 Mm for D (a similar figure may be arrived at by using the figures for the density of ephemeral regions present in the quiet Sun obtained by Hagenaar (2001)). If only the shortest 90% of separators are considered, then this gives a mean separator length of around 100 Mm. However, if the larger of the intranetwork concentrations are included,

with strengths greater than $\sim 4.5 \times 10^{17}$ Mx, then $D \sim 8$ Mm, giving a mean separator length of around 60 Mm. By including even smaller intranetwork regions still, down to around 1.5×10^{17} Mx (the lower limit of current magnetogram images, below which the signal is indiscernible from noise), then $D \sim 4$ Mm, resulting in a mean separator length of around 30 Mm.

Figure 4.4 shows the fraction of separators with footpoint separation greater than d , again normalised to the mean source separation D . If the mean diameter of a supergranular cell is taken to be 14 Mm (Hagenaar et al., 1997), then for $D = 14$ Mm, $D = 8$ Mm and $D = 4$ Mm, it is found that $\sim 6\%$, $\sim 20\%$ and $\sim 47\%$ of separators, respectively, close within a supergranule cell, with the remaining separators forming more distant connections. The dashed line in Figure 4.4 represent the function $N(d) \propto \exp(-0.24d/D)$, and is fitted to the shortest 60% of separators.

The density of separators per unit area, N_A , may be obtained by dividing the total number of separators in the region by the area of the region. This gives a density of $N_A = 5.46/D^2$ Mm $^{-2}$. For a mean supergranular diameter of 14 Mm, the number of separators per supergranule cell is typically around 5, 17 and 52 for the values of 14 Mm, 8 Mm and 4 Mm for D , respectively. This model, however, neglects the effects of supergranular flows on the positioning of photospheric fragments, which tend to sweep magnetic flux into the intergranular lanes. Similarly, the differences in both source strength and spatial distributions that arise when considering sources at varying scales are also ignored.

4.3.3 Separator Bunching

The plot in Figure 4.5 demonstrates an interesting feature common in complex potential magnetic fields: separators can be seen to leave a null bunched closely together in trunks, only to diverge further from the null. This effect has already been observed in the case of upright nulls in a single-polarity field by Beveridge et al. (2003). However, here it is shown that it is also common in general mixed-polarity fields, and that it happens too with prone and coronal nulls.

In order to show mathematically that this effect is commonplace, the angles from which the separators leave their respective nulls are noted. Then, for each null in turn that has its fan plane sectored by more than one separator, the quantity

$$\phi_{i,j} = \frac{|\theta_i - \theta_j|n}{2\pi} = \frac{d\theta_{i,j}n}{2\pi}, \quad (4.3)$$

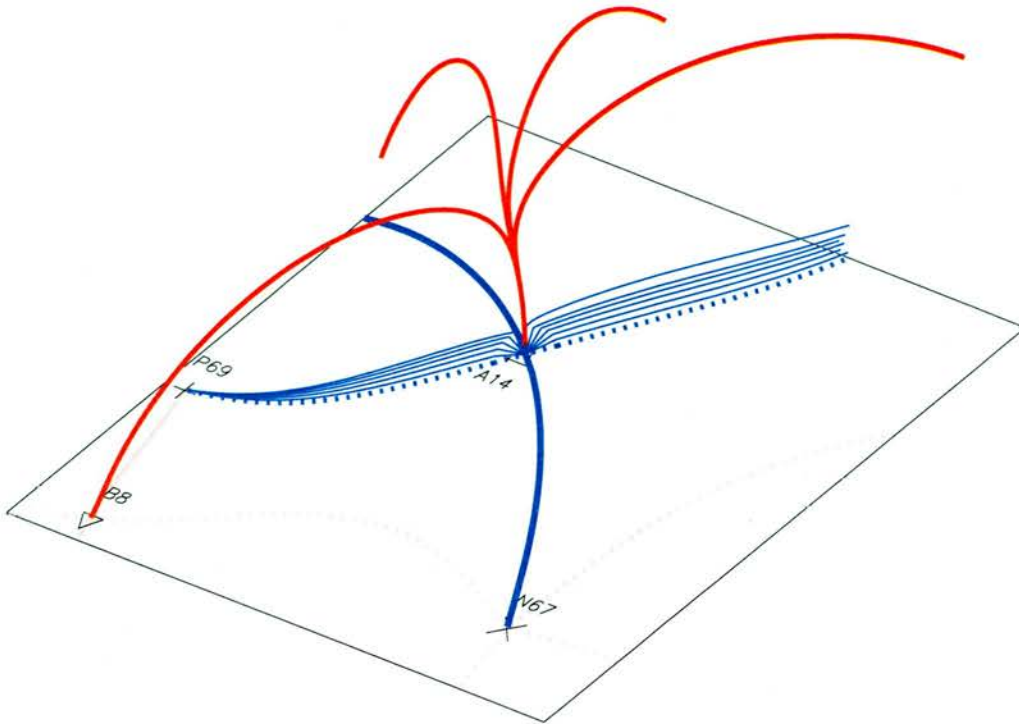


Figure 4.5: Plot of one of the prone photospheric nulls that arises in the model field, A14. The solid blue lines are a selection of fan field lines and the thick solid blue lines are spine curves. The dotted blue lines are fan field lines lying in the $z = 0$ plane, whilst the red lines are separators. The thick solid grey lines and the dotted grey lines are spine field lines and footprint fan field lines (respectively) from other nulls in the field. The plus sign is the positive source P69 and the cross is the negative source N67; the upward pointing triangle is the negative null A14 and the downward pointing triangle is the positive null B8. An animation showing a 3D rotational view about this configuration is provided on the accompanying CD (see Appendix F for details on how to access it).

is considered for all pairings of separators i and j ($i \neq j$), where θ_i and θ_j are the starting angles in the fan plane for separators i and j , respectively, and n is the number of separators connected to the null in question. Note that, since it is easier to analyse data scattered on a circle rather than just a semicircle, separators lying in sections of the fan planes of prone nulls that lie below the $z = 0$ plane are also included in this calculation. All the $\phi_{i,j}$ are calculated for each of the nulls in turn, and the results are shown in a histogram in Figure 4.6.

If the separators were distributed uniformly about the fan plane of each null, then the histogram in Figure 4.6 would climb steadily from zero at $\phi_{i,j} = 0$ and peak at around $\phi_{i,j} = 1$, since two consecutive points scattered uniformly on a circle should be separated, on average, by an angle $2\pi/n$. (only the interval $[0,1]$ is considered, since n varies from null to null and hence the function $\phi(d\theta)$ becomes rather meaningless outwith $[0,1]$). However, on the contrary, it is found that the histogram peaks at around zero, implying

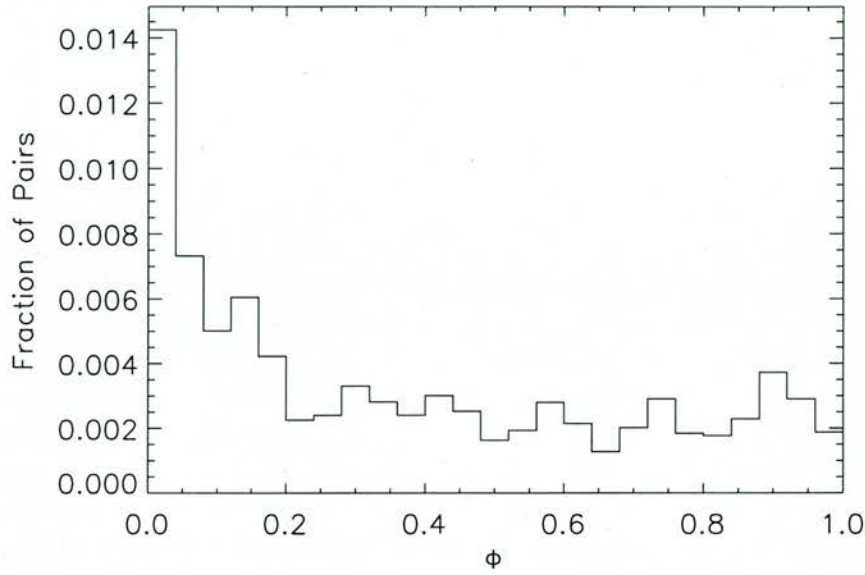


Figure 4.6: Histogram of the quantity $\phi_{i,j} = |\theta_i - \theta_j|n/2\pi$ in the range $[0,1]$ for the pair of separators i and j ($i \neq j$) starting from angles θ_i and θ_j , respectively, about a particular null with n separators.

that the separators have a tendency to bunch together.

This still leaves the question as to why such behaviour occurs, though. In order to address this question, it is assumed that it is related to the effect that causes fan field lines to group together and only partially outline fan surfaces, explained by Parnell et al. (1996).

The field at a point $\mathbf{r} = \mathbf{r}_0 + \delta\mathbf{r}$ near a null point in a potential field can be written linearly as $\mathbf{B}(\mathbf{r}) = \mathbf{M} \cdot \mathbf{r} = \mathbf{M} \cdot (\mathbf{r}_0 + \delta\mathbf{r}) = \mathbf{M} \cdot \delta\mathbf{r}$, where

$$\mathbf{M} = \begin{pmatrix} \frac{\partial B_x}{\partial x} & \frac{\partial B_x}{\partial y} & \frac{\partial B_x}{\partial z} \\ \frac{\partial B_y}{\partial x} & \frac{\partial B_y}{\partial y} & \frac{\partial B_y}{\partial z} \\ \frac{\partial B_z}{\partial x} & \frac{\partial B_z}{\partial y} & \frac{\partial B_z}{\partial z} \end{pmatrix} = \begin{pmatrix} \lambda_1 & 0 & 0 \\ 0 & \lambda_2 & 0 \\ 0 & 0 & \lambda_3 \end{pmatrix}. \quad (4.4)$$

The field may also be expressed in terms of a parameter u , giving a field line equation

$$\frac{d(\delta\mathbf{r})}{du} = \mathbf{B} = \mathbf{M} \cdot \delta\mathbf{r}. \quad (4.5)$$

Suppose, without loss of generality, that λ_1 and λ_2 are the two same-signed eigenvalues of the matrix \mathbf{M} that correspond to the fan plane of the null, and that the spine field line

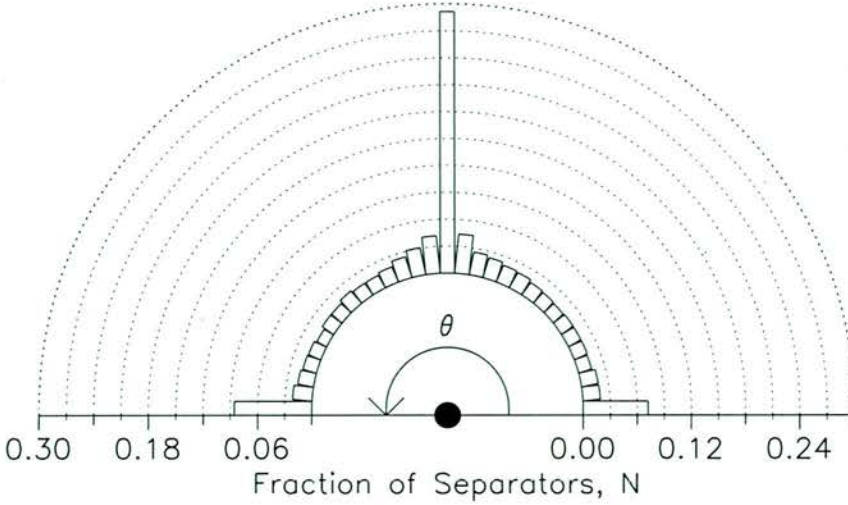


Figure 4.7: Circular histogram showing the fraction of separators N that start from a given angle θ about the fan planes of prone nulls.

is normal to the x - y plane. Then, if δr lies in the fan plane of the null, one may write

$$\begin{pmatrix} d(\delta r_1)/du \\ d(\delta r_2)/du \end{pmatrix} = \begin{pmatrix} \lambda_1 & 0 \\ 0 & \lambda_2 \end{pmatrix} \begin{pmatrix} \delta r_1 \\ \delta r_2 \end{pmatrix}. \quad (4.6)$$

Solving this gives rise to two expressions, namely

$$\delta r_1 = \delta r_{10} e^{\lambda_1 u}, \quad (4.7)$$

$$\delta r_2 = \delta r_{20} e^{\lambda_2 u}, \quad (4.8)$$

the ratio of which is

$$\frac{\delta r_1}{\delta r_2} = \frac{\delta r_{10}}{\delta r_{20}} e^{(\lambda_1 - \lambda_2)u}. \quad (4.9)$$

In the cases when $\lambda_1 \gg \lambda_2$, fan field lines will tend to be preferentially aligned with the direction r_1 in which the field is strongest; however, separator field lines tend to lie in the channels of weak field, since they, by definition, link pairs of null points, and will be preferentially aligned with the direction r_2 . The grouping of separators into channels of weak field will show exponential convergence as $|\lambda_1 - \lambda_2|$ increases.

This explanation, in which the separators tend to form trunks along the fan plane eigenvector with the smaller eigenvalue, implies that, in the case of prone nulls, there are only two directions along which separators will tend to bunch: either parallel to the photospheric plane or perpendicular to it. This is due to the symmetry that exists about the

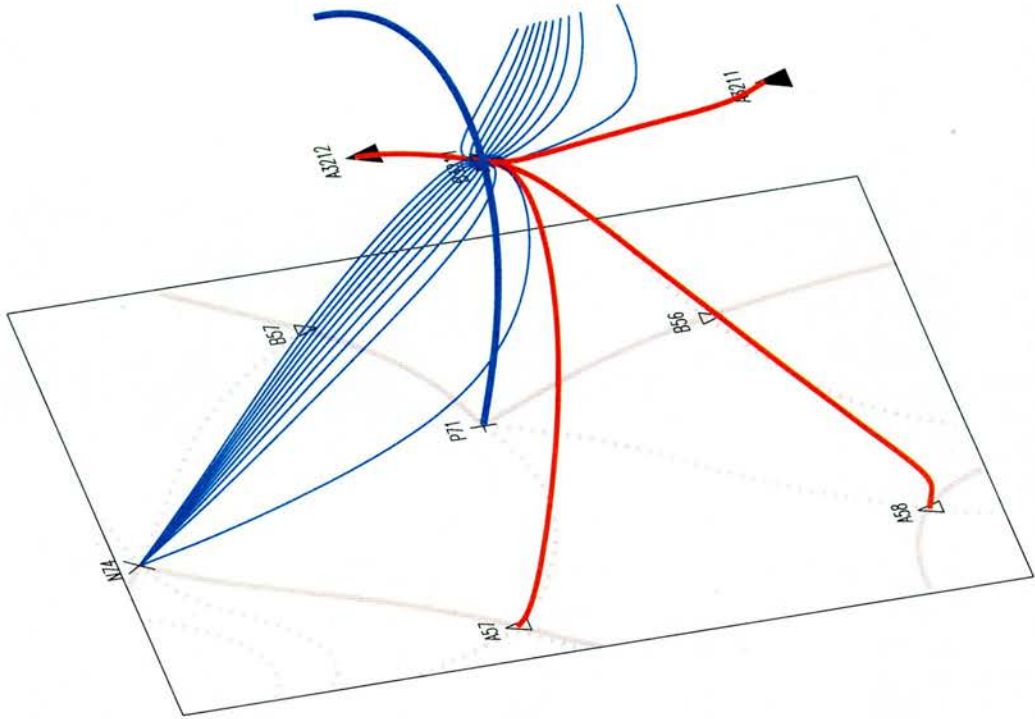


Figure 4.8: Plot of a coronal null, B3211, that is connected to two opposite-polarity coronal nulls, A3211 and A3212. Figure 4.5 gives an explanation of the symbols and line styles. Coronal nulls are shaded black to distinguish them from photospheric nulls. An animation showing a 3D rotational view about this configuration is also available on the accompanying CD.

$z = 0$ plane. Figure 4.7 shows a circular histogram of the starting angles for separators about the fan planes of prone nulls, and shows that the preferred angles are indeed $\theta = 0$, $\theta = \pi/2$ and $\theta = \pi$.

The angles which are obtained for the starting points of the separators about the nulls are, of course, highly dependent on the radius of the ring about which the fan plane of the null is scanned. Thus, if a much smaller radius were to be taken, then it's likely that the behaviour illustrated in Figure 4.7 would be more pronounced. However, it is not suggested here that for every null one should expect the separators to form trunks; indeed, when the two fan-plane eigenvalues are comparable in size, then the separators will be free to leave the fan plane in any direction.

In practice, it is found that separators bunched together about a null diverge at varying stages. Some grouped separators may diverge very close to the null, whereas at the other end of the scale, pairs of separators may remain grouped together right up until they are in the vicinity of another null, where they then split, with one connecting to the aforementioned null and the other going off to connect to a different null.

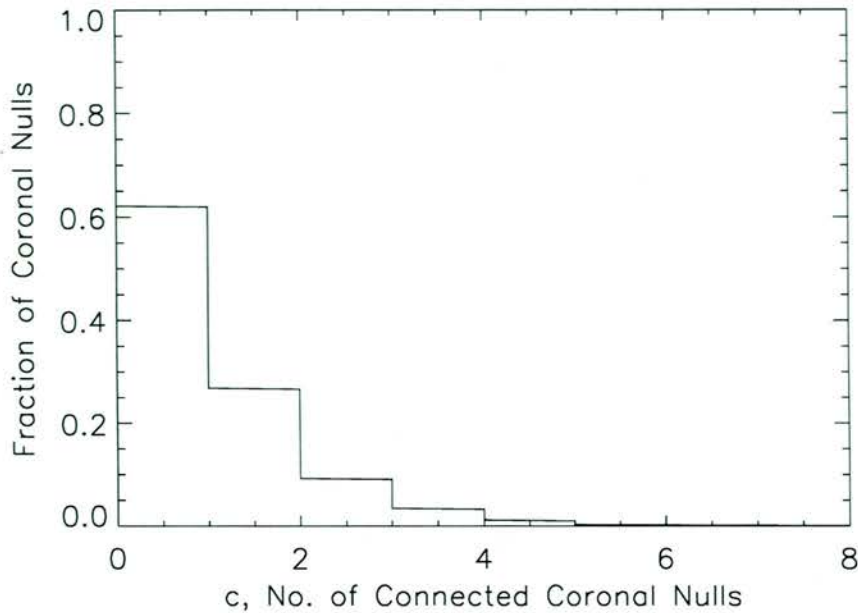


Figure 4.9: Fraction of coronal nulls connected to c or more other opposite-polarity coronal nulls.

4.3.4 Connections between Coronal Nulls

In quiet-Sun fields, the tireless motions of magnetic flux elements mean that the structure of the magnetic field is always changing, with bifurcation after bifurcation constantly redefining the topological skeleton.

Coronal nulls, in particular, will naturally come and go. Since they are believed to be important sites for reconnection, and may play a crucial role in a variety of solar phenomena, such as X-ray bright points and solar flares, a good understanding of how they come about is of great importance.

Until recently, the only known mechanism that could explain how coronal nulls come into existence was the local double-separator bifurcation (Brown and Priest (1999a)), where coronal nulls are born in the photosphere and rise into the corona.

Lately, though, a new explanation for the birth of coronal nulls has emerged from Beveridge (2003), who demonstrated how purely coronal bifurcations can give rise to nulls points. It was shown, for example, how a five-source configuration can produce an unstable second-order null in the corona, which in turn splits into two stable first-order nulls. The study then went on to demonstrate a bifurcation by which a seven-source configuration containing two nulls can change to one with four nulls, which, moreover, may bifurcate into one with 6 nulls.

In this section, the aim is to examine which mechanism is the more likely cause for

coronal nulls to appear. The work here is based on the following observation made by Beveridge (2003): nulls which are produced by coronal bifurcations are likely to remain connected by separator field lines after the bifurcation, whereas coronal nulls created in the plane by the local double-separator bifurcation will not be connected to any other coronal nulls. Furthermore, the scenario in which an unstable second-order null which has just been born out of a coronal bifurcation may be encountered will be discarded as highly unlikely.

By examining the endpoints of separators traced from coronal nulls, the number of coronal nulls that are connected to other coronal nulls by separator field lines is established. Figure 4.8 shows an example of a coronal null that is connected to two opposite-polarity coronal nulls.

On average, 2.85 coronal nulls are found in the inner region containing 32 mixed-polarity sources. Figure 4.9 shows the fraction of coronal nulls connected to c or more other coronal nulls. It is found that each coronal null is connected to, on average, 1.03 ± 0.07 other coronal nulls, with the maximum number of connections being 8. Only 38% of coronal nulls are found to be connected to no other coronal nulls at all.

These findings therefore give a strong indication that coronal bifurcations are commonplace, and are most likely the preferred method by which coronal nulls are produced.

The results here show that a coronal null may be connected to a varying number of coronal nulls. Thus, further work is needed to generalise the theory so that the key processes that cause an arbitrary number of coronal nulls to appear may be clearly understood.

4.4 An Observed Sequence of Magnetograms

In this section, the fields observed in magnetogram images are analysed by representing each of the magnetic fragments as a single point source.

A sequence of 50 magnetograms is examined, each 240×240 Mm, from 17 August 1997. Each image is spaced by 15 minutes and contains, on average, 286 fragments per frame. The region is chosen so that it is roughly in flux balance, although there is an average imbalance of $(\text{total positive flux})/(\text{total flux}) \approx 0.45$, hence there is some open negative flux. Again, only the central $\frac{1}{3} \times \frac{1}{3} \times \frac{1}{6}$ region is searched.

In the quiet-Sun network, fragments, rather than being randomly scattered over the

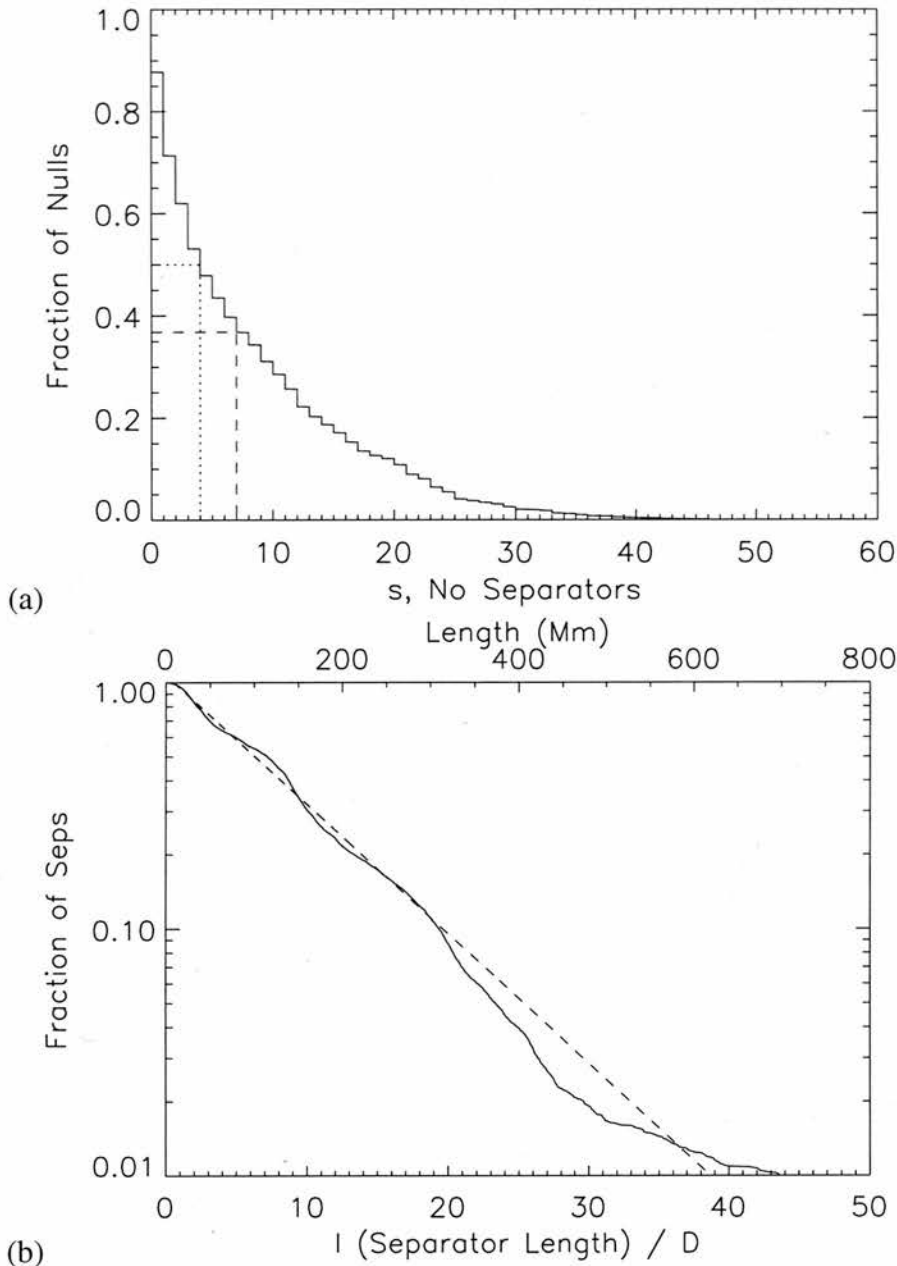


Figure 4.10: (a) Fraction of nulls with number of separators greater than s . Specific values are given for the fractions 0.5 (dotted line) and for the mean number of connected separators (dashed line). (b) Fraction of separators with length greater than l , normalised with respect to the mean source separation, D (lower axis). The upper axis gives the lengths in megametres. The dashed line represents the function $y = 1.07 \exp(-0.12l/D)$ and is fitted to the shortest 90% of separators.

solar surface, tend instead to cluster around supergranular boundaries. With this in mind, all the null points in the inner $80 \times 80 \times 40$ Mm region are calculated. Since a restriction cannot be placed on the minimum distances between sources as was possible with the Monte Carlo experiments of Section 4.3, a search grid of dimensions $1000 \times 1000 \times 500$

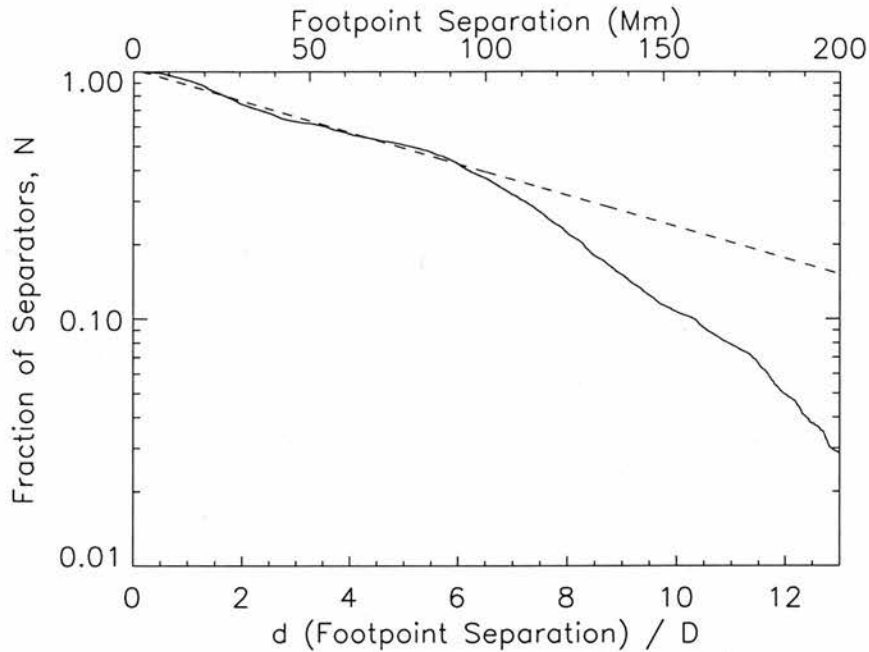


Figure 4.11: Fraction of separators with footpoint separation greater than d , normalised with respect to the mean source separation, D (lower axis). The upper axis gives the distances in megametres. The dotted line represents the function $y = 1.02 \exp(-0.15d/D)$ and is fitted to the shortest 60% of separators.

is adopted, so that nulls situated between fragments that are in close proximity to each other may be identified.

A total of 1.051 ± 0.007 nulls per source are discovered, with 1.013 ± 0.008 (96%) lying in the source plane and 0.038 ± 0.005 (4%) occurring in the corona. Initially, these figures seem alarmingly different from those obtained in Section 4.3; however, it must be remembered that this is a relatively small sample (50 magnetograms), and, since it is a sequence that covers a fairly short time span (12.5 hours) that follows the evolution of the field, the regions won't vary all that greatly from one magnetogram to the next. Thus, although this region is analysed as a case study of what may be expected from more realistic coronal fields, care should be taken not to assume that the results obtained are generic for observed magnetic fields.

4.4.1 Separator Distributions

Shown in Figure 4.10(a) is the fraction of nulls with a total number of connected separators greater than or equal to s . A lower density of separators than the 10.1 separators per null previously found Section 4.3 is observed here— on average, there are 7.63 ± 0.20 separators per null, of which 0.99 ± 0.059 are multiply connecting separators. The fig-

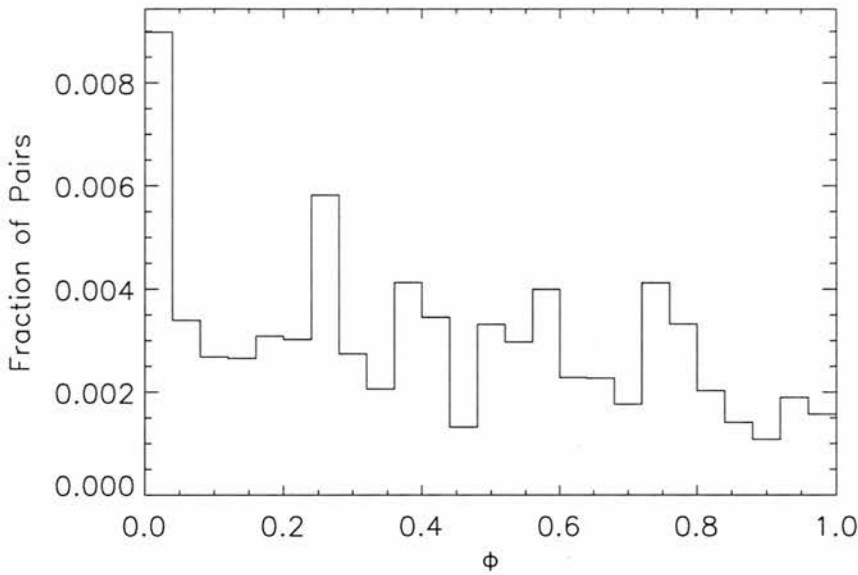


Figure 4.12: Histogram of the quantity $\phi_{i,j}(d\theta) = |\theta_i - \theta_j|/n/2\pi$ in the range $[0,1]$ for the pair of separators i and j ($i \neq j$) starting from angles θ_i and θ_j , respectively, about a particular null with n separators.

ures for coronal nulls and planar nulls are quite similar— there are 7.65 ± 0.21 separators per planar null, with 1.03 ± 0.061 multiply connecting, whilst 7.11 ± 0.39 separators per coronal null are found, although only 0.11 ± 0.038 are multiply connecting. These figures, lower than the averages found in Section 4.3, are partly explained by noting that 0.12 ± 0.021 nulls per source have unbroken fan surfaces, giving rise to isolated domes. This accounts for 12.5% of all nulls— around 7 times greater than the figure of 1.8% found in Section 4.3. Further investigation is required in order to establish whether this anomaly is an effect common to observed quiet-Sun fields, or if it is just specific to the case studied here.

The distribution showing the fraction of separators with lengths greater than or equal to l is shown in Figure 4.10(b), with the fractions shown on a logarithmic scale. It is found that the distribution of lengths is surprisingly close to the earlier distribution obtained in Section 4.3— the curve fitted here corresponds to a distribution $N(l) \propto \exp(-0.12l/D)$, which of course in this scenario may also be expressed as $N(L) \propto \exp(-0.009L)$, where L is measured in megametres. The mean separator length is found to be 113.2 Mm (7.57 times the average source separation).

Similarly, the distribution showing the fraction of separators with footpoint separations greater than or equal to d is shown in Figure 4.11. As previously, the shortest 60% of separator footpoint separations is observed to follow an exponential distribution, with the distribution of footpoint separations here being $N(d) \propto \exp(-0.15d/D)$. This may

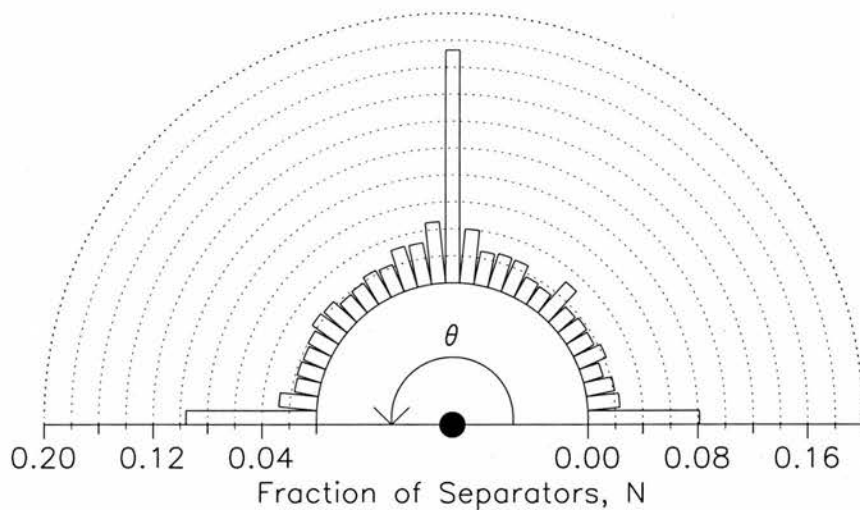


Figure 4.13: Circular histogram showing the fraction of separators N that start from a given angle θ about the fan planes of prone nulls.

also be rewritten as $N(S) \propto \exp(-0.011S)$, where S is measured in megametres.

Figure 4.12 shows a histogram of the function (discussed previously in Section 4.3)

$$\phi_{i,j} = \frac{|\theta_i - \theta_j|n}{2\pi} = \frac{d\theta_{i,j}n}{2\pi},$$

applied to the scenario here, where θ_i and θ_j are the starting angles for separators i and j , respectively, and n is the number of separators connected to the null in question. All the $\phi_{i,j}$ for each of the nulls are calculated in turn. As was the case in Section 4.3, it is also found that the peak of the histogram is centred on 0 rather than 1, so that separator bunching is also abundant in these fields. Figure 4.13 shows a circular histogram of the starting angles for separators about the fan planes of prone nulls. Again, it is clear that the preferred angles are $\theta = 0$, $\theta = \pi/2$ and $\theta = \pi$. Although the plot here has more significant contributions away from these angles than there were in the Monte Carlo simulation, suggesting that there isn't as much separator bunching here, the fact that the starting angles are so sensitive to the radius of the disk taken when scanning the fan planes prevents us from reading too much into this.

It is found here that, on average, each coronal null connects to 0.12 ± 0.016 other coronal nulls, with any given coronal null connecting to a maximum of 1 other coronal null. This figure is in stark contrast to the value of 8 found in Section 4.3. This should not be too surprising, though; a lower density of coronal nulls is also found in general, so there simply aren't enough coronal nulls to provide many more connections.

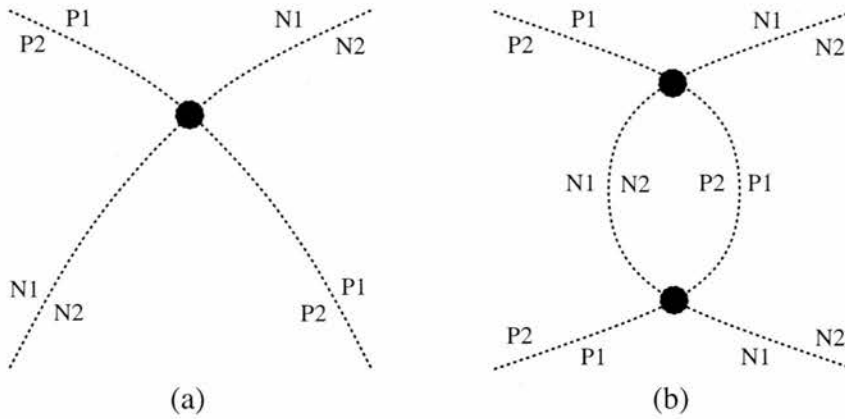


Figure 4.14: (a) Cross section about a typical separator field line. Dotted lines correspond to fan surfaces, whilst the black filled dot is the separator. The flux from sources P1 and P2 is separated by one separatrix wall, and the flux from N1 and N2 is separated by the other. (b) Cross section of two separators linking a common pair of nulls. Note that there are two regions connecting P1 and N1.

4.5 Conclusions

The study here has shown that magnetic separators— strong candidates as locations for energy dissipation in the Sun’s atmosphere— are more abundant than previously thought. One reason found for this is that pairs of nulls can be connected by more than one separator field line. Figure 4.14 shows how the presence of a pair of nulls connected by more than one separator field line results in two opposite-polarity sources being connected by two distinct regions. The separatrix wall separating the flux from P1 and P2 breaks through the one which separates flux from N1 and N2, only to break through it again. Thus, there are two domains through which source P1 may connect to source N1. It is not difficult to imagine this occurring in practice, since fan surfaces are often contorted into elaborate, warped surfaces as they weave their way through complicated magnetic fields.

By analogy with the sources themselves, it is found that some null points too are busier junctions of connectivity than others. It is found in this study of model fields with an exponential flux distribution that 1.8% of nulls connect to no other nulls, whilst one particular null has 100 connected separators. Slightly contrasting results are obtained when an observed sequence of magnetograms is analysed; 12.5% of null fan surfaces are unbroken by separator field lines, whilst the maximum number of connections from a given null is 46.

It has been shown that in many cases, separators leave fan planes bunched together into trunks that lie in a narrow channel. This is due to gradients in the field around the

null, so that separators are grouped into regions where the field is weaker.

Further investigation is required to establish whether the discrepancies between the two sets of findings are truly the result of the spatial distribution of magnetic flux fragments in the photosphere along supergranular boundaries, or whether it is just an artifact of the specific observed data that is analysed here.

Chapter 5

Coronal Flux Recycling Times[†]

加 舎 白 雄	か	二	啼	One cuckoo sings
	ん	つ	け	Then responds another
	こ	の	ば	
	鳥	山	鳴	Between the two mountains
		の	く	

KAYA SHIRAO (1738–1791)

5.1 Introduction

The four key processes that characterise the quiet-Sun photosphere— emergence, coalescence, fragmentation and cancellation— will undoubtedly have consequences for the magnetic field in the corona above. Hence, the aim of this chapter is to gauge the effect of the behaviour of the photospheric flux fragments on the quiet-Sun corona.

Observations have shown that the outer atmosphere of the Sun, the corona, is heated to a temperature of several million Kelvin, some two orders of magnitude hotter than the chromosphere below. It is believed that the energy required for such heating originates in the turbulent convection zone below the photosphere. This energy is channelled through the solar surface into the chromosphere and corona by the magnetic field.

Above the photosphere, new flux is seen to be constantly emerging. This is matched by continual cancellation between coalesced and fragmented flux concentrations, so that the picture that emerges is one of a very dynamic quiet-Sun magnetic field. Schrijver et al. (1997) showed that observed source flux distributions are not consistent with a source

[†]The work in this chapter was published as a letter in Vol. 612 of *The Astrophysical Journal* (Close et al., 2004a).

function that is just the distribution of flux that disappears from the solar surface. Hence, the magnetic fields are not simply bobbing up and down through the photosphere, and are instead continually being reprocessed. Supergranular flows sweep magnetic fields to supergranular cell boundaries, fragmenting, cancelling or coalescing them along the way. Upon reaching a cell boundary, flux fragments then move along the boundary with the flow along it and are again subjected to fragmentation, cancellation or coalescence. (See Subsection 1.2.1 for further details).

The complicated motions of magnetic flux fragments in the quiet-Sun network will drive reconnection higher in the upper atmosphere, as magnetic fields constantly realign themselves in response to the ever-changing footpoint configurations. Moreover, new flux that emerges through the photospheric surface is likely to, at some stage, reconnect with the overlying field.

Reconnection driven by the magnetic carpet is important, since it is thought that this is the mechanism by which the ambient corona is heated (Levine, 1974; Parker, 1981, 1983, 1988; Parnell and Priest, 1994; Parnell and Priest, 1995; Schrijver et al., 1998; Longcope and Kankelborg, 1999; Priest et al., 2002; Priest et al., 2003). It may also play a role in several quiet-Sun coronal events (such as X-ray bright points, X-ray jets and nanoflares), as well as accelerating the fast solar wind (McKenzie et al., 1995).

Thus, the aim of this study is to try to put a handle on the amount of reconnection that occurs as a consequence of the dynamic nature of the magnetic carpet. This is approached by taking observed magnetograms, identifying and tracking individual fragments, and extrapolating the magnetic field using a potential field approximation. By comparing domain fluxes between successive magnetogram images, the amount of reconnection that must have taken place to move from one configuration to the next is gauged. Section 5.2 discusses how photospheric flux fragments are treated using the general approach of Longcope (2001) for mapping the connectivity of the field, whilst Section 5.3 details various assumptions in the analysis. This is followed up with an analysis whereby emergence and cancellation are prohibited in Section 5.4. Section 5.5 starts with a discussion regarding changes in source fluxes, which is followed by a calculation of the flux recycling time due to emergence and cancellation. An estimate of the amount of reconnection that takes place when emergence and cancellation are allowed is then presented. The study is rounded off with a discussion of energy dissipation due to separator reconnection in Section 5.6. A concluding discussion is given in Section 5.7.

5.2 Photospheric Flux Fragments

To study the effects of granular and supergranular flows on the connectivity of magnetic-carpet fields, a sequence of high-resolution MDI magnetograms (each 240×240 Mm) is used for the analysis, and the central 80×80 Mm area is studied. After averaging over sequences of 15-magnetograms spaced by 1 minute (in order to reduce the effects of 5 minute oscillations), this leaves a series of 50 magnetograms, each spaced by 15 minutes and covering a 12-hour period.

Discrete fragments are located spatially and labelled in each of the 50 magnetograms in turn. On average, there are 286 fragments in total per frame, although naturally this number varies from frame to frame. Subsequent magnetograms are then compared in order to track the motions of individual fragments. Thus, the unique labels given to each fragment are projected temporally through the set of magnetograms (Parnell, 2004).

Since magnetograms show that photospheric magnetic field is generally assembled into isolated fragments of strong magnetic field (a small section of which is illustrated in Figure 5.1(*left*)), with relatively little field outwith these concentrations, each fragment is represented by a single point source, placed at its centroid. Further details regarding the geometry and the approximations made here are given in Section 1.4.

As there are no magnetic monopoles within the Sun, the net flux crossing the complete solar surface must be zero. However, in a case such as the one studied here, where only a particular section of the photospheric surface is studied, there will undoubtedly be, unless one is extremely lucky, some amount of flux imbalance. Thus, if a flux imbalance in a particular region is found, and the sum of all the source fluxes is

$$\sum_a \Phi_a = \Phi_{Tot}, \quad (5.1)$$

then this requires the inclusion, at infinity, of a source with flux $-\Phi_{Tot}$. Thence, each system may be considered to be in flux balance.

Aside from topologically defining field lines, such as fan field lines, spine field lines and separator field lines, every field line in the corona begins at a positive source and ends at a negative source. In this scenario, the coronal volume may be viewed as being comprised of a multitude of flux domains, each characterised by the endpoints of its field lines.

It is, of course, possible that a pair of sources may be connected by field lines from

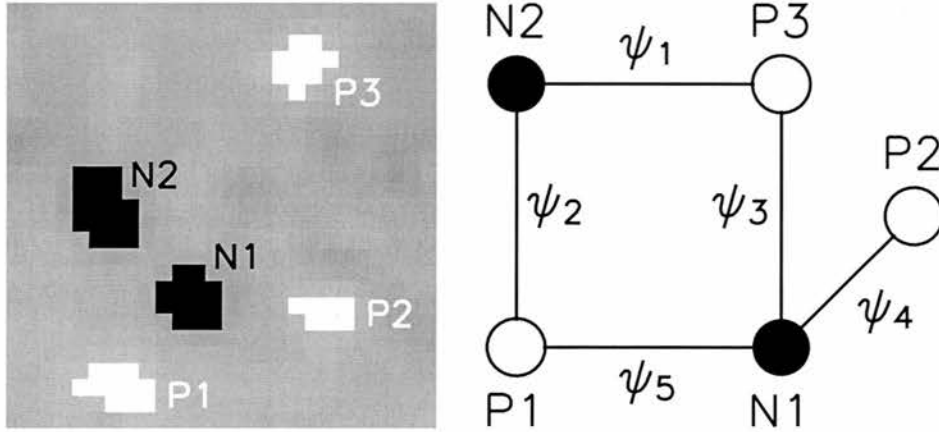


Figure 5.1: *Left*: A small section of one of the magnetogram images showing a typical quiet-Sun region containing mixed-polarity fragments. The field shown here consists of three positive fragments, P_1 , P_2 and P_3 , and two negative fragments, N_1 and N_2 . The background shown in grey is, by comparison with the flux fragments, unmagnetised. *Right*: A possible domain graph for the region, with the domain fluxes ψ_i ($i = 1 \dots 5$) indicated.

multiple domains. However, in this study, only changes in the total flux connecting pairs of sources will be considered, and any reconnection that relates to reapportionment of flux between any multiple domains connecting the given pair of sources will be neglected, just as any redistribution of field lines within domains will not be accounted for.

The fluxes of the N_d domains that interconnect the N_s sources will be denoted by ψ_n . If a source a is considered, with a flux Φ_a , then the N_d domain fluxes may be related to the flux of source a through the incidence matrix

$$\Phi_a = \sum_{n=1}^{N_d} M_{an} \psi_n. \quad (5.2)$$

The domain fluxes ψ_n are defined as positive quantities. An *unsigned-flux convention* is adopted here, whereby $\Phi_a > 0$ for all sources, and the entries in M_{an} are either +1 or 0. Longcope and Klapper (2002), by contrast, use a *signed-flux convention*, where $\Phi_a < 0$ if a is a negative polarity source, and along the corresponding row $M_{an} = -1$ for each domain n connected to it. The unsigned-flux convention is adopted here so as to avoid confusion with the terms “increase” and “decrease” when referring to changes in source fluxes. This will become important when comparing emergence and cancellation of flux in a given domain with reconnection in that domain.

Figure 5.1(*right*) shows an example of how a magnetic field may be interpreted in

terms of graph theory. In this example,

$$M = \begin{matrix} & \mathcal{D}_1 & \mathcal{D}_2 & \mathcal{D}_3 & \mathcal{D}_4 & \mathcal{D}_5 \\ \begin{matrix} P1 \\ P2 \\ P3 \\ N1 \\ N2 \end{matrix} & \begin{pmatrix} 0 & 1 & 0 & 0 & 1 \\ 0 & 0 & 0 & 1 & 0 \\ 1 & 0 & 1 & 0 & 0 \\ 0 & 0 & 1 & 1 & 1 \\ 1 & 1 & 0 & 0 & 0 \end{pmatrix} \end{matrix}, \quad (5.3)$$

where \mathcal{D}_i denotes the domain within which the flux ψ_i is contained. The relationship (5.2) may be stated more explicitly as

$$\begin{pmatrix} \Phi_1 \\ \Phi_2 \\ \Phi_3 \\ \Phi_4 \\ \Phi_5 \end{pmatrix} = \begin{pmatrix} 0 & 1 & 0 & 0 & 1 \\ 0 & 0 & 0 & 1 & 0 \\ 1 & 0 & 1 & 0 & 0 \\ 0 & 0 & 1 & 1 & 1 \\ 1 & 1 & 0 & 0 & 0 \end{pmatrix} \cdot \begin{pmatrix} \psi_1 \\ \psi_2 \\ \psi_3 \\ \psi_4 \\ \psi_5 \end{pmatrix}. \quad (5.4)$$

5.3 Analysis

The sequence of 50 magnetograms gives a total of 49 sets of consecutive pairs of magnetograms with which to compare domain fluxes. Henceforth, the first magnetogram in a pair will be denoted with the letter 'i' for initial, and the second magnetogram with the letter 'f' for final. In order to obtain the domain fluxes ψ_n , the same method as that of Chapter 2 is used. This involves calculating a number of field lines from starting points close to each source. (The method by which starting points are determined is given in Section 2.2). Hence, from each source within the inner region, m field lines are traced, with m equal to the integer part of ϵ/ϵ_1 (where $\epsilon_1 = 7.73 \times 10^{15} Mx$). Thus, each field line represents essentially the same amount of flux.

The connectivity for each magnetogram is stored in a connectivity matrix, where columns represent positive-polarity fragments and rows represent negative fragments. Naturally, the nature of the connectivity matrix will change from one magnetogram to the next, as fragments may emerge, fragment, coalesce or cancel from one magnetogram to the next. Thus, positive and negative index vectors are kept for each frame, and the history of which fragments have fragmented and which have coalesced is also stored. This enables a comparison of domain fluxes for each of the 49 pairs. To accommodate for the fact that field lines may close outwith the inner region, all the flux represented by such

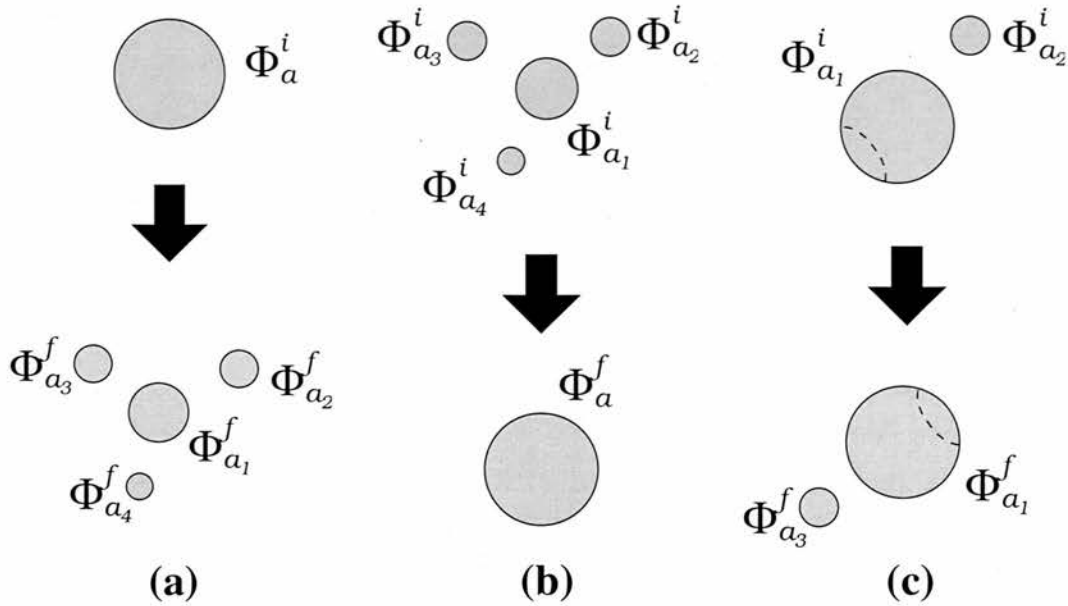


Figure 5.2: Sketches of the possible scenarios that may arise when (a) a single fragment in frame i has split into several smaller fragments by frame f , (b) several fragments in frame i have coalesced into a single, larger fragment by frame f , and (c) several fragments coalesce to form a single, larger fragment in frame i , whilst this single fragment has split into several smaller fragments by frame f . The various Φ values represent the flux in the given fragments.

field lines is recorded in the connectivity matrix; however, only half the flux represented by a field line closing within the inner region is recorded because, at least in optimal conditions, the other half of the flux represented will be recorded when tracing back from the fragment at which the field line closed. Thus, all the flux within the inner region studied is accounted for.

5.3.1 Comparing Magnetogram Pairs

Taking each pair of magnetograms in turn, the aim is to have, for every fragment in frame f , a corresponding fragment in frame i , and vice versa. However, a complication arises due to the fact that fragments may split or coalesce. The exact cause of fragmentation is not clear, but it is suspected that granulation may play a role (Parnell, 2001). A given network element may cover a region containing as many as 25 granules, so it is quite probable that granulation flows will constantly buffet the many intense flux tubes comprising the magnetic fragments, resulting in a continual redistribution of the flux within each fragment. Supergranular flows will tend to hold these fragments together as they drift towards the downflow regions at supergranular boundaries. However, whenever there is a weakening in the supergranular flows, then granular motions will prevail, causing fragmentation

to occur.

Sketched in Figure 5.2 are three possible scenarios that may occur involving fragmentation and coalescence. Figure 5.2(a) shows a fragment in frame i that has split into several smaller fragments by frame f . Figure 5.2(b) shows the converse of this, where several distinct fragments in frame i have coalesced into a single larger fragment by frame f . However, a third possibility, shown in Figure 5.2(c), is that several fragments in frame i coalesce into a single, larger fragment, which itself is viewed to have split by frame f . Note the suggestion here is that coalescence occurred, followed by fragmentation. Of course, one cannot know what happened between frames, so it is equally plausible that fragmentation occurred, followed by coalescence. Indeed, both processes may have occurred at the same time. However, the way such cases are treated is independent of the order of the processes.

Fragmentation and coalescence may be dealt with in the following way. Consider two fragments, a and b , in frame f , with fluxes Φ_a^f and Φ_b^f , respectively. If these two fragments are connected by an amount ψ_n^f , then the change in the flux connecting a and b from frame i to frame f may be written as

$$\Delta\psi_n = \psi_n^f - \kappa_A\kappa_B\psi_N^i. \quad (5.5)$$

The term $\kappa_A\kappa_B\psi_N^i$ is essentially ψ_n^i , the amount of flux connecting the equivalents of the fragments a and b in the frame i . The values of κ_A and κ_B , which deal with fragmentation, and ψ_N^i , which deals with coalescence, are found in the following manner. If fragment a in frame f has been formed by fragmentation, then

$$\kappa_A = \frac{\Phi_a^f}{\Phi_A^f}, \quad (5.6)$$

where Φ_A^f is the sum of the fluxes of all the fragments that were involved in the fragmentation. Otherwise $\kappa_A = 1$. κ_B is defined in a similar way for the fragment b . Thus, it is assumed that, at the point of fragmentation, each fragment receives a portion of the connected flux proportional to its own flux strength.

The value of ψ_N^i is defined in one of the following three ways:

1. If both the fragments a and b consist of fragments that coalesced between the frames

i and f , then

$$\psi_N^i = \sum_{j,k} \text{Flux connecting } a_j^i \text{ to } b_k^i,$$

where the a_j^i are the fragments associated with a that have coalesced by frame f , and the b_j^i are the fragments associated with b that have coalesced by frame f .

2. If only a consists of fragments that coalesced between the frames i and f , then

$$\psi_N^i = \sum_j \text{Flux connecting } a_j^i \text{ to } b^i,$$

where the a_j^i are the fragments associated with a that have coalesced by frame f , and b^i is the fragment associated with b in frame i .

3. If neither a nor b consist of fragments that coalesced between the frames i and f , then

$$\psi_N^i = \text{Flux connecting } a^i \text{ to } b^i,$$

where a^i is the fragment associated with a in frame i , and b^i is the fragment associated with b in frame i .

Births and deaths of fragments cause a slight problem, as it is of course not possible to find corresponding fragments in both frames when fragments simply appear/disappear between frames. The way in which this problem is overcome is as follows. If a fragment in magnetogram i has died by magnetogram f , then either (i) the fragment is removed from frame i or (ii) the fragment is copied into frame f , giving it the same flux and the same position as it has in frame i . Both of these options are deployed in different scenarios later on. Fragments that are newly born in frame f are treated in an analogous manner.

5.3.2 Emergence, Cancellation and Reconnection

In complex magnetic configurations, such as those found in the mixed-polarity quiet Sun, the motions of photospheric fragments will inevitably, at the very least, lead to redistribution of flux between the domains that have their flux rooted in these fragments. Also, from a topological viewpoint, these motions will drive bifurcations, as old domains are destroyed or altered and new ones are created (Brown and Priest, 1999b, 2001; Beveridge

et al., 2002). In a potential field, the system is entirely current-free, so the configuration permits no stress and therefore changes in connectivity occur instantly. Here, however, the details of how the reconnection occurs are not considered; instead, snapshots of the field are examined as the process evolves, and regions where reconnection has occurred are identified.

The motions of the flux fragments are not the only reason for changes in domain fluxes, though. In a system as dynamic as the quiet-Sun photosphere, emergence and cancellation of flux through the photospheric boundary will also alter domain fluxes, so that the resulting changes that are recorded from one magnetogram to the next will be the net effect of emergence, cancellation and reconnection. In light of this, recycling times for coronal flux in two different scenarios are considered here. In the first, reconnection is driven purely through the motions of the fragments by prohibiting emergence and cancellation. In this case, fluxes are averaged between frames, so that fragment strengths are kept fixed and only the effects of the motions of the fragments are measured. In the second scenario emergence and cancellation are allowed, so that the fluxes of the fragments may vary between frames. Births and deaths of fragments are exceptions to this; by deploying the little tricks outlined previously, it is essentially assumed that these fragments have witnessed no emergence or cancellation. Although this will introduce slight errors into the analysis, the alternative, whereby the fragments are copied into the frame in which they are absent but have their fluxes set to zero (these would essentially be “ghost fragments”, existing solely for the purpose of quantifying the change in domain fluxes), would introduce far greater errors into the analysis. This is mainly because the cadence of the magnetogram images is not high enough to trace the deaths (births) smoothly, resulting in a vanishing effect whereby fragments suddenly disappear (appear), rather than having their strengths decrease (increase) to (from) zero. This will be discussed further later on.

From a coronal heating viewpoint, a measure of the amount of reconnection that occurs is what is of greatest interest. Changes in source fluxes are accompanied by changes in domain fluxes, related by the expression

$$\Delta\Phi_a = \sum_{n=1}^{N_d} M_{an} \Delta\psi_n. \quad (5.7)$$

This assumes that the connectivity does not change, so that, if a domain is absent from either the initial or final field, then it is simply included in the incidence matrix and given the value $\psi_n = 0$. Magnetic reconnection is a change in domain fluxes, R_n , which occurs

in the corona and therefore does not affect the source fluxes. Thus

$$\sum_{n=1}^{N_d} M_{an} R_n = 0. \quad (5.8)$$

The processes of emergence and cancellation of flux will alter the fluxes of the photospheric sources, which in turn will inject flux S_n into the domains. In general, domain fluxes combine reconnection, emergence and cancellation (the adoption of an unsigned flux convention means that $S_n > 0$ relates to emergence, while $S_n < 0$ relates to cancellation). Hence

$$\Delta\psi_n = R_n + S_n. \quad (5.9)$$

This decomposition, however, is not unique, as can easily be seen by the fact that

$$\Delta\Phi_a = \sum_{n=1}^{N_d} M_{an} S_n, \quad (5.10)$$

which is consistent with no reconnection ($R_n = 0$). Thus, in order to quantify the reconnection R_n occurring in a field in which $\Delta\Phi_a$ and $\Delta\psi_n$ are measured, additional information that allows the determination of S_n must first be introduced.

In the following section, the scenario in which emergence and cancellation of flux are prohibited is considered, so that only the time taken to recycle coronal flux due to fragment motions is measured. Section 5.5 then deals with the effects of emergence and cancellation on the recycling time of coronal flux due to reconnection.

5.4 Scenario 1: Excluding Emergence and Cancellation

Initially, fields with $\Delta\Phi_a = 0$ are considered. By Equation (5.10), this means that $S_n = 0$ for all n . This is achieved in the following way: if a fragment a is identified, which exists in both the initial and final frames, then the flux of a is adjusted in both frames so that it is equal to the mean of its values in frame i and frame f . However, since the four processes of emergence, fragmentation, coalescence and cancellation occur, this must also be taken into account when adjusting the fluxes.

Generally, if fragments that are born or die between frames i and f are excluded, the fluxes in frame i are adjusted in one of the following 2 ways:

1. If the fragment a in frame i is not just about to coalesce, then its flux Φ_a^i is adjusted such that

$$\Phi_a^i \rightarrow \frac{\Phi_A^f + \Phi_a^i}{2},$$

where Φ_A^f is its corresponding flux in the frame f . If the fragment a is not about to fragment, then $\Phi_A^f = \Phi_a^f$, the fragment's flux in frame f . If a is just about to fragment, then

$$\Phi_A^f = \sum_{j=1}^p \Phi_{a_j}^f,$$

where $\Phi_{a_j}^f$ are the fluxes of the p fragments into which a fragments.

2. If m fragments in frame i are just about to coalesce, then the fluxes of each of the a_j fragments ($j = 1, \dots, m$) are adjusted such that

$$\Phi_{a_j}^i \rightarrow \frac{\Phi_{a_j}^i}{\Phi_A^i} \left(\frac{\Phi_A^f + \Phi_A^i}{2} \right),$$

where Φ_A^f is as previously defined and

$$\Phi_A^i = \sum_{j=1}^m \Phi_{a_j}^i,$$

namely, the sum of the fluxes of the m fragments that are about to coalesce.

Similarly, if fragments that are born or die between frames i and f are again excluded, then the fragments in frame f must also have their fluxes adjusted in one of the following 2 ways:

1. If the fragment a in frame f has not just been involved in fragmentation, then its flux Φ_a^f is adjusted such that

$$\Phi_a^f \rightarrow \frac{\Phi_a^f + \Phi_A^i}{2},$$

where Φ_A^i is its corresponding flux in the frame i . If the fragment a does not consist of newly coalesced fragments, then $\Phi_A^i = \Phi_a^i$, the fragment's flux in frame i . If a is

comprised of newly coalesced fragments, then

$$\Phi_A^i = \sum_{j=1}^p \Phi_{a_j}^i,$$

where the $\Phi_{a_j}^i$ are the fluxes of the p fragments that coalesced.

2. If the fragment a has just coalesced with m fragments, then the fluxes of each of the a_j fragments ($j = 1, \dots, m$) is adjusted such that

$$\Phi_{a_j}^f \rightarrow \frac{\Phi_{a_j}^f}{\Phi_A^f} \left(\frac{\Phi_A^f + \Phi_A^i}{2} \right),$$

where Φ_A^i is defined as above and

$$\Phi_A^f = \sum_{j=1}^m \Phi_{a_j}^f,$$

namely, the sum of the fluxes of the fragments that just coalesced.

The results obtained by these measures are provided in the following subsection.

5.4.1 Coronal Flux Recycling Time Due to Reconnection Driven by Footpoint Motions Alone

By prohibiting the emergence and cancellation of flux between magnetogram pairs, it is possible to measure the changes in domain fluxes resulting from the motions of the fragments alone.

Assuming that each domain is either a “donor” or a “recipient” of reconnected flux, then the total amount of reconnected flux is

$$\Delta R = \frac{1}{2} \sum_{n=1}^{N_d} |R_n|. \quad (5.11)$$

In this scenario, $R_n \equiv \Delta\psi_n$, since $S_n = 0$ in all domains.

The fraction of flux reconnected over time Δt is given by

$$f_R = \frac{\Delta R}{F}, \quad (5.12)$$

where F , the total flux in the system, is given by

$$F \equiv \sum_{n=1}^{N_d} \psi_n = \frac{1}{2} \sum_{a=1}^{N_s} \Phi_a. \quad (5.13)$$

If $f_R \ll 1$, then all field lines will be remapped after a time

$$\tau_r \equiv \frac{\Delta t}{f_R} = \Delta t \frac{\sum_{a=1}^{N_s} |\Phi_a|}{\sum_{n=1}^{N_d} |R_n|}, \quad (5.14)$$

where Δt is the time lapse between successive magnetograms, which here is 15 minutes. In the first instance, where all fragments that have just been born or just died are removed, it is found that an average of $8.12\% \pm 0.14\%$ of flux is recycled between each pair of magnetograms. This results in a recycling time of $\tau_r = 3.08$ hours (ranging from 3.03–3.13 hours) for coronal field lines by motions of their footpoints alone.

By copying fragments that are just born or have just died into the frame in which they are not present, similar figures are obtained. It is found that, on average, $7.88\% \pm 0.14\%$ of flux is remapped between each pair of magnetograms, resulting in a period of $\tau_r = 3.17$ hours for all the coronal field lines to be recycled. This has a range of 3.12–3.23 hours if errors are taken into account.

However, the constant emergence and cancellation of flux through the photosphere is likely to have an effect on the remapping time for coronal field lines. The next section therefore details how an estimate of the effects of emergence and cancellation may be obtained.

5.5 Scenario 2: Including Emergence and Cancellation

In this section, changes in the strengths of the fragments from one frame to the next are included. Therefore, a boxcar smoothing method, as described in Appendix B, is applied to the time sequence of each fragment in order to remove spurious fluctuations in the fragment strengths. The effects of such smoothing are described in Appendix C.

Any effort to take into account emergence and cancellation of flux requires prior knowledge of the changes in source fluxes. In general, the change in the flux of a fragment a from frame i to frame f will be given by

$$\Delta\Phi_a = \Phi_a^f - \Phi_a^i.$$

However, it is again necessary to approximate what happens when fragments split or coalesce. Thus, in such cases, the change in flux of a fragment a is approximated by

$$\Delta\Phi_a = \frac{\Phi_a^f}{\Phi_A^f} (\Phi_A^f - \Phi_A^i).$$

If a is involved in fragmentation, then Φ_A^f is the sum of the fluxes of all the fragments that were involved in the fragmentation. Otherwise, $\Phi_A^f = \Phi_a^f$. Similarly, if a consists of newly coalesced fragments, then Φ_A^i is the sum of the fluxes of all the fragments in frame i that have coalesced by frame f . Otherwise, $\Phi_A^i = \Phi_a^i$, the corresponding flux for a in frame i .

Since infinity is included as a balancing source, then it too will have a change in strength. Thus, as changes from one system of flux balance to another are considered, the difference in these two fields comprises equal amounts of positive and negative flux. Hence, it is now possible to start thinking about obtaining a decomposition of Equation (5.10).

A natural starting point for considering emergence and cancellation is to assume that the processes of emergence and cancellation must occur at the photosphere, resulting in $S_n = 0$ for any domain n which is purely coronal. Assuming intuitively that emergence and cancellation occur through a set of flux tubes crossing the photospheric surface, then each flux tube will correspond to a domain, with the set of flux tubes forming a subset \mathcal{T} of all domains. Henceforth this will be referred to as *pair-wise emergence/cancellation*. In the most straightforward version of this scenario, no source may belong to more than one flux tube, meaning that each flux tube links a pair of sources that must increase or decrease in tandem. However, even if pair-wise emergence/cancellation were occurring in practice, one could not realistically expect that measured changes in source fluxes $\Delta\Phi_a$, with inherent noise and other errors, would be exactly equal in each pair of sources. Thus, in order to make the analysis robust and mathematically well-posed, enough domains must be included in the set \mathcal{T} so that its graph forms a *tree*. A tree is a graph in which all the vertices (here sources) are connected by a number of edges (domains) that is one fewer than the number of vertices, here $N_s - 1$. Consequently, there will be one and only one path connecting any pair of vertices, thus ruling out the possibility of circuits (a circuit is a closed path containing a route that starts and ends at the same vertex, passing through other vertices along the way).

However, a general set of photospheric domains will contain many circuits, meaning that there will be numerous tree subgraphs that span the entire set of sources. Thus,

further information must be supplied so that the choice of tree is unique and is related to emergence and cancellation. An obvious assumption is that emergence/cancellation occurs between the closest pairs of sources, leading to a *minimum spanning tree*. Of course, infinity has been included as a source, which doesn't have a position. However, this minor difficulty is overcome by writing $D_{a\infty}$, the distance between the source a positioned at \mathbf{x}_a and infinity, as

$$D_{a\infty} = D_{max} + \frac{1}{|\mathbf{x}_a - \mathbf{x}_0|},$$

where \mathbf{x}_0 is the centroid of all the sources and D_{max} is the maximum distance between any pair of sources. Thus, sources located at the edge of the region are preferentially chosen as the sources through which infinity is included in the tree.

So, with knowledge of the distances between pairs of sources, the minimum spanning tree is obtained, with the distances between the connected pairs of sources subject to the minimisation. The minimum spanning tree is obtained using Prim's algorithm (Prim, 1957).

The incidence matrix $M_{an}^{(T)}$ may now be introduced, defined such that

$$M_{an}^{(T)} = \begin{cases} M_{an}, & \mathcal{D}_n \in \mathcal{T} \\ 0, & \mathcal{D}_n \notin \mathcal{T} \end{cases}, \quad (5.15)$$

where \mathcal{D}_n represents the domain n . This allows Equation (5.10) to be rewritten as

$$\sum_{n=1}^{N_d} M_{an}^{(T)} S_n = \Delta\Phi_a, \quad (5.16)$$

under the assumption that $S_n = 0$ for $\mathcal{D}_n \notin \mathcal{T}$. Since \mathcal{T} is a tree, the matrix $M_{an}^{(T)}$ is of full rank and may be inverted, giving

$$S_n = \sum_{a=1}^{N_s} [M^{(T)}]_{na}^{-1} \Delta\Phi_a. \quad (5.17)$$

In practice, Equation (5.15) is solved by locating a "leaf" on the tree, which is a vertex, representing source y , say, connected to only one edge, representing domain \mathcal{D}_x , say. This gives the relationship $S_x = |\Delta\Phi_y|$, which is trivial to solve. The vertex corresponding to source y and the edge corresponding to domain \mathcal{D}_x are then "removed" from the graph, and the flux of the source z at the other end of domain x is decremented, such that $\Delta\Phi_z \rightarrow$

$\Delta\Phi_z - S_x$. Hence, row a and column n are removed from Equation (5.15). The new graph still has one fewer edges than vertices, and is therefore still a tree. The process is repeated, solving for the next leaf and so forth, until all the S_n have been found. The final equation will contain two sources coupled by a single domain, and as such will be mathematically over-specified. However, since the system is in over-all flux balance, both of the remaining fluxes will be equal, and the remaining S_n may be determined from either one.

If \mathcal{T} is unconnected, then, since complete flux balance is far from guaranteed for each disconnected component, Equation (5.15) would be over-constrained and could not be solved in general. Therefore, after obtaining the tree \mathcal{T} , a quick check is performed to ensure that the graph \mathcal{T} is connected, which, of course, it always is.

In pair-wise emergence, at least in optimal conditions, the $\Delta\Phi_a$ vector takes the form of equal pairs corresponding to the emerging flux tubes. It can be shown that in this scenario S_n is non-zero in only those domains linking the pairs being considered, independent of which domains supplemented the graph \mathcal{T} in order to obtain a tree. In practice, the addition of errors to a set of pair-wise emergences/cancellations will be manifested in non-zero (but presumably small) fluxes in additional domains.

5.5.1 Photospheric Recycling Times

By considering the change in the source fluxes, an estimate for the recycling time of photospheric flux due to emergence and cancellation may be obtained. The amount of emergence in all the sources is given by

$$\Delta S_+ = \frac{1}{2} \sum_{a=1}^{N_s} |\Delta\Phi_a| \Theta(\Delta\Phi_a), \quad (5.18)$$

where the Heaviside function $\Theta(x)$ picks out only the cases where the flux is increasing as emergence. The factor of $1/2$ is present since emergence affects a positive and a negative pole equally. Conversely, the amount of cancellation is given by

$$\Delta S_- = \frac{1}{2} \sum_{a=1}^{N_s} |\Delta\Phi_a| \Theta(-\Delta\Phi_a). \quad (5.19)$$

In a statistical steady state, one may define an average quantity ΔS that accounts for either emergence or cancellation as

$$\Delta S \simeq \frac{1}{2}(\Delta S_+ + \Delta S_-) \equiv \frac{1}{4} \sum_{a=1}^{N_s} |\Delta \Phi_a|. \quad (5.20)$$

The fraction of flux that emerges, which by the assumption of a statistical steady state is equal to the amount that cancels, is

$$f_S \equiv \frac{\Delta S}{F}, \quad (5.21)$$

where F is the total flux in the system, as given by Equation (5.13). Provided that $f_S \ll 1$ and the system is indeed in a statistical steady state, then all photospheric flux will be “recycled” by emergence or cancellation after a time

$$\tau_p \equiv \frac{\Delta t}{f_S} = \Delta t \frac{\sum_{a=1}^{N_s} |\Phi_a|}{\frac{1}{2} \sum_{a=1}^{N_s} |\Delta \Phi_a|}. \quad (5.22)$$

By including all changes in source fluxes in the calculation (i.e. changes due to births of fragments, deaths of fragments and fluctuations in their fluxes throughout their lifetimes), a photospheric flux recycling time of 15.66 hours is obtained. This figure is in fairly good agreement with that of Hagenaar (2001) who obtained a slightly shorter recycling time of 14 hours for photospheric flux. Important factors that account for the difference in these estimates include the size of the area being studied—the region studied here is significantly smaller than that studied by Hagenaar (2001), plus the data set used here is of a much higher resolution too. Also, the two methods of calculating the recycling time differ greatly, with Hagenaar (2001) generally being much stricter in what is accepted as an emergence. (Hagenaar et al. (2003) revised the previous figure by Hagenaar (2001) of 14 hours to 8–19 hours, which is still in agreement with the estimate obtained here).

5.5.2 Coronal Recycling Time Due to Emergence and Cancellation

An estimate for the time taken to recycle the coronal field due to emergence and cancellation may also be obtained by considering the domains with $S_n \neq 0$. The total amount of emergence/cancellation in all domains is given by

$$\Delta S'_\pm \equiv \sum_{r=1}^{N_d} |S_n| \Theta(\pm S_n). \quad (5.23)$$

Again, the Heaviside function picks out cases where flux is increasing/decreasing as emergence/cancellation. Following the same reasoning for ΔS_{\pm} , an average quantity to account for *either* emergence or cancellation is defined:

$$\Delta S' \equiv \frac{1}{2}(\Delta S'_+ + \Delta S'_-) = \frac{1}{2} \sum_{n=1}^{N_d} |S_n|. \quad (5.24)$$

Using $\Delta S'$ instead of ΔS provides a time for *coronal flux recycling* due to emergence and cancellation:

$$\tau_{e/c} \equiv \Delta t \frac{F}{\Delta S'} = \Delta t \frac{\sum_{a=1}^{N_s} |\Phi_a|}{\sum_{n=1}^{N_d} |S_n|}. \quad (5.25)$$

The photospheric recycling time should be longer than the corresponding coronal recycling time for recycling due to emergence/cancellation. This can be seen by taking the absolute value of Equation (5.16) and applying the triangle inequality:

$$|\Delta \Phi_a| \leq \sum_{n=1}^{N_d} M_{an}^{(T)} |S_n|. \quad (5.26)$$

The equality only holds in the case that no source is involved in both emergence and cancellation simultaneously (since in this case all of the terms $M_{an}^{(T)} S_n$ are of the same sign for a given source a). Although this is automatically true in the pair-wise emergence scenario, when each source is part of only one emerging flux tube, in the more general case of a tree of emergence domains it is possible for one source to simultaneously connect to both emerging and cancelling domains at the same time. Substituting the inequality in expression (5.20) yields

$$\Delta S \leq \frac{1}{4} \sum_{a=1}^{N_s} \left(\sum_{n=1}^{N_d} M_{an}^{(T)} \right) |S_n| = \Delta S'. \quad (5.27)$$

Here use has been made of the fact that $\sum_a M_{an} = 2$ for any incidence matrix, since each domain connects exactly two sources. This inequality leads immediately to $\tau_{e/c} \leq \tau_p$.

At this point, it is not possible to obtain a value of the coronal recycling time due to emergence and cancellation that includes effects of the births and deaths of fragments. Since a birth (death) can inject (remove) a relatively large amount of flux in one go (due to the low cadence of the sequence of magnetograms studied here), this would wreak havoc on the decomposition for S_n . Such a problem would not be so pronounced with

a much higher cadence, since the births (deaths) of fragments would be more smoothly traced, and there wouldn't be such a large amount of flux simply appearing (disappearing) between frames. Nevertheless, by including only the fluctuations in fragment fluxes throughout their lifetimes, coronal recycling times of $\tau_{e/c} = 2.25$ hours and $\tau_{e/c} = 2.29$ hours are found (the first figure is obtained by copying newly born/just died fragments into the frame in which they are not present; the second figure is obtained by removing said fragments from both frames altogether). The corresponding photospheric times, calculated by prohibiting births and deaths of fragments, are $\tau_p = 20.84$ hours and $\tau_p = 21.01$ hours. Thus, the time taken to recycle all the coronal flux due to emergence and cancellation is much less than the time taken to recycle all photospheric flux. This, as will be seen, has dramatic consequences for the time taken for all coronal field lines to be remapped by reconnection.

5.5.3 Coronal Recycling Time Due to Reconnection Driven by Emergence, Cancellation and Motions of Fragments

Having obtained an estimate for the amount of flux in each domain that may be attributed to emergence and cancellation, it is now possible to consider reconnection.

Changes in domain fluxes related to reconnection are given by subtracting the flux due to emergence/cancellation from each domain:

$$R_n = \Delta\psi_n - \sum_{a=1}^{N_s} [M^{(T)}]_{na}^{-1} \Delta\Phi_a. \quad (5.28)$$

An estimate of the amount of the coronal flux that is involved in magnetic reconnection may be obtained from

$$\tau_r \equiv \Delta t \frac{F}{\Delta R}, \quad (5.29)$$

where ΔR is found by substituting the R_n found here into Equation (5.11). In doing so, it is found that $17.87\% \pm 0.21\%$ of coronal flux is remapped every 15 minutes, giving a recycling time of 1.399 hours (ranging from 1.382–1.416 hours). These figures are obtained by copying newly born/just died fragments into the frame in which they are not present; when the newly born/just died fragments are removed from the frame in which they are present, it is found that $17.61\% \pm 0.21\%$ of coronal flux is remapped every 15 minutes, giving a recycling time of 1.420 hours (ranging from 1.403–1.437 hours).

The calculation of the flux (S_n) that has emerged or cancelled in a given domain n linking a pair of sources is often larger than the observed net change in flux ($\Delta\psi_n$) when $\Delta\psi_n > 0$, so that the reconnected flux (R_n) is of the opposite sign to S_n (similarly, for $\Delta\psi_n < 0$, it is sometimes found that $S_n < \Delta\psi_n$). This implies that the field, initially assumed potential, reacts to emergence and cancellation of flux between frames by re-arranging itself through the process of reconnection to a new equilibrium field (which is assumed to be potential). This is reasonable, since it would be unlikely that coronal domains simply swell from injection of flux without reconnection occurring. Thus, the changing of photospheric flux continuously drives reconnection in the corona, enabling the field to remain close to potential.

5.6 Energy Dissipation

In this section, energy dissipation by means of separator reconnection is considered.

Generally, a given domain will be encircled by a closed ring of separators (Lau and Finn, 1990; Longcope and Klapper, 2002; see also Chapter 3). The flux ψ_n^i in such a domain n may be obtained by defining a closed curve \mathcal{K} which, for a coronal domain, is just the engirdling ring of separators, whilst for a photospheric domain, \mathcal{K} is the section of the engirdling curve that is situated in the region $z \geq 0$, running from the photospheric points P to Q , combined with a line segment in the $z = 0$ plane joining P to Q . Integrating the magnetic potential \mathbf{A} along \mathcal{K} gives

$$\psi_n^i = \oint_{\mathcal{K}} \mathbf{A} \cdot d\mathbf{l}, \quad (5.30)$$

where the direction of the integration proceeds parallel to the magnetic field along the separator.

Of course, there will also be isolated systems of flux where the field from a given source is completely enclosed by an unbroken fan surface from a single null— it was shown in Chapter 4 that around 12.5% of nulls give rise to such domains in a region like the one studied here. However, these domains account for only a small fraction of the total number of domains and, due to their nature, their fluxes will be altered primarily through emergence/cancellation of flux through the photospheric boundary. Thus, the consequences of the presence of these types of domain will not be considered here.

If the photospheric fragments are displaced so that the domain flux changes from ψ_n^i

to ψ_n^f , then this will typically alter the net vacuum flux that \mathcal{K} encloses by an amount $\Delta\psi_n$. However, Longcope (1996) points out that if the plasma is a perfect conductor, it will not permit any change in flux through \mathcal{K} . Therefore, a current ribbon with a total current I forms along the separator, with I flowing such that it generates a self-flux $\psi_n^{(cr)}(I)$ which cancels $\Delta\psi_n$. Hence

$$\psi_n^f + \psi_n^{(cr)}(I) = \psi_n^i + \Delta\psi_n + \psi_n^{(cr)}(I) = \psi_n^i. \quad (5.31)$$

Longcope and Cowley (1996) found that the quantities $\psi_n^{(cr)}(I)$ and I are related by

$$\psi_n^{(cr)}(I) = \mu_0 I \mathcal{L}, \quad (5.32)$$

where \mathcal{L} is the differential inductance of the current ribbon. The precise expression for \mathcal{L} can be quite complex, depending upon the current it carries; however, it may be crudely thought of as being the length of the separator, L .

In order that non-potential energy may be stored in the corona, this requires that current densities are present without an accompanying electric field. Longcope (1996) proposed a scenario where the corona remains ideal for a period, during which currents gradually build up along each separator loop. When the build-up of current along a given loop exceeds a threshold value, it is assumed that some instability occurs, which permits an electric field E_{\parallel} that in turn allows a change in flux through the loop \mathcal{K} , and reduces $\psi_n^{(cr)}$. Longcope (1996) also assumed that, when this process occurs, $\psi_n^{(cr)} \rightarrow 0$, so that all the energy above that of the potential energy is liberated and the field is returned to its vacuum state.

Here the aim is to obtain an estimate for the mean threshold current, I^* , at which the reconnection process is triggered. Time differentiating equation (5.30) results in a version of Faraday's law

$$\frac{d\psi_n}{dt} = \oint_{\mathcal{K}} \frac{\partial \mathbf{A}}{\partial t} \cdot d\mathbf{l} = - \int E_{\parallel} dl = V_n, \quad (5.33)$$

where V_n is the voltage along the loop \mathcal{K} . Here the approximation

$$\frac{\Delta R_n}{\Delta t} \approx \frac{d\psi_n}{dt} \quad (5.34)$$

is made, where ΔR_n is the amount of reconnection associated with the domain n . Withbroe and Noyes (1977) obtained a heating rate of $H = 300 \text{ W/m}^2$ for the quiet Sun. This

may be related to this study by

$$H = \frac{I^* \langle V_n \rangle_{sep}}{A} = \frac{I^*}{A} \left\langle \frac{\Delta R_n}{\Delta t} \right\rangle_{sep} N_{sep}, \quad (5.35)$$

where A is the area of the region, $\langle V_n \rangle_{sep}$ is the mean voltage, I^* is the mean current along each separator, and N_{sep} is the number of separators in the region. Using the figures obtained by prohibiting emergence/cancellation, an I^* of 5.33×10^{10} Amps is obtained by removing all fragments that have just been born or died, and a similar figure of $I^* = 5.45 \times 10^{10}$ Amps is found by copying the newly born/just died fragments into the frame in which they are not present.

However, in the example where emergence and cancellation during the lifetimes of fragments are allowed, much lower values of I^* are found. By using ΔR in order to obtain $\langle V_n \rangle_{sep}$, a value of 2.42×10^{10} Amps is found in the scenario whereby fragments that are newly born/just died are copied into the frame in which they are not present (by removing newly born/just died fragments from the frame in which they are present, a similar figure of 2.44×10^{10} Amps is found).

These values make sense when the difference in recycling times for the two representations (i.e. including and excluding emergence and cancellation) are considered. By disallowing emergence and cancellation, it is found that much less reconnection takes place. Thus, one should naturally expect larger currents to build up. In the case when emergence and cancellation are allowed, however, the abundance of reconnection events means that the threshold current for allowing reconnection and the subsequent dissipation of energy must be lower for the given heating rate.

The figures above provide an indication as to the sort of values that should be expected from current-ribbon models of the quiet Sun, where currents are confined to magnetic separators.

Longcope (1998), in contrast, applied a current ribbon model to the flare of 7 January 1992, and suggested maximum currents of the order 10^{11} Amps were flowing along the associated separators. Here, the estimates for quiet-Sun separators suggest figures between 1–10 times smaller.

5.7 Conclusions

Examining changes in the connectivity of potential fields based on observed magnetograms has shown that there is quite a gulf in the recycling time of coronal flux compared with that for photospheric flux.

By identifying discrete fragments in a 12-hour sequence of magnetograms, it is found that the time taken for all photospheric flux to be recycled is around 15.7 hours. This is in fairly good agreement with the figures of 14 hours obtained by Hagenaar (2001) and 8–19 hours obtained by Hagenaar et al. (2003), considering the relatively small region and small time interval used here, not to mention the completely different approaches to the calculations.

Whilst the recycling time for photospheric flux has been known for several years, until now there have been no estimates for the time taken to recycle the magnetic field in the corona. Such a calculation has been presented here. By considering a *pair-wise emergence/cancellation* scenario, whereby flux emerges/cancels in flux tubes through a tree of domains linking pairs of closest photospheric flux sources, it is estimated how much of the change in domain fluxes is a consequence of emergence and cancellation of flux in the photosphere. In this way, it is found that emergence and cancellation of photospheric flux will recycle all coronal field lines in around 2.3 hours.

The time taken to recycle the coronal field due to reconnection, which is of particular interest since reconnection is believed to be the primary means of heating the corona over the quiet Sun, has also been calculated here. By considering two scenarios, one in which the processes of emergence and cancellation are prohibited, and another in which the change in magnetic flux domains due to emergence and cancellation is estimated, it is found that the coronal flux is reconnected more quickly in the presence of emergence and cancellation. If the motions of magnetic flux fragments were the only mechanism driving reconnection in the corona, it is surmised the process would take around 3 hours to completely remap all coronal field lines. However, by allowing emergence and cancellation as well, a much lower estimate of around 1.4 hours is found.

This implies that the two main driving forces behind reconnection in the corona, namely reconnection driven by motions of fragments and reconnection driven by emergence and cancellation of flux, are comparable in their importance. The first estimate of 3 hours indicates that even if emergence and reconnection were not occurring, the coronal magnetic field would still be entirely replaced in a relatively short time interval. The second estimate of 1.4 hours implies that reconnection continually occurs in reaction to

the emergence and cancellation of flux in the photosphere, which seems reasonable, as the coronal field is unlikely to allow domains to swell too much from injection of flux without responding in some way (similarly with reduction of flux due to cancellation). Hence, the changing of photospheric flux continually drives reconnection in the corona, enabling the field to remain close to potential.

All this will naturally have consequences for coronal heating. In this study, observed heating rates have been used, along with the findings presented here, to predict the consequences for energy dissipation due to separator reconnection. It is shown that the observed changes in domain fluxes will result in an average current density of around 5×10^{10} Amps for reconnection due to motions of flux fragments alone, whereas if reconnection due to emergence and cancellation is included, a lower average current is produced of around 2×10^{10} Amps. This points to the fact that a higher rate of reconnection implies that the currents flowing along the separators during reconnection will generally be lower, as expected.

The model presented here does, however, have its limitations. Flux motions, caused by granular flows, which are unobservable in current magnetograms and occur within fragments (which have a finite geometrical extent), are neglected here. These would in turn cause more reconnection of field lines within domains, and would hence reduce the recycling time further. To some degree, however, the effects of neglecting such dynamics in the model are offset by the fact that potential fields are used to model the corona, since a potential field permits no stress and therefore reconnection occurs instantaneously. Work by Parnell and Galsgaard (2003), which examined reconnection between two driven flux patches initially separated and connected to an ambient coronal field, showed that in a potential field, the sources reconnect all their flux in a quarter of the time taken by a full MHD evolution.

The mean reconnection time for coronal flux presented here will nevertheless have a number of interesting applications in future. Indeed, the analysis may be extended to provide a distribution of energy release magnitudes for the solar corona, and it could also be adapted to show how reconnection in the quiet Sun may account for the background population of non-thermal electrons observed by RHESSI. Furthermore, the frequent reconnection episodes will most likely launch a spectrum of waves that are a necessary input to models of solar wind acceleration (e.g. Axford and McKenzie, 2002). Knowledge of the recycling rate of the coronal magnetic field may also be of relevance to studies of the anomalous diffusion of plasma through the corona and abundance variations.

Chapter 6

Coronal Tectonics Model

正岡 子規	水	橋	夏	The summer river
	を	あ	川	Although there is a bridge
	行	れ	や	
く	と		My horse goes through the water	
	馬			

MASAOKA SHIKI (1867–1902)

6.1 Introduction

Several different heating mechanisms are believed to be at work in the various magnetic phenomena observed in the Sun's outer atmosphere, the solar corona. In the quiet Sun, for instance, the complicated motions of network and intranetwork elements in the photosphere will force coronal magnetic fields, with their footpoints rooted in these concentrations, to respond in different ways.

Heating mechanisms tend to fall broadly into one of two categories, namely heating due to magnetic waves and heating due to magnetic reconnection. Granulation, for example, is likely to result in heating by way of magnetic waves, as granular motions will tend to buffet magnetic fragments, resulting in magnetic waves being generated that propagate up to the corona and dissipate their energy there (Roberts, 1991). An example of an instance where reconnection is important is the process of emergence of flux elements through the photospheric surface, where the emerging magnetic field reconnects with the overlying field, as discussed in Chapter 5. In a similar manner, cancellation between collections of flux elements will also result in reconnection. This process has been used to explain the presence of X-ray bright points in particular (Parnell and Priest, 1995).

As has already been discussed, motions of magnetic flux fragments in the solar photosphere will undoubtedly drive currents in the corona above, which in turn may lead to coronal heating. Up until this point, only currents concentrated along separator field lines have been discussed; however, one might also expect a certain amount of current to build up on the separatrix surfaces that bound the complex domain structures that fill the Sun's outer atmosphere. Priest et al. (2002) recently proposed a scenario whereby reconnection is driven at the myriads of separatrix surfaces that separate regions of interconnectivity, known as "flux-tube tectonics", by analogy with geophysical plate tectonics on Earth. They showed that lateral shearing motions of sources lead directly to the formation of current sheets along separatrices, which then dissipate rapidly by fast reconnection or in a turbulent manner.

Whilst high-resolution images from *SOHO* have revealed that small magnetic fragments in the quiet Sun have typical fluxes of the order 10^{18} Mx, the likelihood is that the fundamental units of flux in the quiet-Sun photosphere are a great deal smaller, comprising flux tubes with a field strength of around 1200 G, diameter 100 km and a flux of around 3×10^{17} Mx (Priest et al., 2002). This would imply that each network element itself consists of around 10 of these intense flux tubes, whilst ephemeral regions may contain as many as 100. This will have important consequences for the field above the photosphere, due to the multitude of unobserved flux tubes separated from one another by a great many separatrix surfaces.

Here the aim is to model in $2\frac{1}{2}$ D the effect of photospheric flux dislocation on coronal heating by adopting a standard model for $2\frac{1}{2}$ D magnetic fields used, for example, by Zwingmann et al. (1985), Wolfson and Low (1988), Amari and Aly (1990), Vekstein et al. (1990), Vekstein and Priest (1992, 1993) and Titov and Priest (1993). (Here $2\frac{1}{2}$ D here refers to fields with no spatial dependence on the z -direction.) This is achieved by showing that the independent motions of separate small 2D flux elements in the photosphere generate current concentrations at the separatrix curves in the corona, where this flux becomes more continuously distributed. The effects of complexity are examined by investigating what happens to the amount of free energy (i.e. that above potential) resulting from a small shear when the total absolute flux in a region is fixed and the number of concentrations by which it pierces through the photospheric surface is varied. The next section, Section 6.2, introduces the problem and provides an overview of two-dimensional fields. Section 6.3 then considers small perturbations to an initial potential field configuration, with Section 6.4 providing a calculation of the extra energy stored by this process. A simple four-source example is studied in Section 6.5, whilst Section 6.6 discusses the effects of varying levels of complexity on the energy stored. Section 6.7

provides a simple comparison between separator heating and separatrix heating by revisiting the quadrupolar configuration of Section 6.5. A concluding discussion is then given in Section 6.8.

6.2 Flux Tube Tectonics

Priest et al. (2002) considered a plane-stratified geometry with the photosphere represented by the planes $z = -L$ and $z = L$. By studying a configuration in which the field emanates from two infinite arrays of uniformly spaced flux sources of equal magnitude, they found that in 2.5D the shearing of fragmented flux elements generates concentrated flux layers which, although not singular in the Dirac sense, are nevertheless concentrated into extremely thin layers in the limit of large aspect ratios. In 3D, they found that the shearing motions give rise to a discontinuity in the field across separatrices that supports a singular current sheet across which the current density exhibits a Dirac distribution. In both cases, they showed that no significant current flows outwith these sheets.

The work here is also carried out in Cartesian coordinates (x, y, z) , assuming a locally flat photosphere in the plane $y = 0$. The magnetic field at the photosphere is assumed to be rooted in sources of negligible size that suffer relative motions with respect to each other, driven by the photospheric flow. Initially, the coronal field is taken to be the potential field associated with these line sources.

Only simple motions are considered, in which the field sources are moved slightly by a shearing in the z -direction. The resulting coronal magnetic perturbation is calculated under the assumption that it can be treated by linearisation about the potential field, and that the coronal magnetic structure remains at all times force-free.

6.2.1 Overview of 2D Magnetic Fields

Following Zwingmann et al. (1985), Wolfson and Low (1988), Amari and Aly (1990), Vekstein et al. (1990) and others, consider a 2^{1/2}D field $\mathbf{B}(x, y)$:

$$\mathbf{B} = B_x \hat{x} + B_y \hat{y} + B_z \hat{z}, \quad (6.1)$$

which is translationally symmetric in the z -direction. Denoting B_z by b , and noting that \mathbf{B}_\perp , the part of \mathbf{B} which is perpendicular to the direction of invariance z , is itself

solenoidal ($\nabla \cdot \mathbf{B}_\perp = 0$), one may write

$$\frac{\partial B_x}{\partial x} + \frac{\partial B_y}{\partial y} = 0. \quad (6.2)$$

This implies that $\mathbf{B}_\perp = \nabla \times (a(x, y)\hat{\mathbf{z}})$, which gives $B_x = \partial a / \partial y$ and $B_y = -\partial a / \partial x$. Thus, \mathbf{B} may be expressed in terms of two functions, $a(x, y)$ and $b(x, y)$, as

$$\mathbf{B} = \frac{\partial a}{\partial y} \hat{\mathbf{x}} - \frac{\partial a}{\partial x} \hat{\mathbf{y}} + b \hat{\mathbf{z}}. \quad (6.3)$$

It is worth noting here that

$$\mathbf{B} \cdot \nabla a = B_x \frac{\partial a}{\partial x} + B_y \frac{\partial a}{\partial y} = 0. \quad (6.4)$$

This implies that $a(x, y)$ is constant along every field line. Much use will be made of this property throughout the subsequent analysis. Using Ampere's law, the electric current conveyed in a magnetic structure is given by

$$\nabla \times \mathbf{B} = \mu_0 \mathbf{j}, \quad (6.5)$$

where μ_0 is the vacuum permeability. The displacement current, $\epsilon_0 \partial \mathbf{E} / \partial t$, has been ignored as always in non-relativistic MHD. Evaluating Equation (6.5) explicitly for the field here gives

$$\mu_0 \mathbf{j} = \frac{\partial b}{\partial y} \hat{\mathbf{x}} - \frac{\partial b}{\partial x} \hat{\mathbf{y}} - \left(\frac{\partial^2 a}{\partial x^2} + \frac{\partial^2 a}{\partial y^2} \right) \hat{\mathbf{z}}. \quad (6.6)$$

Furthermore, the Lorentz force (or rather its density) is

$$\mathbf{j} \times \mathbf{B} = \frac{1}{\mu_0} \left[- \left(\Delta a \frac{\partial a}{\partial x} + b \frac{\partial b}{\partial x} \right), - \left(\Delta a \frac{\partial a}{\partial y} + b \frac{\partial b}{\partial y} \right), \left(\frac{\partial b}{\partial x} \frac{\partial a}{\partial y} - \frac{\partial b}{\partial y} \frac{\partial a}{\partial x} \right) \right]. \quad (6.7)$$

6.2.2 Non-Constant- α Force-Free Fields

Here, a force-free field is considered, such that any ambient force, pressure gradient or gravity is negligible in comparison to the Lorentz force, and so $\mathbf{j} \times \mathbf{B} = 0$. In particular,

$$\frac{\partial b}{\partial x} \frac{\partial a}{\partial y} - \frac{\partial b}{\partial y} \frac{\partial a}{\partial x} = 0. \quad (6.8)$$

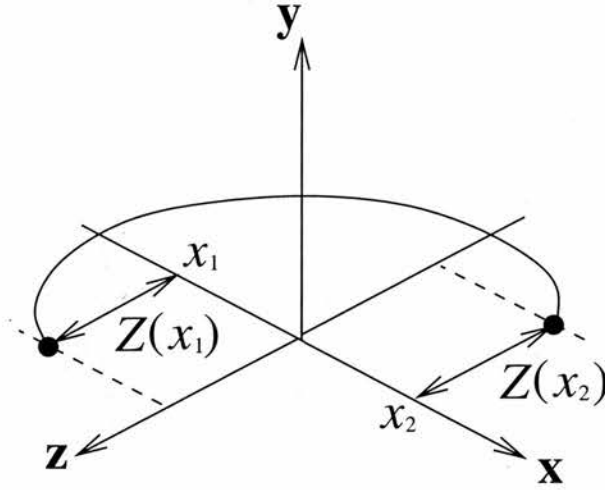


Figure 6.1: Schematic representation of the photospheric displacement ($Z(x)$) of the footpoints of a $2^{1/2}$ D force-free magnetic field. Initially, the field is potential and the field line lies in the x - y plane with $Z(x_1) = Z(x_2) \equiv 0$.

This implies that $b(x, y)$ is in fact a function, $b(a)$, of $a(x, y)$, and this in turn implies that b is constant along any given field line. The consequence is that the first two equations of Equation (6.7) reduce to a single equation, since

$$\left. \begin{aligned} \frac{\partial b}{\partial x} &= \frac{db}{da} \frac{\partial a}{\partial x} \\ \frac{\partial b}{\partial y} &= \frac{db}{da} \frac{\partial a}{\partial y} \end{aligned} \right\} \Rightarrow \nabla b = \frac{db}{da} \nabla a. \quad (6.9)$$

Thus

$$-\Delta a \nabla a - b \frac{db}{da} \nabla a = 0, \quad (6.10)$$

which shows that the force-balance equation can only be satisfied everywhere if the Grad-Shafranoff equation is satisfied, i.e.

$$\Delta a + b \frac{db}{da} = 0. \quad (6.11)$$

Note that, although there is no need to introduce α here, it equals db/da , and so is a function of a alone.

6.3 Perturbation of 2D Potential Field into a $2\frac{1}{2}$ D Force-Free Field

Now suppose that this configuration is sheared by slightly moving the footpoints of any field line rooted at x in the plane $y = 0$ by $\mathbf{Z} = Z(x)\hat{\mathbf{z}}$. From the flux freezing theorem, $B_y(x, 0)$ is unchanged, as is $a(x, y)$, which remains equal to $a(x, 0)$. However, the flux freezing theorem also implies that those points which were linked by a common field line before the footpoint displacements should remain so afterwards. For example, suppose a particular field line had its footpoints initially at $(x_1, 0, z_0)$ and $(x_2, 0, z_0)$, with $z_0 = 0$, say. The field line's footpoint at x_1 moves from $z_0 = 0$ to $z_1 = Z(x_1)$, and its footpoint at x_2 moves from $z_0 = 0$ to $z_2 = Z(x_2)$, as sketched in Figure 6.1. The overall footpoint displacement is

$$Z_{12} = Z(x_2) - Z(x_1). \quad (6.12)$$

The component $b(a)$ is determined by the stretching experienced by the corresponding field line. The general field-line equation reduces in this linear approximation to

$$\frac{dx}{B_{0x}} = \frac{dy}{B_{0y}} = \frac{dz}{b(a)} = \frac{ds_0}{|\mathbf{B}_0|} = \frac{ds_0}{|\nabla a|}, \quad (6.13)$$

where ds_0 denotes the line element along an unperturbed field line of the flux function $a(x, y)$. Integrating along a field line gives

$$Z_{12} \equiv Z(x_2) - Z(x_1) = \int_{\text{foot1}}^{\text{foot2}} b \frac{ds_0}{|\nabla a|} = b(a) \int_{a=\text{const.}} \frac{ds_0}{|\nabla a|}, \quad (6.14)$$

since on a line of constant $a(x, y)$, $b = b(a)$ is also constant. The force-free field which appears as a result of the stretching is given by the Grad-Shafranoff equation (6.11).

6.3.1 Infinitesimal Perturbations by Shearing Footpoints of a Potential Field

In cases when $Z_{12}(a)$ is very small, the Grad-Shafranoff equation reduces, to first order in Z_{12} , to $\Delta a = 0$. This implies that the boundary conditions for $a(x, y)$ (i.e. $a(x, 0)$) are effectively unchanged. Hence, $a(x, y)$ remains the same function as it is for the potential

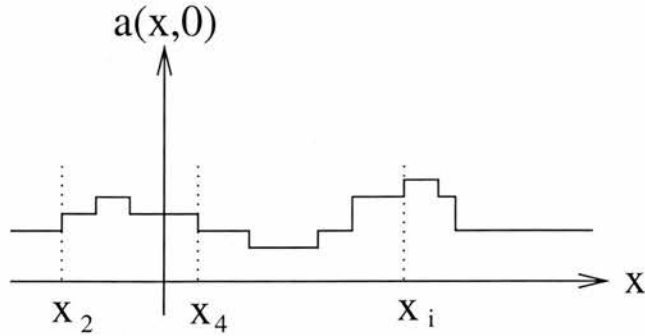


Figure 6.2: Sketch of how $a(x,0)$ varies with x . Between pairs of sources, $a(x,0)$ is constant, and suffers a discontinuous jump when passing over a source.

field. For small $Z_{12}(a)$, the associated $b(a)$ is approximately

$$b(a) \approx \frac{Z_{12}(a)}{\int_{a_0(x,y)=a} \frac{ds_{\perp 0}}{|\nabla a_0|}} = \frac{Z_{12}(a)}{V_0(a)}. \quad (6.15)$$

This relation between the field and the elongation involves the specific volume of the field line

$$V_0 = \int_{a_0(x,y)=a} \frac{ds_{\perp 0}}{|\nabla a_0|}, \quad (6.16)$$

so-named because the volume of a flux tube of small flux $d\Phi$ constructed about this field line is $V_0 d\Phi$. The distribution in space of the electric current induced by the small source displacement is given by

$$\mathbf{j} = \frac{b'(a)\mathbf{B}_{\perp}}{\mu_0}. \quad (6.17)$$

6.3.2 Peculiarities of Fragmented-Flux Model

In the model considered here, the distribution of flux on the photosphere (the plane $y = 0$) enters the system via line sources parallel to the axis of invariance z . The potential field generated by a series of n such sources is given by the sum

$$\mathbf{B}_{\perp}(x, y) = \sum_i^n \frac{\epsilon_i}{\pi} \frac{\mathbf{r}_{\perp} - \mathbf{r}_i}{|\mathbf{r}_{\perp} - \mathbf{r}_i|^2}, \quad (6.18)$$

where $\mathbf{r}_i = x_i \hat{\mathbf{x}} + y_i \hat{\mathbf{y}}$ is the position of the i th source, with strength ϵ_i .

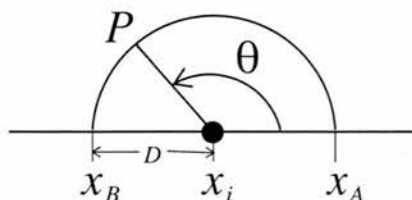


Figure 6.3: Illustration of a point P lying at an angle θ on a semicircle of radius D ($D \ll \delta$, the mean source separation), drawn about a source positioned at x_i . At such a small distance from the source, the value of $a(x, y)$ varies linearly about the circumference of the circle from $a(x_A, 0)$ at the point $(x_A, 0)$ to $a(x_B, 0)$ at the point $(x_B, 0)$.

Since in this model the flux remains constant between magnetic fragments, the function $a(x, 0)$ is constant between the fragments and suffers a discontinuous jump by $-\epsilon_i$ when crossing a fragment i at \mathbf{r}_i , as illustrated in Figure 6.2. When $\sum \epsilon_i = 0$, one should expect that $a(+\infty, 0) = a(-\infty, 0)$. Rotating about a source makes the identification of a easy, because very close to a source its own field is dominant, and \mathbf{B} may therefore be approximated by only the field created by this source, so that

$$\mathbf{B} \approx \frac{\epsilon_i}{\pi} \frac{\mathbf{r}_\perp - \mathbf{r}_i}{|\mathbf{r}_\perp - \mathbf{r}_i|^2} \quad (6.19)$$

near source i , say. If a semicircle of radius D is taken about the source (shown in Figure 6.3), and the value of $a(x_i, 0)$ at x_i is known, then at P , $a(x, y)$ has the value

$$a(P) = a(x_i) + \frac{\epsilon_i}{\pi} \theta(P). \quad (6.20)$$

This is only true if D is very small, so that field lines about the source i are still straight and radial at such a distance.

6.4 Extra Energy Stored

In response to the small motions, the magnetic field perturbations take the form $\mathbf{B}_1 = \nabla \mathbf{A}_1 \times \hat{\mathbf{z}} + \mathbf{b}\hat{\mathbf{z}}$. The poloidal field component is small in comparison to the toroidal component. The magnetic energy (per unit length in the z direction) is then given by

$$W = \int \int \frac{B^2}{2\mu_0} dx dy = \int \int \frac{(B_0^2 + 2\nabla A_0 \cdot \nabla A_1 + b^2)}{2\mu_0} dx dy. \quad (6.21)$$

Under the assumption that the poloidal field remains unchanged for small motions, the perturbation \mathbf{b} to the original field is essentially confined to the direction of invariance

(i.e. $\mathbf{b} = b\hat{z}$). The magnetic energy (per unit length in the z -direction) is then given by

$$W = \int \int \frac{B^2}{2\mu_0} dx dy \equiv \int \int \frac{(B_0^2 + 2\mathbf{B}_0 \cdot \mathbf{b} + b^2)}{2\mu_0} dx dy = \int \int \frac{(B_0^2 + b^2)}{2\mu_0} dx dy. \quad (6.22)$$

Although it may be shown that the energy associated with the actual perturbation to the poloidal field may potentially be comparable to the energy associated with the perturbation to the field in the z -direction in magnitude (and indeed, need not necessarily be positive), such a possibility is not considered here. The change in magnetic energy (per unit length in the z -direction) is consequently given by

$$W_z = \int \int \frac{b^2}{2\mu_0} dx dy. \quad (6.23)$$

Not all this energy is convertible into heat (Heyvaerts and Priest, 1984), but this will nevertheless be assumed in order to judge the properties of energy storage due to shearing. The surface element (dx, dy) is split as usual into $dx dy \equiv dS = ds d\sigma_\perp$, where ds is a line element along the local potential field line and $d\sigma_\perp$ is an infinitesimal element across it. The element $d\sigma_\perp$ sustains a flux $|da|$, the two quantities being related by $|da| = |\mathbf{B}_\perp| d\sigma_\perp$. Since b depends only on a , this gives the stored energy W_z as

$$W_z = \int \int \frac{ds |da|}{|\mathbf{B}_\perp|} \frac{b^2}{2\mu_0} = \int da \frac{b^2(a) V_0(a)}{2\mu_0}. \quad (6.24)$$

In practice, this integral is approximated numerically by

$$W_z = \sum_{i,j} \frac{Z_{ij}^2}{2\mu_0} \int_{a_{min}}^{a_{max}} \frac{da}{V_0(a)}. \quad (6.25)$$

The integral can be calculated without difficulty because $V_0^{-1}(a)$ is a regular function which vanishes at the separatrix. Very interestingly, this shows that those field lines in a given domain linking two sources that contribute most to the energy storage are the lines of smallest specific volume. It will certainly emerge that much energy becomes stored in the ‘carpet’, i.e. regions where a lot of flux closes back down in the form of short loops.

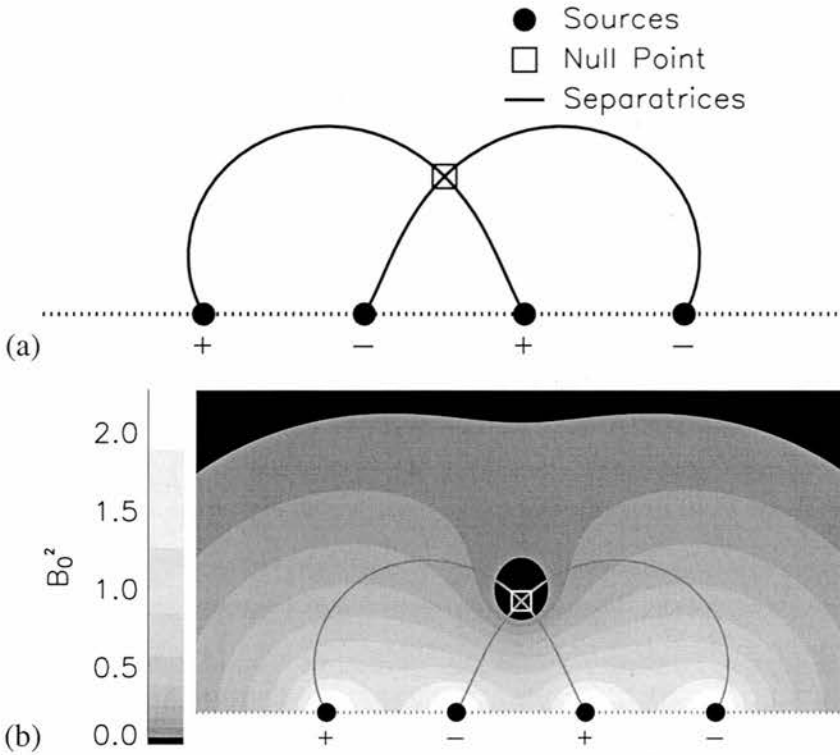


Figure 6.4: (a) Skeleton of the simple field arising from four sources positioned at $-0.3, -0.15, 0.15$ and 0.3 , with strengths $0.5, -0.5, 0.5$ and -0.5 , respectively, from left to right. The region studied extends between -0.5 and $+0.5$ in the x -direction, and between 0 and 0.5 in the y -direction. (b) Contour plot of B_0^2 for the initial potential field. Each contour level is a factor of 1.5 times the previous level. The skeleton of the field is overplotted.

6.5 Example: Four Sources

In order to demonstrate the properties of the field following a translational shearing motion, a case consisting of four sources, two positive and two negative (as shown in Figure 6.4(a)), is initially considered. If the sources were to represent network fragments, then typical source fluxes, source separations and field strengths would be 10^{18} – 10^{19} Mx, 14 Mm and 3 – 30 G, respectively. In this simple scenario, the sources alternate in polarity and are spaced at uniform intervals. The magnitudes of all the strengths are equal, and a contour plot of the unperturbed field is shown in Figure 6.4(b). A plot of the specific volume about the second source from the left is shown in Figure 6.5(a) as a function of a . The specific volume, in comparison with the values it takes close to the separatrix, is negligible in regions far from the separatrix. In fact, V_0 diverges at the separatrix, in the vicinity of which, as shown in Appendix D, it varies as

$$V_0(a) \approx \frac{L^2}{2|F|} \ln \left(\frac{4|F|}{|a - a^*|} \right), \quad (6.26)$$

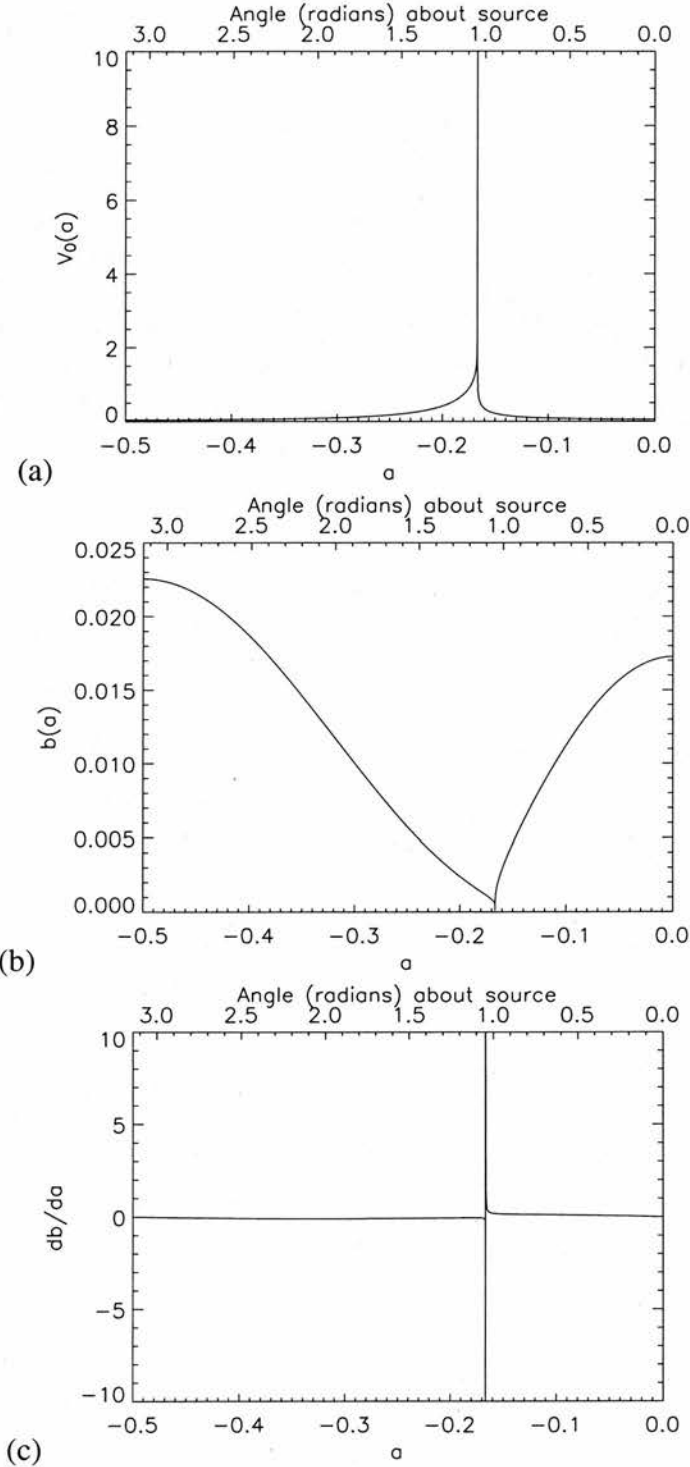


Figure 6.5: (a) Specific volume $V_0(a)$ as a function of a , rotated about the negative source located furthest to the left. Far from the region being examined, $a(-\infty, 0) = a(+\infty, 0) = 0$. (b) Resulting magnitude of the field b in the z -direction, which is constant along each field line. The magnitude of the displacement field b is minuscule in comparison with the poloidal field $|\mathbf{B}_0|$ —typically around 1%. (c) Derivative of b with respect to a ; the current density \mathbf{j} is given by $\mathbf{j} = (db/da)\mathbf{B}_0$.

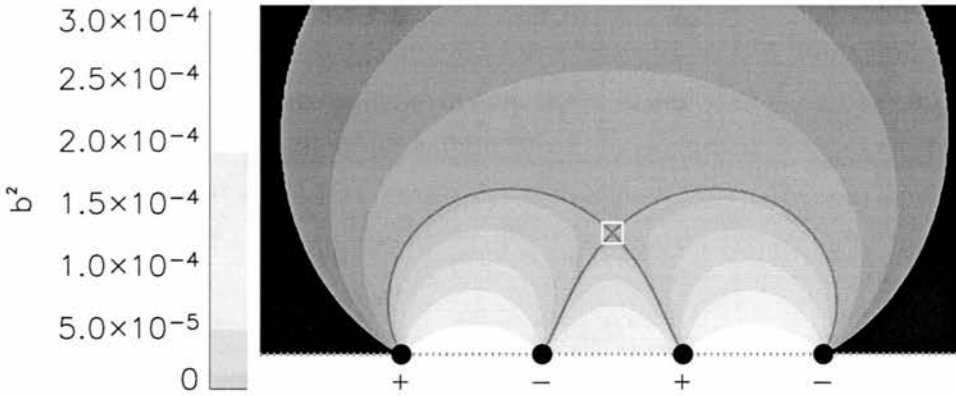


Figure 6.6: Contour plot of b^2 for the sheared field. Each contour level is a factor of 4 times the previous level. The skeleton of the field is overplotted.

where a^* is the value of $a(x, y)$ along the separatrix, L is a characteristic length scale and F may be identified as $F = \langle B_0^* \rangle L$ (here $\langle B_0^* \rangle$ is a representative value of the field calculated about the null). As such, F/L^2 is therefore a gradient of the field about the null point.

The two positive sources are then moved a distance of 5×10^{-4} units in the negative z -direction, whilst the negative sources are moved a distance of 5×10^{-4} units in the positive z -direction. The resultant b component of the perturbed field about the second source from the left is shown in Figure 6.5(b). Because $V_0(a)$ diverges on field lines passing close to the neutral point, the value of the perturbed component of the field $b(a)$ given by Equation (6.15) is very small on field lines passing close to the neutral point, and is zero on the separatrices themselves.

The derivative of $b(a)$ with respect to a is shown in Figure 6.5(c). Here it can be seen that the current given by Equation (6.17) is focused on the field lines that pass very close to the neutral point, and actually becomes infinite at the separatrix in this model. Priest et al. (2002) showed that this kind of behaviour is generic for systems with translational symmetry.

A contour plot of b^2 is shown in Figure 6.6. Since the free energy stored (i.e. that above potential) scales as b^2 , it can be seen that the bulk of the energy is stored low down in the system.

6.6 Effects of Complexity

The properties of the current sheets that occur in a $2^{1/2}D$ force-free field generated by applying small shearing motions to a potential configuration have been demonstrated above. However, it should be expected that complexity in the distribution of photospheric fragments plays a role in determining macroscopic quantities, such as the amount of energy stored and dissipated. Indeed, this complexity will affect, for example, the total number of neutral points and separatrix surfaces in the configuration. Energy storage and dissipation may depend drastically on properties other than just the r.m.s. flux of the photospheric fragments or their average density in the photosphere. They may depend, for example, on the statistics of the flux distribution among fragments, their spatial clustering properties (or lack thereof), or the mixing of polarities on the photospheric boundary. Extrapolating further, they might also depend on the possibly fractal character of photospheric flux distribution (or lack thereof) and its effective fractal dimension.

A simple exploration of the effects that complexity in the photospheric flux distribution may have on the magnetic energy storage and coronal heating has been undertaken here. Such a study, even for such a simplified model as that studied here, needs to be numerical. As such, limitations are placed on the distances between sources and the range that their fluxes cover.

Energy storage has been computed for several models with varying spatial flux distributions on the x -axis. These models also differ in the number of fragments involved and the distribution of flux among the different fragments. For example, in some cases the fluxes of the fragments are all equal in magnitude, whereas in other cases the fluxes are drawn from chosen statistical distributions. Similarly, the spatial distribution of fragments in space is in some cases taken to be deterministically simple and regular, whilst in other cases fragments are positioned randomly, and/or clustered to varying degrees. In all cases, the configuration is held in flux balance, with the total flux in the positive fragments equal in magnitude to the total flux contained in the negative fragments. In every run, the total absolute flux in the system is fixed at 2 arbitrary units.

The sources in each configuration have been placed between $x = -0.3$ and $x = +0.3$, with the region examined extending between $x = -0.5$ and $x = +0.5$. Table 6.1 summarises concisely the parameters of the experiments that are performed. Six cases are considered, as follows:

- (i) The sources are positioned regularly in space in sequences of two positive sources, followed by two negative sources, e.t.c.

Source Distribution	Distribution Pattern	Clustered?	Figures
(i)	++--++--...	No	(a),(b)
(ii)	++--++--...	Yes	(c),(d)
(iii)	+ - + - + - + - ...	No	—
(iv)	+ - + - + - + - ...	Yes	—
(v)	Random	No	(e),(f)
(vi)	Random	Yes	(g),(h)

Table 6.1: Summary of the source distributions described in the text. The '+' and '-' signs represent the polarity of each source in sequence that is placed on the photospheric axis. The 'Clustered' column indicates whether or not the sources are split into well-separated groups of four sources.

- (ii) The sequence of the source signs is the same as case (i); however, this time sources are grouped together into clusters of 4.
- (iii) The same as case (i), except that this time the sequence of the source signs varies alternately from one source to the next.
- (iv) The same as case (ii), but for the fact that the sequence of source signs also varies alternately from one source to the next.
- (v) Half the sources are positive, and half are negative. They are scattered randomly throughout the interval between $x = -0.3$ and $x = 0.3$.
- (vi) Similar to case (v); however, the sources are clustered in groups of four containing two sources of each polarity. Each source is positioned randomly within the interval that its group occupies.

In the cases where fragments are positioned in a regular (unclustered) way, each consecutive pair of sources is separated by a distance $0.6/(n - 1)$, where n is the number of sources in the given configuration. When sources are clustered into groups of 4, the intervals in which the sources are placed are $1/3$ of the separation between clusters.

In the following sections, several distributions of source strengths are considered. These include a constant distribution, where the magnitudes of all the sources are equal, a uniform distribution, where all the source strengths are selected randomly with a uniform probability, an exponential distribution, and a power-law distribution.

Source Distribution	Figure	Fitted Line
(i)	6.7(a)	$y = 5.5x - 17.3$
(ii)	6.7(c)	$y = 35x - 188.6$
(iii)	Similar to 6.7(a)	$y = 5.1x - 12.5$
(iv)	Similar to 6.7(c)	$y = 40.9x - 224$
(v)	6.7(e)	$y = 14.5x + 8$
(vi)	6.7(g)	$y = 137.9x - 815$

Table 6.2: Equations fitted to the graphs on the left-hand side of Figure 6.7. y represents the extra energy stored and x represents the number of sources through which the flux emerges.

6.6.1 Scenario 1: Constant Source Strengths

In order to consider the effects of having the field emerge through a varying number of sources, the number of sources in each case is initially set at eight. After having calculated the extra energy stored in such a field following a translational shearing motion, the number of sources through which the flux emerges is increased to 12. In turn, this is increased to 16, and so forth, until the number of sources has reached 200.

In the initial scenario, where all the sources are of equal magnitude, the cases in which the sources are spatially distributed in a symmetric way (cases (i)–(iv)) have, for a prescribed shearing motion, one unique value for the extra energy stored. However, in the cases where the sources are scattered randomly on the photospheric plane, there is an infinite number of possible fields. Thus, for a given number of sources, the extra energy stored is calculated for a sample of 50 fields.

Figure 6.7 shows plots of the energy stored versus the number of sources through which the flux emerges. By examining Figures 6.7(a) and (c), and Figures 6.7(e) and (g), it is clear that the clustering of the sources is the most important factor in affecting the amount of extra energy stored due to shearing motions; in the cases where the sources are clustered into groups of 4 (Figures 6.7(c) and (g)), the stored energy is significantly larger. The lines fitted to Figures 6.7(a), (c), (e) and (g) are given in Table 6.2. By comparison, the differences in stored energy incurred due to varying the sequence of the source signs on the photosphere, which invariably reflects the density of neutral points on the photospheric plane, is fairly minimal.

The right-hand side of Figure 6.7 shows the fraction of the extra energy, W , stored below a given height, h (here h is normalised to total width of the region under examination). It is clear that, in all cases, the height below which the majority of the energy is stored decreases as the number of sources increases. It is also clear from comparing Figures 6.7(b), (d), (f) and (h) that when there is a greater amount of energy, the height

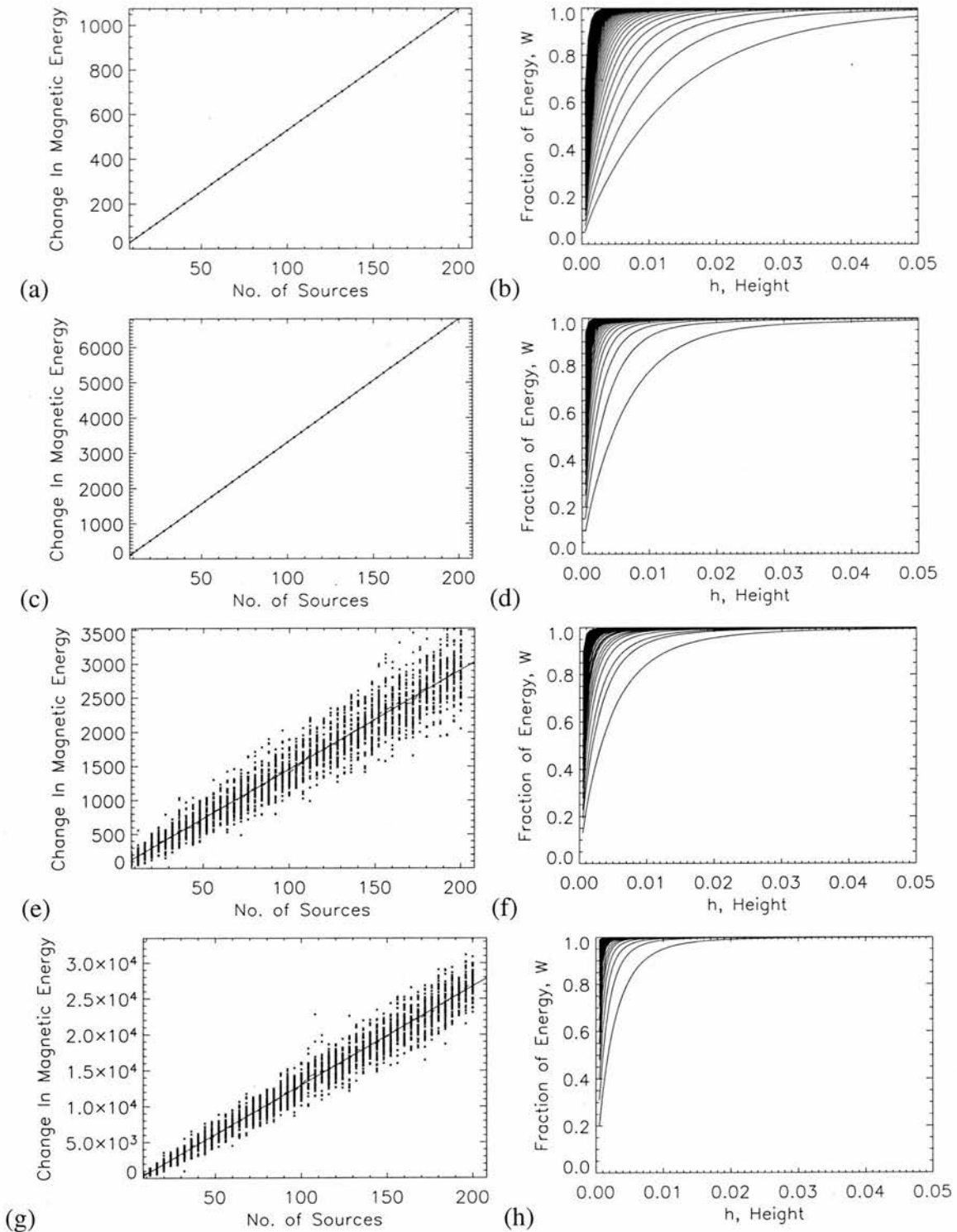


Figure 6.7: Plots of the extra energy stored per unit length in the z -direction (*left*) for distributions in which all sources have equal strength, versus number of sources. The source positioning for each of the graphs is summarised in Table 6.1. The fraction of the total energy stored in the system below a given height is given on the *right*. In each plot, the rightmost curve represents the values obtained with eight sources; proceeding leftwards, subsequent curves give the values obtained with 12, 16, 20... 200 sources. Thus, as the number of sources increases, the energy becomes stored lower and lower down.

below which the majority of the flux is stored is lower.

In all the cases, the amount of stored energy increases linearly as the number of sources is increased. This can be understood by carrying out a dimensional analysis. Considering a typical domain, the field is of the order

$$B_0 \sim \frac{\Phi_0}{L_0}, \quad (6.27)$$

where Φ_0 is a typical source flux and L_0 is a typical length scale of an average domain. Of course, the field contains contributions from other sources at distances greater than L_0 ; however, close to the photosphere the field is largely dominated by the sources at the boundaries of the domain, so that, even if there are thousands of sources in the configuration, only a few have a non-negligible contribution. The specific volume V_0 may then be expressed as

$$V_0 \sim \frac{L_0}{B_0} \sim \frac{L_0^2}{\Phi_0}. \quad (6.28)$$

This means that the extra energy stored, W_z , scales as

$$W_z \sim \frac{\Phi_0}{V_0} \sim \frac{\Phi_0^2}{L_0^2}. \quad (6.29)$$

If the number of sources is then increased by a factor of \mathcal{N} from N to $\mathcal{N}N$, then the flux Φ_0 and length L_0 change in the following way:

$$\Phi_0 \rightarrow \frac{\Phi_0}{\mathcal{N}} \quad \text{and} \quad L_0 \rightarrow \frac{L_0}{\mathcal{N}}, \quad (6.30)$$

Clearly, as the number of sources is increased, the energy stored in a typical domain remains, on the whole, unchanged. However, the number of domains into which the flux is partitioned does increase. As has already been seen, domains with long connections (which by their very nature are the ones that reach higher into the corona) do not contribute much to the extra stored energy W_z . Thus, the majority of the extra energy above potential comes from the domains that lie along the photospheric axis. In a two-dimensional configuration there is typically one such domain per source, so that, when the number of sources is increased by a factor \mathcal{N} , then the extra energy W_z increases accordingly:

$$W_z \rightarrow \mathcal{N}W_z. \quad (6.31)$$

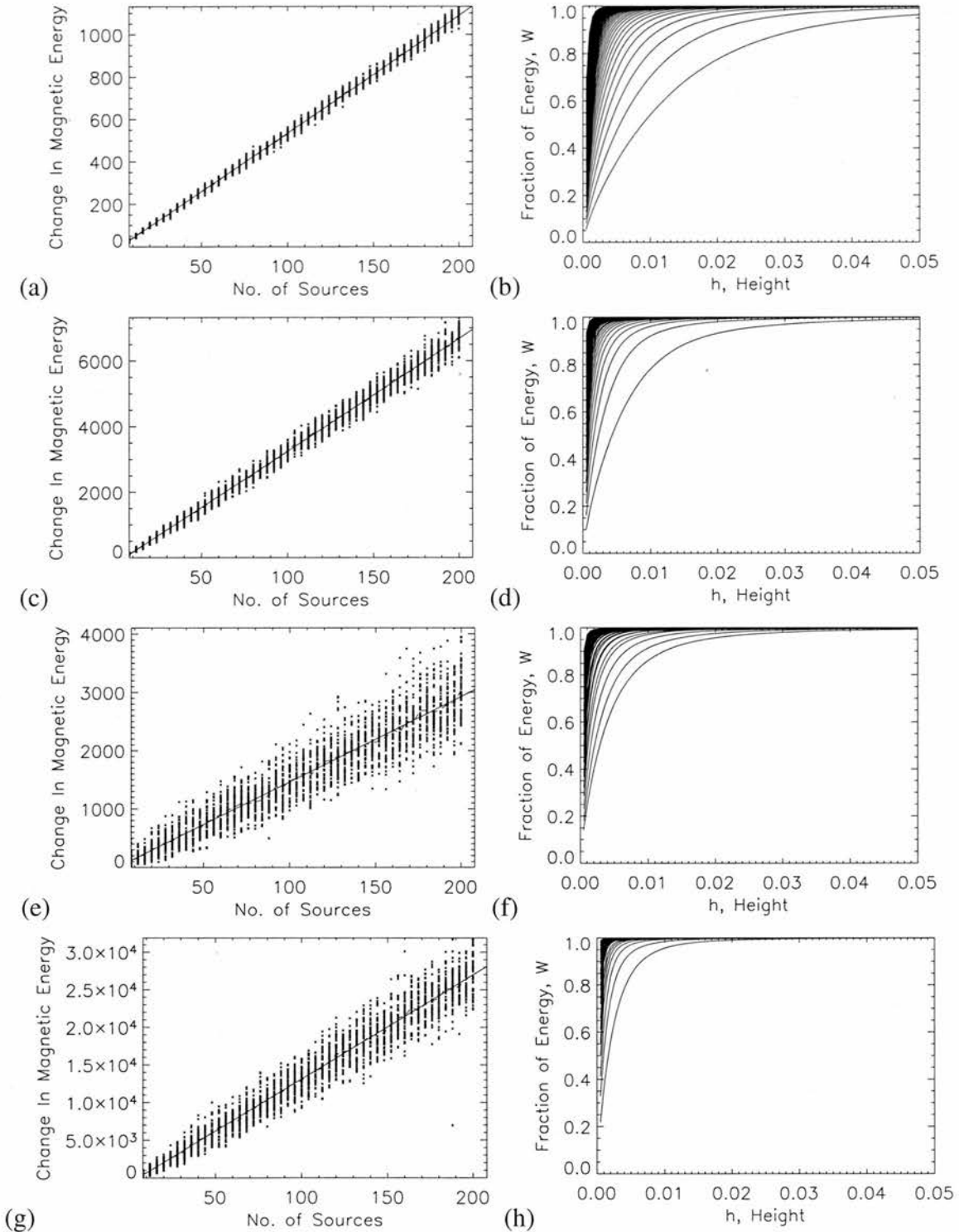


Figure 6.8: Plots of the extra energy stored per unit length in the z -direction (left) when source strengths are selected from a uniform distribution, versus number of sources. The source positioning for each of the graphs is summarised in Table 6.1. The fraction of the total energy stored in the system below a given height is given on the right. In each plot, the rightmost curve represents the values obtained with eight sources; proceeding leftwards, subsequent curves give the values obtained with 12, 16, 20... 200 sources. Thus, as the number of sources increases, the energy becomes stored lower and lower down.

Source Distribution	Strength Distribution	Figure	Fitted Line
(i)	Uniform	6.8(a)	$y = 5.5x - 16.3$
(ii)	Uniform	6.8(c)	$y = 34.3x - 184.4$
(iii)	Uniform	Similar to 6.8(a)	$y = 5.7x - 14.1$
(iv)	Uniform	Similar to 6.8(c)	$y = 44.5x - 246.8$
(v)	Uniform	6.8(e)	$y = 14.6x - 0.17$
(vi)	Uniform	6.8(g)	$y = 138.4x - 699.3$
(i)	Exponential	Similar to 6.8(a)	$y = 5.6x - 20.4$
(ii)	Exponential	Similar to 6.8(c)	$y = 34.2x - 195.3$
(iii)	Exponential	Similar to 6.8(a)	$y = 5.9x - 16.8$
(iv)	Exponential	Similar to 6.8(c)	$y = 44.7x - 254.5$
(v)	Exponential	Similar to 6.8(e)	$y = 14.8x + 2.4$
(vi)	Exponential	Similar to 6.8(g)	$y = 140.5x - 773.5$
(i)	Power Law	Similar to 6.8(a)	$y = 5.6x - 13.9$
(ii)	Power Law	Similar to 6.8(c)	$y = 34.2x - 170.2$
(iii)	Power Law	Similar to 6.8(a)	$y = 6.2x - 15.7$
(iv)	Power Law	Similar to 6.8(c)	$y = 44.4x - 236.7$
(v)	Power Law	Similar to 6.8(e)	$y = 14.8x + 3.7$
(vi)	Power Law	Similar to 6.8(g)	$y = 138.4x - 709.6$

Table 6.3: Equations fitted to data for the uniform source-strength distribution (Figure 6.8), the exponential source-strength distribution, and the power-law source-strength distribution. y represents the extra energy stored and x represents the number of sources through which the flux emerges.

Hence W_z should be expected to increase linearly with \mathcal{N} , which of course it does.

6.6.2 Scenario 2: Random Source Strengths

Having studied the behaviour due to sources that are all of constant magnitude, fields emanating from sources whose strengths are chosen at random are now analysed.

In order to do this, three different source-strength distributions are considered; a uniform distribution, an exponential distribution, and a power-law distribution. In all these cases, the source strengths are selected randomly from the range $[0.1, 1]$. In this way, it is ensured that there are no neutral points that lie too close to any of the sources, which of course would make it difficult to resolve the problem computationally. The sources are then scaled so that the sum of the positive sources is 1, and the sum of the negative sources is -1 .

For each of the 6 different spatial distributions, the experiment is performed over a sample of 50 fields, since randomly selecting source strengths means that there is an

infinite number of fields, even when there is spatial symmetry in the distribution of the sources.

Figure 6.8 shows the results obtained using the uniform distributions (results obtained for the exponential and power-law distributions are similar). By comparing the plots in all three figures, it can clearly be seen that the results obtained for the various spatial distributions are all very similar. This naturally implies that the distribution of source strengths has little effect on the extra energy stored due to the shearing motions. This is further backed up by looking at the equations of the lines fitted to the plots, given in Table 6.3. For a particular spatial distribution, the lines fitted to the data obtained from the three separate source-strength distributions are practically the same.

6.7 A Comparison of Separator and Separatrix Heating

In this section, the four-source quadrupolar configuration of Section 6.5 is re-examined in order to make a simple comparison between heating resulting from the formation of current sheets upon separatrices and heating resulting from the formation of current sheets along separators.

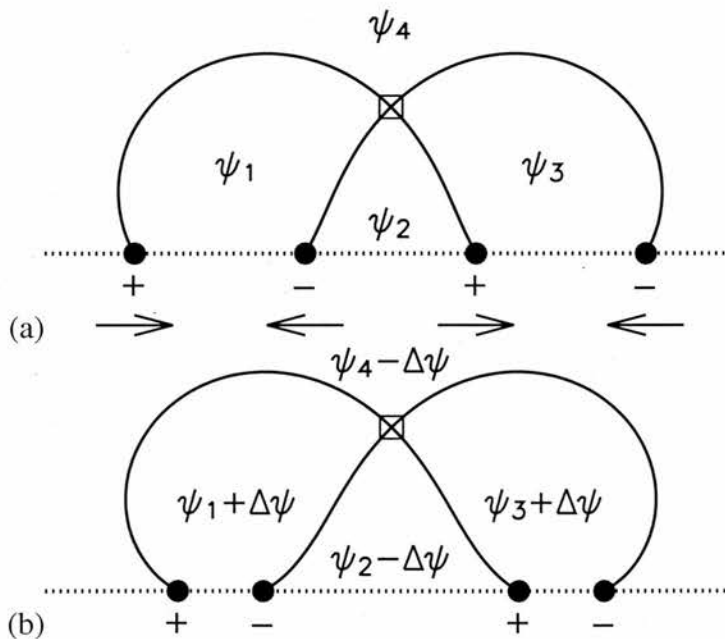


Figure 6.9: (a) Sketch of initial source configuration, with the directions in which the sources are displaced shown by arrows. The domain fluxes are shown by ψ_1 , ψ_2 , ψ_3 and ψ_4 . (b) The configuration after the source displacement. Domains \mathcal{D}_1 and \mathcal{D}_3 have had their fluxes increased by an amount $\Delta\psi$, whilst the fluxes of domains \mathcal{D}_2 and \mathcal{D}_4 have decreased by the same amount.

6.7.1 2D Separator Current Sheet Formation

Since the magnetic field in two dimensions is translationally symmetric, the sources are of infinite length in the direction of invariance (here taken to be the z -axis). This also means that the neutral point has an infinite extent in the z -direction, and is in fact a neutral line. In light of this, the calculation is restricted to a finite portion of the system by placing conducting boundaries at the planes $z = 0$ and $z = 1$ (Longcope, 2001). Furthermore, in this 2D model, the role of the 3D separator, which generally lies at the confluence of four separate magnetic domains, will be played by the neutral line, which also lies at the confluence of four domains.

In this simple 2D scenario, illustrated in Figure 6.9(a), the four sources are linked in all possible ways by the domains \mathcal{D}_1 , \mathcal{D}_2 , \mathcal{D}_3 and \mathcal{D}_4 , which have fluxes ψ_1 , ψ_2 , ψ_3 and ψ_4 , respectively. Since all source strengths are of equal magnitude, it turns out that $\psi_1 = \psi_3$ and $\psi_2 = \psi_4$. Displacing the sources along the x -axis in a vacuum magnetic field will in general lead to changes in the domain fluxes ψ_i ($i = 1 \dots 4$). Following the displacement shown in Figure 6.9(a), domains \mathcal{D}_1 and \mathcal{D}_3 have their fluxes increased by an amount $\Delta\psi$, whilst domains \mathcal{D}_2 and \mathcal{D}_4 have their fluxes decreased by the same amount. However, in the stick-slip reconnection model of Longcope (1996), the field is assumed to thread a perfectly conducting plasma, which does not permit any flux to pass through the neutral point. Thus, a current ribbon with total current I forms along the neutral line with an orientation and self-flux such that it cancels $\Delta\psi$. Longcope (2001) showed that the current I and self-flux $\psi^{(cr)}$ are related by

$$\psi^{(cr)}(I) \equiv -\Delta\psi(I) = \frac{\mu_0 I}{4\pi} \ln \left[16\pi e \frac{I_*}{\mu_0 |I|} \right], \quad (6.32)$$

where I_* is a characteristic current for the potential neutral point and is given by $I_* \equiv B' Y_N^2$ (Y_N is the y -coordinate of the neutral point and B' is defined as $|\nabla \mathbf{B}_0|$ calculated at the neutral point, with \mathbf{B}_0 denoting the initial vacuum field). Strictly, this expression is only valid in the vicinity of the neutral point (i.e. when $|I| \ll I_*$). The free energy above potential (ΔW) stored by this current build-up is given by

$$\Delta W = \frac{1}{2} I (\Delta\psi) \Delta\psi. \quad (6.33)$$

Rather than allowing the current to build up indefinitely, the model of Longcope (1996) places a limit on the quantity $I_*/|I|$, so that, once such a threshold is reached, a ‘nanoflare’ is assumed to occur, in that an electric field parallel to the neutral line ensues and consequently allows the flux $\Delta\psi$ to pass through the neutral point. It is also assumed that

$\Delta\psi \rightarrow 0$, i.e. the field returns to its vacuum state, which is precisely the potential field arising from the sources positioned as they are at the onset of the flaring event.

6.7.2 Analogous Separatrix Stick-Slip Reconnection

The current per unit length in the z -direction across a separatrix resulting from the shearing motions described in Section 6.3 follows from Equation (6.17), and is given by

$$I'_i = \int_{\mathcal{L}_i} \mathbf{j}_i \cdot d\mathbf{l} = \int_{\mathcal{A}_i} \left(\frac{db_i}{da} \right) da, \quad (6.34)$$

where \mathcal{L}_i follows the path of the separatrix i and \mathcal{A}_i is across the separatrix. For the purpose of making a comparison between the two heating models, a representative current I'_{*i} ($i = 1 \dots 4$) for each separatrix is defined as

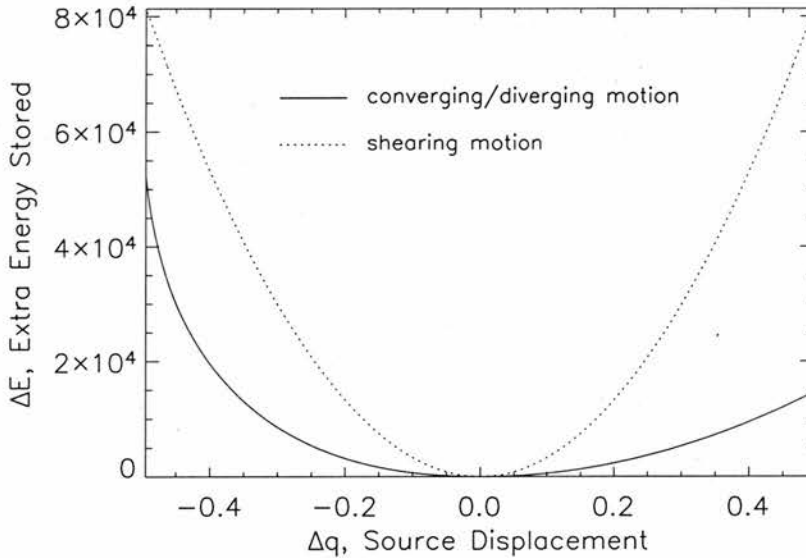


Figure 6.10: Extra energy stored (ΔE) as a function of source displacement (Δq) for the two different scenarios. The displacement axis is normalised to the initial separation between each of the sources. Extra energy stored following the shearing motions is given per unit length in the z -direction.

$$I'_{*i} = |\mathbf{B}_{mi}| L_i, \quad (6.35)$$

where L_i is the length of the separatrix curve i and \mathbf{B}_{mi} is the value of the poloidal field at the midpoint of the separatrix. Since the values of I_* and I'_{*i} ($i = 1 \dots 4$) are not directly comparable, a more universal criterion for comparing the two mechanisms must be found, hence the actual values of the various I'_{*i} are not too critical. In fact, due

to the translational symmetry along the z -axis, all the I'_{*i} ($i = 1 \dots 4$) remain constant throughout the evolution of the system (unlike I_* , which changes its value after every event (i.e. release of energy)). It is assumed that when any one of the four $I'_{*i}/|I'_i|$ reaches a threshold value, an instability occurs and the energy stored in the system is released. Thus $I'_i \rightarrow 0$ for all i .

6.7.3 Comparison of Energy Storage

The evolution of the two configurations is managed such that each source is displaced by an amount Δq . In the separator heating scenario, the sources are displaced along the x -axis in accordance with the description in Subsection 6.7.1, while in the separatrix heating scenario, the sources are sheared along the z -axis in accordance with Section 6.5.

The value of Δq is normalised to the initial distance between neighbouring pairs of sources, and is varied between the limiting values of -0.5 and 0.5 . In the case of displacements along the x -axis, when $\Delta q = -0.5$ the two central sources cancel and the null point disappears; when $\Delta q = 0.5$, the leftmost pair of sources cancels, as does the rightmost pair of sources, resulting in a magnetic void.

Figure 6.10 shows how the extra energy above potential would vary for the two types of source motions were the energy storage to increase unimpeded. The plot suggests that energy storage associated with separatrix currents is more efficient than energy storage associated with separator currents, with the ratio of separatrix to separator energy being typically 2–4. It should be noted, however, that the values calculated for the larger displacements are less reliable, since the validity of Equations (6.25) and (6.33), which give the extra energy stored by the two systems, becomes somewhat overstretched.

The three plots in Figure 6.11 show how the extra energy stored (ΔE) by the two configurations varies with the mean displacement between flaring events. As one would naturally expect, small source displacements between events (which are a consequence of placing low thresholds on the values of the peak currents allowable) result in frequent releases of energy, and therefore not so much energy is stored between events as is stored when there are large displacements between the flaring events. The question that then arises is: what releases a greater amount of energy in total—frequent releases of small bundles of energy, or less frequent releases of relatively large bundles of energy? This question is addressed by Figure 6.12, which shows that in both the scenarios less frequent releases of energy result in a greater amount of energy being released in the long run. What is also shown is that, for a given mean source displacement between events, the total

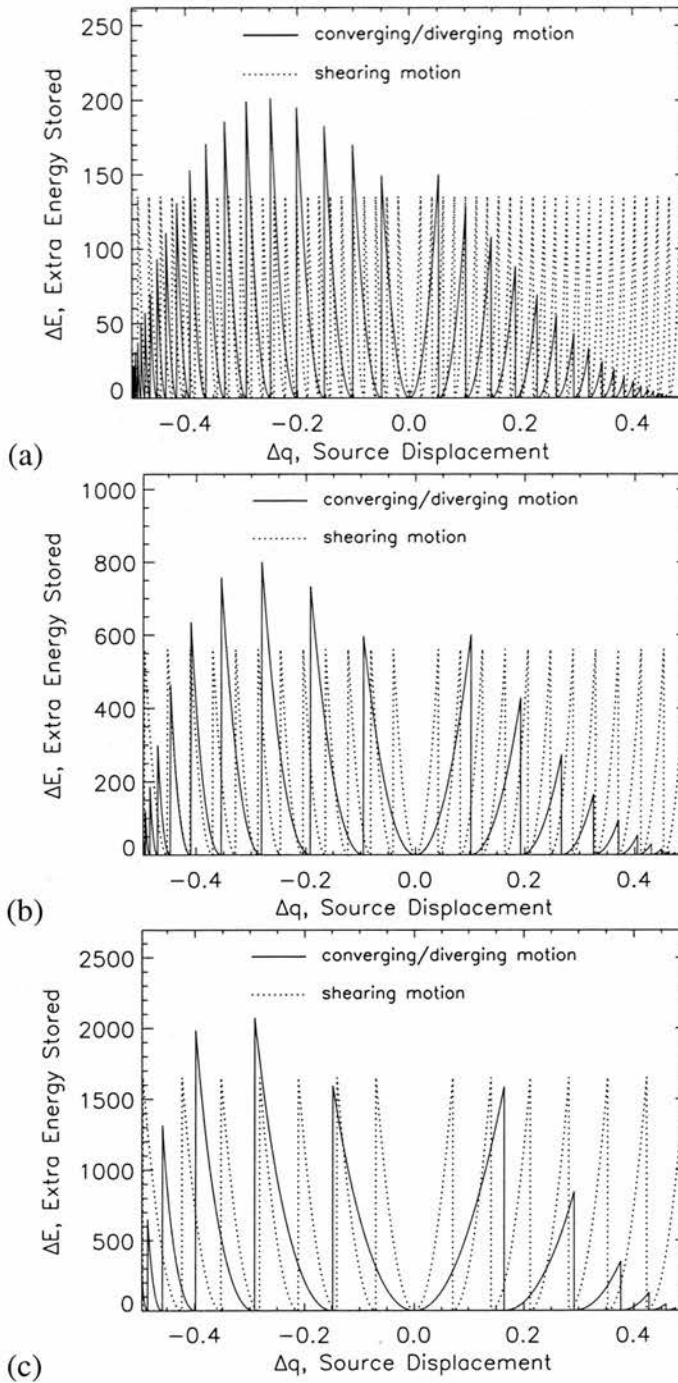


Figure 6.11: Extra energy stored (ΔE) as a function of source displacement (Δq) for mean source displacements of (a) 0.02, (b) 0.04 and (c) 0.07 between events.

amount of energy released by the separatrix heating model is around twice as much as that released by the separator heating model. This simple analysis suggests that separatrix heating and separator heating both make significant contributions to coronal heating, with separatrix heating being somewhat more prevalent.

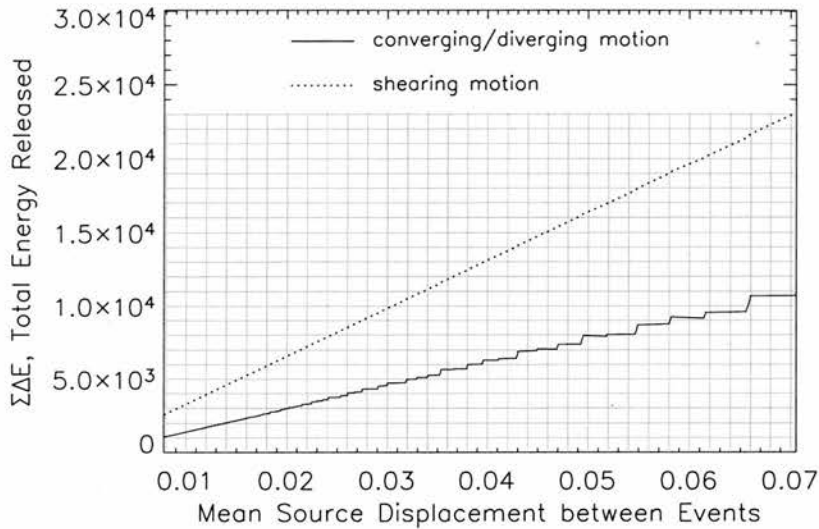


Figure 6.12: Plot showing how the total energy released by the system ($\Sigma\Delta E$) varies as a function of the mean source displacement between events.

6.8 Conclusions

The effects of applying simple shearing motions to a series of line sources in a translationally symmetric magnetic field have been studied here. It has been shown that these motions lead to highly concentrated currents on the separatrices that are present in the system, with essentially no currents flowing far from them. The extra energy generated by these shearing motions is stored very low down in the system, with little energy stored in the overlying upper coronal domains. In other words, the heating preferentially occurs near the footpoints of coronal loops, in agreement with observations of TRACE loops.

By conserving the total amount of flux in the system, along with the length scales over which the flux emerges, it has been found that increasing the number of sources through which the flux emerges results in an increased amount of stored energy arising from the shearing motions. On the Sun, it is more natural to expect the total absolute flux to increase as one considers smaller and smaller scales. This is because magnetogram images are comprised of a multitude of finitely sized pixels, meaning that opposite-polarity magnetic structures that exist on scales smaller than the dimensions of the pixel elements are likely to suffer from cancellation effects. Thus, all that is registered in a given magnetogram pixel is the net flux of the region covered by that pixel.

Nevertheless, this study has shown that the introduction of complexity alone may greatly increase the energy storage of a given system. Such a discovery is of particular relevance at the moment, where there is a growing realisation of the importance of fine-scale structures in the problem of how the corona is heated.

The results obtained here have natural implications regarding what should be expected in three dimensions. Although the Grad-Shafranov equation does not hold in 3D, making an analysis that is analogous to the work presented here extremely difficult, one would expect to find results in 3D that are similar to those found here. (Indeed, Priest et al. (2002) have already shown how currents may build up on 3D separatrix surfaces by considering a configuration comprising point sources placed in a grid-style pattern on two infinite lattices at $z = -L$ and $z = L$). It would seem fairly intuitive to expect that the majority of the energy in a 3D system is also stored predominantly by the low-lying loops. However, it is shown in Appendix E that the amount of free energy arising from shearing motions in 3D should be expected to fall as \mathcal{N} as a linear decrease in the length scale is considered (although the amount of free energy arising from such shearing motions falls as $\sqrt{\mathcal{N}}$ when the number of sources increases linearly). This contrast with the 2D scenario arises because in 2D, the number of sources is related linearly to the length scale; in 3D, there is an extra dimension to consider when placing sources on the photosphere. This means that the number of sources should grow quadratically as the length scale decreases, therefore affecting the amount of extra energy stored. The consequence of this discrepancy is that merely increasing the number of sources through which the magnetic field arises will not increase energy storage in 3D; however, this assumes that the total amount of flux remains constant as smaller scales are considered, which (as discussed above), is not the case on the Sun. Thus, on the real Sun, the stored energy will likely increase as smaller scales are considered. The rate at which the stored energy increases will depend on the rate at which the amount of flux observed increases.

The simple comparison of separator heating and separatrix heating given here has suggested that coronal heating associated with shearing motions and subsequent current concentrations on separatrices play a substantial role in coronal heating, with indications that it may actually be more efficient at heating the corona than heating associated with currents confined to separators. It will be interesting to see how future work involving more complicated systems compares with the results found here.

Chapter 7

Discussions and Future Work

梶原 笹臣	降	な	天	No sky
	り	し	も	No earth– but still
	し	た	地	The snowflakes fall
	き	だ		
	る	も		
		雪		
		の		

KAJIWARA HASHIN (1864–?)

7.1 Discussion

Several previous authors, such as Inverarity and Priest (1999), Brown and Priest (1999b, 1999a, 2000, 2001) and Beveridge et al. (2002) have produced some insightful work that has greatly advanced our understanding of the configurations that one might expect in a magnetic carpet environment and the (often subtle) relationship between the various states. Whilst their work tended to focus upon the interactions between only a handful of magnetic sources, other studies, motivated by the existence of multitudes of magnetic sources in the quiet-Sun photosphere, have aimed more at estimating the statistical properties of model magnetic fields arising from hundreds of sources (e.g. Schrijver and Title, 2002; Longcope et al., 2003 ; Beveridge et al., 2003).

The work presented in this thesis has followed in the same vein as the later case and considered magnetic fields arising from a great many point sources scattered on a model photosphere. In Chapter 2, such point sources were used to represent the fragments observed in MDI magnetogram data. With each fragment itself being comprised of several point sources, it was found that 50% of quiet-Sun flux closes down at chromospheric heights or lower (i.e. < 2.5 Mm), with only 5–10% of flux reaching heights of 25 Mm or

higher. It was also shown in Chapter 2 that a given fragment may connect to between 1 and 75 opposite-polarity fragments, the average being 5. Whilst the larger fragments tend to connect to more fragments, the majority of their flux is distributed among only a few nearby neighbours, with approximately 60–70% of flux connecting solely to an adjacent neighbour.

Chapter 3, in contrast, examined the domain structures themselves that interconnect the magnetic fragments previously discussed in Chapter 2. This involved representing each fragment as a single point source and using the techniques of magnetic charge topology to identify the boundaries of each domain. Such analysis required the development of an algorithm for efficiently tracing separator field lines. It was found that, although there are generally only two types of domain observed in 3D potential magnetic fields, namely separator-ring domains and isolated domains, non-trivial differences between domain structures that exist under both of these categories mean that they may be classified further. Such a classification will be a useful tool as heating models of increasing complexity are considered.

The work in Chapter 4 provided a statistical analysis of magnetic separators in magnetic fields based on both simulated source distributions and observed source distributions. In the case of the simulated fields, this involved replicating the results of Schrijver and Title (2002) in order to obtain a population of nulls from which to track separators. It was found that separators are generally more abundant than one would imagine, with pairs of nulls often being linked by more than one separator. As well as establishing that separators tend to bunch together to form trunks, Chapter 4 also showed that many pairs of coronal nulls are connected by separator field lines, suggesting that perhaps bifurcations in the corona are a common way of creating coronal nulls.

Chapter 5 again made use of observed magnetogram data. Having already shown in Chapter 2 how flux from a given fragment is typically apportioned between connected opposite-polarity fragments, the aim of this chapter was to gauge how the dynamic behaviour in the photosphere affects the configuration in the corona above. After developing a method with which to determine how variations in source strengths affect domain fluxes, it was then established that, when emergence and cancellation of flux are considered, the magnetic field in the corona is replaced in around only 1.4 hours by the process of reconnection (when emergence and cancellation are prohibited, this figure increases to around 3 hours). It was then estimated that to achieve the observed heating rate of 300 W m^{-2} (Withbroe and Noyes, 1977) by means of separator reconnection requires a mean current of $2 \times 10^{10} \text{ A}$ to be flowing along the separators in the configuration (when emergence

and cancellation are neglected in the calculation, this figure becomes 5×10^{10}).

In Chapter 6, a $2^{1/2}$ D translationally symmetric geometry was considered in order to study the effects of complexity on the build-up of currents on separatrices following a simple shearing motion of the magnetic sources. It was established that the amount of free energy stored increases as the number of sources through which the flux emerges is increased. This energy is stored lower and lower down as more sources are considered. Chapter 6 also provided a simple comparison between coronal heating resulting from separatrix currents and coronal heating resulting from separator currents in a $2^{1/2}$ D quadrupolar configuration. In such a scenario, it was found that the two forms of heating release comparable amounts of energy, with separatrix heating being the more dominant.

7.2 Future Work

Developing a better understanding of the quiet-Sun photosphere and the heating of the overlying corona is a multi-faceted affair, with various angles from which the matter may be approached.

Advances in observational capabilities over recent years have resulted in an increasing realisation of the importance of small-scale magnetic fields. Indeed, as the spatial resolution available to observers increases, it is natural to expect that more and more magnetic flux should be discovered, as the mixing of polarities on scales below current magnetogram resolutions reduces polarisation, effectively hiding such flux from the observer. Thus, a challenge for the observationalists is to determine empirically the full complexity of the magnetic fields that emerge through the solar photosphere.

It was shown in Chapter 2 that intranetwork concentrations, rather than closing down entirely at low levels, actually contribute to the coronal field over quiet-Sun regions. Recent indications by Schrijver and Title (2003), obtained using a theoretical model, suggest that as much as 50% of the coronal field over quiet-Sun regions may originate in such weak intranetwork concentrations. A qualitative follow up to this work based on observed data is required in order to confirm these findings.

Whilst the larger of the intranetwork fragments were included in the calculation of the recycling times given in Chapter 5, in future a reworking of the analysis that includes the multitudes of weaker intranetwork fragments along with the full complexity of the substructures within fragments will also be necessary.

From a topological viewpoint, there are several important areas for development.

Multiple domains, noted in Chapters 3 and 4, warrant further study in order to understand the bifurcations that bring about their existence. More investigation is also required to uncover the properties of coronal domains; although thorough studies of configurations arising from small numbers of sources have provided a wealth of knowledge regarding the low-lying domains that intersect the photosphere, coronal domains generally tended to be absent from these models. As large-scale connections are typically through coronal domains, a study that demonstrated a series of bifurcations through which flux from a given source emerges through the photosphere, rises up into the corona and then forges large-scale connections would be highly interesting.

Topological models of the quiet Sun could also explore the consequences of the study by Schrijver and Title (2003) in terms of null point statistics and how our new understanding of the structure of the quiet-Sun magnetic field affects the density and location of null points within the corona.

The major disadvantage of using potential field models to extrapolate the magnetic field into the corona is that, being in the lowest energy state, they allow no extra energy to be stored. Certainly, as higher order force-free models are considered, one should expect new topological behaviour to present itself alongside the behaviour already observed in potential field models. Preliminary discussions on force-free topology have been presented (e.g. Longcope (1996), Brown and Priest (2000), Maclean et al. (2004)); however, as of yet the subject remains largely unexplored.

With regard to the subject of coronal heating, the extent to which the various proposed mechanisms play a role in dissipating the energy stored in the coronal magnetic field is still unknown. From a reconnection viewpoint, a key unsolved question at the moment is whether separator heating is more or less efficient than separatrix heating. With recent analytical work by Priest et al. (2004), together with the experiment in Chapter 6, concluding that both are likely to be important for coronal heating, a natural progression would be a quantitative analysis of the role played by each mechanism in complex model fields. A starting point could be to expand the work in Section 6.7 to more complicated fields arising from many sources and containing a multitude of neutral points. It would be interesting to see what effects mutual induction and subsequent sympathetic flaring (Longcope, 1996) have on the pattern of energy storage and release by the system. A more involved analysis would be to consider a 3D numerical simulation that contained both separator and separatrix currents, and to calculate the resultant energy dissipation at both locations.

Appendix A: Comparison of Photospheric Fragment Representations

Here a comparison is made between the fields produced by two different methods of representing the flux fragments in the balanced region of the magnetogram studied in Chapter 2. As with Chapter 2, the central $\frac{1}{3} \times \frac{1}{3}$ is studied, with the 8 surrounding magnetogram squares being included for the purpose of removing the potential bias of edge effects within the region of study. Hence, this is essentially the configuration of Section 3.4, but with 8 surrounding squares included.

In the first representation, all the pixels in the magnetogram are represented by a single point source, as in Chapter 2. Setting the minimum number of pixels in a given fragment to 10 results in each fragment being represented by at least 10 point sources. This representation has the advantage that it retains something of the general geometric character of the fragment. In the second representation, each fragment is represented by a single point source. Other possibilities for representing magnetic fragments include placing sources below the photosphere, hence avoiding singularities in the photospheric plane (Démoulin et al., 1992), or modelling a fragment by a circular region in the photosphere, within which the normal field is uniform and vanishing outside of it (Lothian and Browning, 1995).

In both representations considered here, a single field line represents 7.73×10^{15} Mx, so that more field lines are traced from stronger fragments. Field lines are traced both forward from positive fragments and backwards from negative fragments using the method of Section 2.2 for determining the starting points for field lines. Since flux closing within the inner region is accounted for twice (i.e. once when calculating field lines from positive fragments, and once from negative fragments), it is only right that field lines closing outwith the inner region should be counted twice, so as to fully account for all the

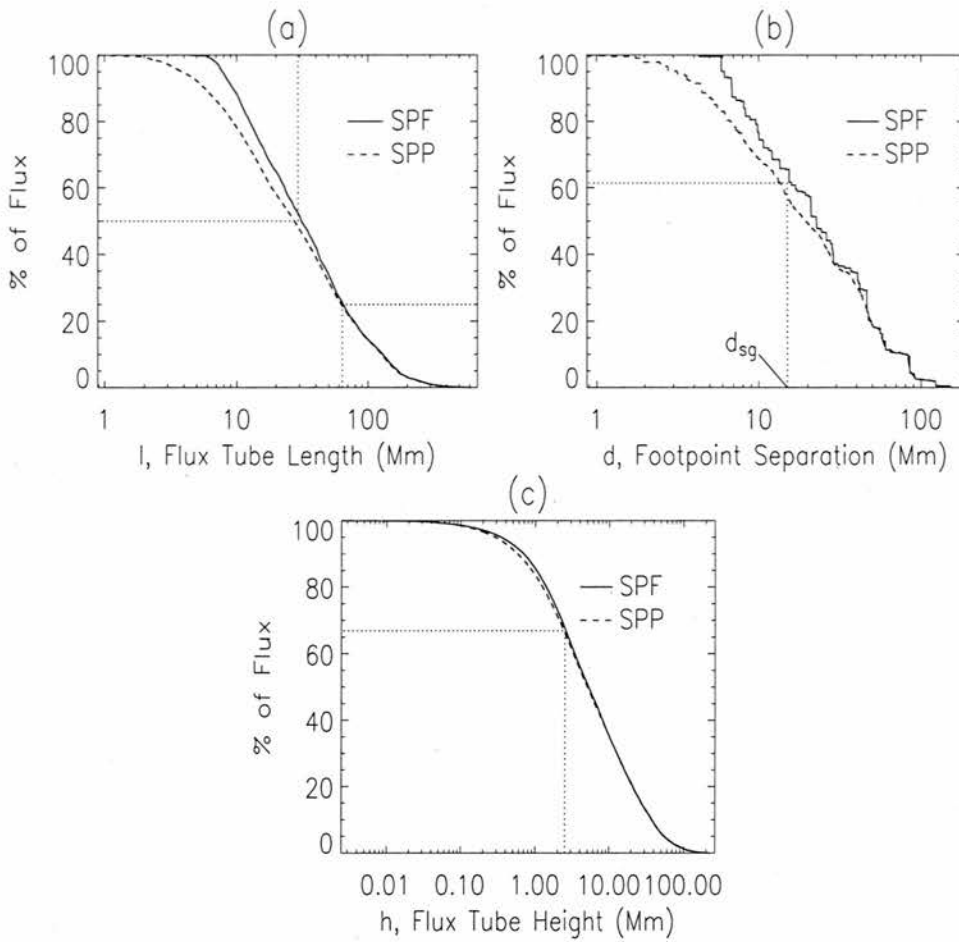


Figure A.1: Percentage of flux tubes with (a) length greater than l , (b) footpoint separation greater than d and (c) height greater than h . In all three plots, the *solid lines* represent the field lines calculated using the point-source-per-fragment representation, and the *dashed lines* represent the flux tubes calculated using the point-source-per-pixel representation.

flux within the inner region.

A.1 Flux Tube Characteristics

Figure A.1(a) shows the contrast in flux tube lengths obtained by the two representations. As one would expect, the two representations differ mostly at the lower end of the length distribution. With the point-source-per-pixel approximation, flux tubes as short as 0.88 Mm can be found, whereas the point-source-per-fragment approximation only allows for flux tubes as short as 4.3 Mm. A glance at Figure 3.5 in Section 3.4 confirms why this should be so; one can see opposite-polarity fragments literally touching each other. In the point-source-per-fragment approximation, there is a greater limit to how close two point sources may lie, as each point source lies at the “centre of gravity” of a cluster of

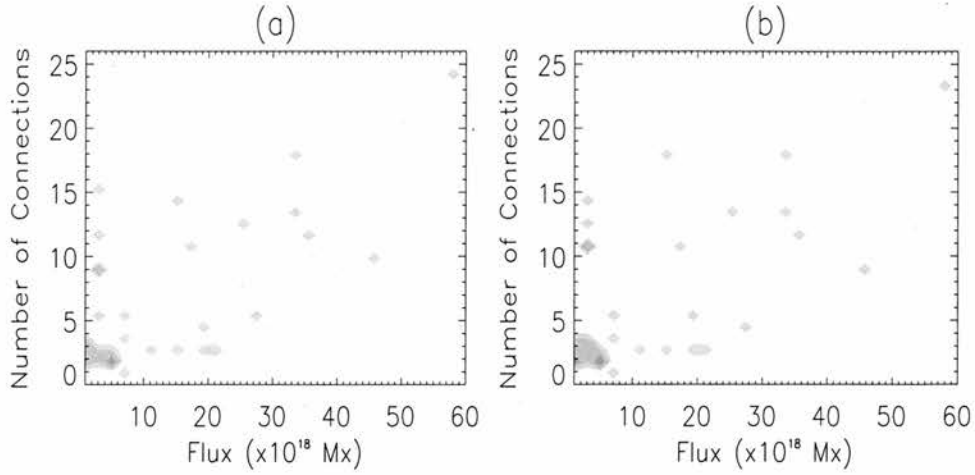


Figure A.2: Contour plots showing the the number of fragments to which a fragment of given flux connects for (a) the point-source-per-pixel representation and (b) the point-source-per-fragment representation

the (at least) ten pixels that comprise each fragment (of course, the point-source-per-pixel approximation places a point source at the centre of each pixel, so the minimum length of flux tube attainable is exactly the side length of a pixel).

As the length of the flux tube considered is increased, the two approximations converge to one another, so that the longest 50% of flux tubes have practically the same distribution in both representations. This also shows in the mean lengths of flux tubes found, as the point-source-per-pixel representation gives a mean flux tube length of 50 Mm, whilst the point-source-per-fragment representation gives the mean flux tube length as being only slightly longer at 53 Mm. The longest 25% of flux tubes have essentially the same distribution, with the longest flux tubes found at around 620 Mm.

Figure A.1(b) paints a similar picture for the footpoint separation of the flux tubes. Below the scales of typical supergranular diameters (around 14 Mm), the two representations differ quite greatly. As already discussed, the minimum footpoint separation in the point-source-per-pixel approximation is 0.88 Mm, whereas the minimum footpoint separation in the point-source-per-fragment representation is 4.3 Mm. This will therefore be the minimum separation between point sources in this representation.

The longer ends of the distributions are again essentially the same for both representations. However, the point-source-per-pixel representation gives a maximum footpoint separation of 160 Mm, whilst the maximum footpoint separation found by the point-source-per-fragment representation is 150 Mm. This is a hint that, whilst one would expect the topology of both regions to be on the whole quite similar, the connectivity of the two configurations should also be expected to differ in places.

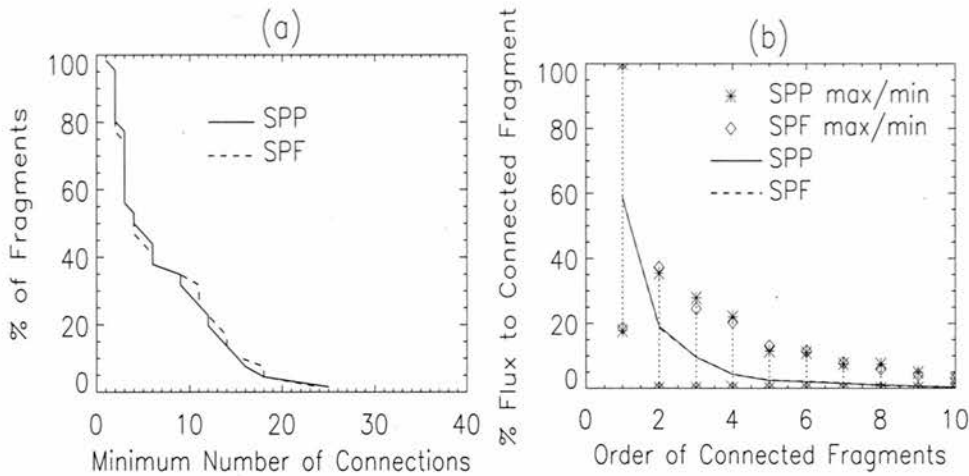


Figure A.3: (a) Percentage of fragments against the minimum number of connections of that fragment. (b) Mean proportion of flux for each fragment to which a given fragment connects.

The distribution of the maximum heights reached by the flux tubes is given by Figure A.1(c). Here it can be seen that the distributions obtained by both approximations are almost identical, at both the shorter and the longer ends of the scale. This perhaps indicates how well the field produced by a single point source resembles the field of a more complex configuration at a sufficient distance. The previous two plots (Figures A.1(a) and (b)) show greatest differences at length scales where the physical positioning of the point sources provides limiting factors. In the vertical direction, however, where one would expect the positioning of the sources to have less of an influence, the two distributions of maximum heights attained are virtually the same.

A.2 Connectivity

A good measure of the complexity of the entangled field produced by the abundant magnetic flux fragments observed in the quiet-Sun photosphere is given by analysing their connectivity.

Figures A.2(a) and (b) are contour plots showing the number of fragments to which a fragment of given flux connects for the point-source-per-pixel and the point-source-per-fragment representations, respectively. Although these plots are very similar, they exhibit clear differences, confirming that, rather than merely deforming the skeleton into a state that is slightly differing spatially but conserving of the original topology, representing a fragment by a single point source will actually result in changes in topology. That said, the areas where differences in connectivity occur are likely, on the whole, to involve

small unstable flux domains, so that the large flux domains that mostly characterise the topological skeleton will be consistent between the two approximations.

Statistically, however, the two representations give similar results. The point-source-per-pixel representation gives the mean number of connections at 7.03 per fragment, with a maximum of 25 connections for a single fragment, whilst the point-source-per-fragment representation gives a mean value only slightly higher at 7.12 connections per fragment, with a maximum of 24 connections. Figure A.3(a) reinforces this statistical agreement, showing no significant difference in the distribution of the number of connections for each fragment.

Figure A.3(b) shows the average partitioning of flux from a given fragment to its connected fragments. As the two curves lie on top of one another, it is clear that representing magnetic carpet fragments by single point sources has no notable effect on the mean distribution of flux over a fragment's connections.

Appendix B: Boxcar Data Smoothing

The algorithm used for smoothing an array A of N elements is that used by IDL. Typically, the smooth function in IDL returns an array R , defined as

$$R_i = \begin{cases} \frac{1}{w} \sum_{j=1}^w A_{i+j-w/2-1}, & i = \frac{w+1}{2}, \dots, N - \frac{w-1}{2} \\ A_i, & \text{otherwise} \end{cases},$$

where N is the number of elements in the array A and w is an odd number equal to the width of the smoothing window. However, here edge truncation is used, so that if the neighbourhood of a point includes a point outside the array, the nearest edge point is used to compute the smoothed result. For example, when smoothing an N -element vector with a smoothing window three points wide (i.e. $w = 3$), the first point of the result, R_1 , is set equal to $(A_1 + A_1 + A_2)/3$ if edge truncation is used (it would just be A_1 otherwise). In the same manner, the point R_N is set to $(A_{N-1} + A_N + A_N)/3$ if edge truncation is used (otherwise it would be set equal to A_N). In this way, points within a distance $w/2$ from the edge of the array are also smoothed.

In the case studied here, the value of N is dictated by P , the number of elements in the sequence of fragment fluxes being smoothed. This means that N generally varies. When $P > w$, the size of N is just P . However, in some cases, particularly when larger values of w are chosen, the value of P is actually less than the value for w . As N must be larger than w , in such scenarios an extra $w - P + 1$ “dummy” elements are added to the array A so that N is then greater than w . These extra dummy elements are all initially assigned the same value as the last point in the original sequence (i.e. A_P), and are discarded after smoothing. This allows any given sequence of points to be smoothed using a smoothing window of arbitrary width w .

Appendix C: Effects of Data Smoothing

Preparing magnetogram data for the purpose of extrapolation requires the use of thresholds in order to separate genuine signals from the noise that is inherent in magnetic field observations. In the data studied here, where fragments are tracked not only spatially but also temporally, two levels of threshold are used so that fragments whose strengths fluctuate above and below the upper threshold are tracked properly and not simply recorded as a series of births and deaths.

Despite the use of two thresholds to minimise the counting in and out of pixels with values near the upper threshold level, the total flux in each of the fragments does of course include contributions from noise in the pixels. As the method outlined in Section 5.5 for calculating emergence and cancellation in the fragments counts all changes in the fluxes of the fragments between frames as being emergences or cancellations, this inevitably results in an over-estimation of the amount of emergence and cancellation that is occurring.

Thus, in order to reduce the effects outlined above, data smoothing is applied to the time sequence of each fragment's flux. The algorithm used for the smoothing is a box-car smoothing algorithm, detailed in Appendix B. This essentially relies on an integer parameter w which defines the width of the "smoothing window" (i.e. the number of neighbouring data points used for the smoothing of a given data point). Varying the size of w subsequently varies the amount of smoothing that occurs, therefore varying the amount of emergence and cancellation that occurs.

Before proceeding any further, it is worth pointing out that since emergence and fragmentation may occur within the region of interest, it is not always possible to smooth over the entire lifetime of some fragments. In such cases, only the parts of the time sequence of the fragment's flux where no emergence or fragmentation occurs are smoothed. Of course, this will lead to peculiar jumps in the time sequences of such fragments across the points where emergence or fragmentation occur. In order to remove these anomalies, the fluxes

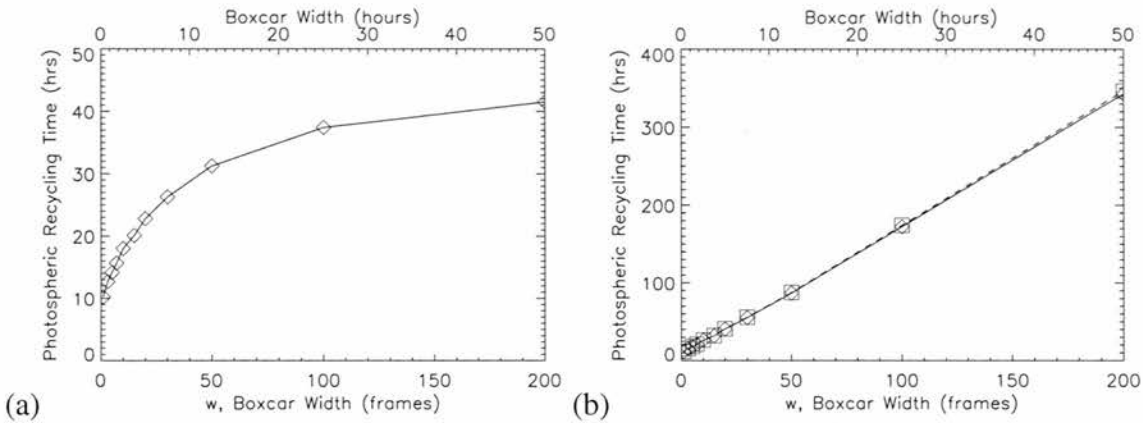


Figure C.1: (a) Time taken (in hours) to recycle all photospheric flux versus boxcar width w used in the smoothing of the fluxes of the fragments. The diamonds indicate the values obtained for specific values of w . In this plot, births and deaths of fragments, along with the fluctuations in their fluxes, have been taken into account. (b) Time taken to recycle all photospheric flux when only fluctuations in the fluxes of fragments over their lifetimes are considered. The solid line and diamonds indicate values obtained when newly born/just died fragments are copied into the frame in which they are not present, whilst the dashed line and squares indicate values obtained when newly born/just died fragments are removed from the frame in which they are present.

of the fragments that are affected by mergence and fragmentation are adjusted in accordance with Section 5.4. In this way, it is assumed that fragments that either merge or split between a given pair of magnetograms witness no emergence or cancellation. This is an unavoidable consequence of using observed data in which mergence and fragmentation occur.

Ideally, a sensible amount of smoothing should be applied so that one may be certain that spurious fluctuations in the data due to noise in the magnetogram pixels are eradicated without compromising the profiles of the fragment fluxes too much. Whilst all recycling times given in the text are calculated using a smoothing window of width 7 frames (1.75 hours), it is interesting to observe what happens to the recycling times when varying levels of smoothing are used. This is what is detailed here.

Figure C.1 shows a couple of plots that demonstrate how the recycling time for photospheric flux, given by Equation (5.22), varies as the amount of smoothing deployed varies. Plot (a) shows the photospheric recycling time calculated by measuring all changes in the fluxes of the fragments, i.e. due to births of fragments, deaths of fragments and fluctuations in the strengths of fragments. From an initial recycling time of 10 hours in the case where no smoothing is deployed, the graph asymptotes towards a figure of around 46 hours. This would essentially be the time taken to recycle all photospheric flux were the strengths of each fragment constant over its lifetime. Plot (b) in Figure C.1 shows the

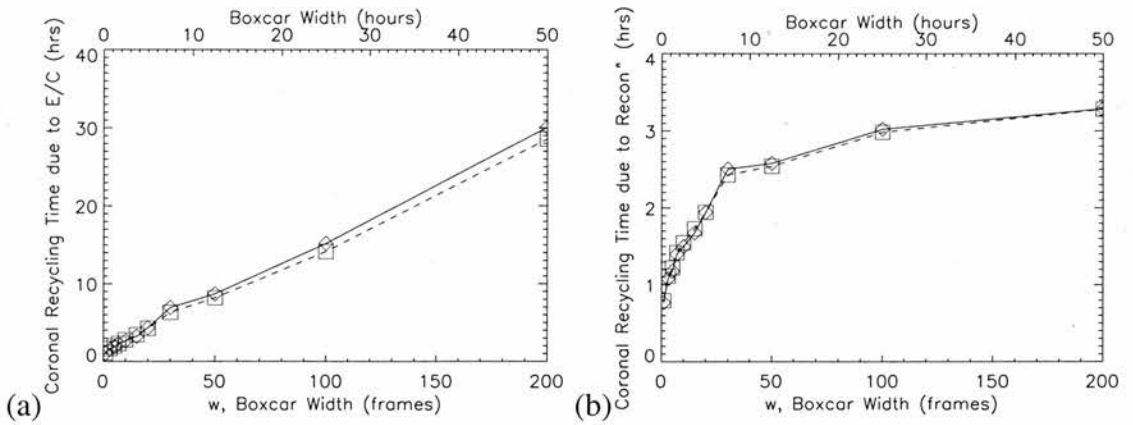


Figure C.2: (a) Time taken (in hours) to recycle all coronal flux due to emergence and cancellation of flux in the photosphere versus boxcar width w used in the smoothing of the fluxes of the fragments. Again, the solid line and diamonds indicate values obtained when newly born/just died fragments are copied into the frame in which they are not present, whilst the dashed line and squares indicate values obtained when newly born/just died fragments are removed from the frame in which they are present. (b) Time taken to recycle all coronal flux due to reconnection versus boxcar width w used in the smoothing of the fluxes of the fragments.

recycling times calculated when changes in flux associated with the births and deaths of fragments are ignored. In such a scenario, one would expect the recycling time to tend to infinity as the smoothing is increased, since the profiles of the fragments tend to one in which the fragment fluxes are constant over their lifetimes. This is clearly seen to be happening in the plots.

Corresponding coronal recycling times due to emergence and cancellation, given by Equation (5.25), are shown in Figure C.2(a). Again, the effects of the births and deaths of fragments have been neglected in the calculation of these values, meaning that as the amount of smoothing increases, the recycling time tends towards infinity. Comparing plot (b) in Figure C.1 with Figure C.2(a) suggests that the photospheric recycling time tends to infinity much quicker than the coronal recycling time. This is fairly intuitive behaviour, since one would expect a given amount of recycling in the photosphere to result in substantially more recycling in the corona, where the flux is partitioned into complex domain structures that interconnect the multitude of sources.

The recycling times due to reconnection are displayed Figure C.2(b). The times are calculated using ΔR in Equation (5.29). It can clearly be seen how varying the amount of emergence that is occurring affects the time taken to recycle all the coronal flux due to reconnection. When there is very little data smoothing applied, reconnection driven by emergence and cancellation of flux dominates over reconnection resulting from fragment motions, giving a recycling time of ~ 0.78 hours. However, as the amount of smoothing is

increased, the flux recycling occurring as a result of emergence and cancellation becomes increasingly less significant. This relates to a scenario in which reconnection occurs only as a consequence of fragment motions. In the infinity limit, footpoint motions take just below 5 hours to recycle all the flux.

Appendix D: Specific Volume about a 2D Null Point

Here an analytic expression for the value of V_0 about a null point is obtained. In appropriate cartesian coordinates, X and Y say, a 2D potential field may be represented locally in the vicinity of a null point by the flux function

$$a(X, Y) = a_* + \frac{F}{L^2}(Y^2 - X^2). \quad (\text{D.1})$$

The magnetic field which corresponds to this is

$$B_x = 2\frac{F}{L^2}Y, \quad B_y = 2\frac{F}{L^2}X, \quad (\text{D.2})$$

where the X and Y axes are orientated such that locally about the origin the field is that of a classical X-type neutral point. The quantity F/L^2 may then be physically identified as being related to the gradient of the field near the null point

$$2\frac{F}{L^2} = \frac{dB_x}{dY} = \frac{dB_y}{dX} = \pm \left| \nabla \sqrt{B_x^2 + B_y^2} \right|. \quad (\text{D.3})$$

This shows that near the null point $|\mathbf{B}|$ depends only on the distance from the null point. Hence F/L^2 describes the structure of the magnetic field near the null point. Letting δa be the difference in the flux function between a given non-singular field line a and the flux function of the separatrix a_* gives

$$\delta a = a - a_*. \quad (\text{D.4})$$

In the vicinity of the neutral point, this may be rewritten as represented by

$$\delta a = \frac{F}{L^2}(Y^2 - X^2). \quad (\text{D.5})$$

Now consider a section of a field line passing the Y axis at Y_0 and extending from $-\hat{X}$ to $+\hat{X}$. Next, consider how the specific volume of this section varies as the separatrix is approached, i.e. when $|\delta a|$ approaches zero. The value of δa for this line is

$$\delta a = \frac{F}{L^2} Y_0^2, \quad (\text{D.6})$$

and line element along this field line is

$$ds^2 = dX^2 + dY^2 = dX^2 \left(\frac{X^2}{Y^2} + 1 \right). \quad (\text{D.7})$$

With the modulus of the field being given as

$$|\mathbf{B}| = \left(4 \left(\frac{F}{L^2} \right)^2 (X^2 + Y^2) \right)^{\frac{1}{2}}, \quad (\text{D.8})$$

this leads to

$$\frac{ds}{|\mathbf{B}|} = \frac{L^2 dX \sqrt{\frac{X^2}{Y^2} + 1}}{2|F| \sqrt{X^2 + Y^2}} = \frac{L^2 dX}{2|FY|} = \frac{L^2 dX}{2|F| \sqrt{Y_0^2 + X^2}}. \quad (\text{D.9})$$

The specific volume of the line between $\pm \hat{X}$ is then

$$\hat{V}_0 = \int_{-\hat{X}}^{+\hat{X}} \frac{L^2 dX}{2|FY_0| \sqrt{1 + X^2/Y_0^2}} = \frac{L^2}{|F|} \arg \sinh \left(\frac{\hat{X}}{Y_0} \right), \quad (\text{D.10})$$

which can be expressed in terms of δa , the difference in the flux function across the separatrix

$$\hat{V}_0 = \frac{L^2}{|F|} \arg \sinh \left(\frac{\hat{X} \sqrt{|F|}}{\sqrt{L^2} \sqrt{\delta a}} \right). \quad (\text{D.11})$$

For very small δa , the approximation $\arg \sinh(u) \approx \ln(2u)$, which is valid for large u , may be used. This leads to the expression

$$\hat{V}_0 = \frac{L^2}{|F|} \ln \left(\frac{2\hat{X} \sqrt{|F|}}{\sqrt{L^2} \sqrt{\delta a}} \right) \approx \frac{L^2}{2|F|} \ln \left(\frac{4|F|}{|\delta a|} \right). \quad (\text{D.12})$$

Appendix E: Energy Storage in a 3D Configuration

It was shown in Subsection 6.6.1 that the energy stored in a $2^{1/2}$ D configuration over a fixed region following a simple shearing motion grows linearly with the number of sources through which a given amount of flux emerges. Here, similar dimensional arguments are used to explore what happens in 3D. Assuming that the initially potential magnetic field arises from a series of sources which lie in a 2D plane and are subjected to a shearing motion, it is further assumed that the overlying corona consequently suffers a quasi-static, perfect MHD change. This turns the potential magnetic configuration into one that is force-free, associated with a displacement field ξ . The resulting field perturbation is

$$\mathbf{b} = \nabla \times (\xi \times \mathbf{B}_0). \quad (\text{E.1})$$

The field in a typical 3D magnetic domain is of the order

$$B_0 \sim \frac{\Phi_0}{L_0^2}, \quad (\text{E.2})$$

where Φ_0 is a typical source flux and L_0 is a typical length scale of an average domain. As in $2^{1/2}$ D, the field contains contributions from other sources at distances greater than L_0 ; however, close to the photosphere the field is largely dominated by the sources on the boundaries of the domain, so that, even if there are thousands of sources in the configuration, only a few have a non-negligible contribution. A typical field perturbation may then be seen to be of the order

$$b_0 \sim \frac{\Phi_0}{L_0^2}. \quad (\text{E.3})$$

The energy associated with the field perturbation in a typical domain may be expressed as

$$W_b \sim b_0^2 L_0^3 \sim \frac{\Phi_0^2}{L_0}. \quad (\text{E.4})$$

If the number of sources N is then increased by a factor of \mathcal{N} to $\mathcal{N}N$, then the flux and length scales change in the following way:

$$\Phi_0 \rightarrow \frac{\Phi_0}{\mathcal{N}} \quad \text{and} \quad L_0 \rightarrow \frac{L_0}{\mathcal{N}^{1/2}}. \quad (\text{E.5})$$

This implies that the energy stored in a typical domain varies as $W_b \rightarrow W_b/\mathcal{N}^{3/2}$. As in 2D, though, the number of domains increases as the number of sources is increased. Furthermore, the majority of the extra energy stored in the system following the source displacement is likely to be stored in the low-lying domains. There are typically 3–4 planar domains per source in 3D (Schrijver and Title, 2002; see also Chapter 4). Thus, the total energy stored in the system, ΣW_b , as a result of the source displacement varies as

$$\Sigma W_b \rightarrow \frac{\Sigma W_b}{\mathcal{N}^{1/2}}. \quad (\text{E.6})$$

It may also be shown in a similar way that the total energy stored in the system following a fixed shearing motion increases linearly with a linear decrease in the length scale L_0 (i.e. $\Sigma W_b \rightarrow \Sigma W_b/\mathcal{N}$ for $L_0 \rightarrow L_0/\mathcal{N}$).

Appendix F: CD Information

Attached to this thesis is an accompanying CD, which contains animations of 3D rotations about some of the configurations studied in Chapters 2, 3, and 4. To access these animations, the file '*index.html*' should be opened in any web browser. This page gives a list of links to the animations contained on the CD, together with descriptions of the parts of the thesis to which they are relevant.

The animations on the CD are provided in both AVI and MPEG formats. It may be necessary to download a relevant browser plug-in, for example RealPlayer, from the web browser homepage (for example, for Netscape browsers, see <http://wp.netscape.com/plugins/index.html>). Alternatively, the animations may be viewed in a suitable package directly from the files on the CD.

Bibliography

- Amari, T. and Aly, J. J. (1990). Extended Massive Current Sheets in a Two-Dimensional Constant- α Force-Free Field: A Model for Quiescent Prominences. *Astron. Astrophys.*, 231:213–220.
- Axford, W. I. and McKenzie, J. F. (2002). Coronal Heating. *Advances in Space Research*, 30:505–505.
- Beveridge, C. (2003). *Magnetic Topology of the Solar Corona*. PhD thesis, Mathematical Institute, University of St Andrews.
- Beveridge, C., Longcope, D. W., and Priest, E. R. (2003). A Model for Elemental Coronal Flux Loops. *Solar Phys.*, 216:27–40.
- Beveridge, C., Priest, E. R., and Brown, D. S. (2002). Magnetic Topologies Due to Two Bipolar Regions. *Solar Phys.*, 209:333–347.
- Boyd, T. J. M. and Sanderson, J. J. (2003). *The Physics of Plasmas*. Cambridge University Press, Cambridge.
- Brown, D. S. and Priest, E. R. (1999a). The Topological Behaviour of Stable Magnetic Separators. *Solar Phys.*, 190:25–33.
- Brown, D. S. and Priest, E. R. (1999b). Topological Bifurcations in 3D Magnetic Fields. *Proc. Roy. Soc.*, 455:3931–3951.
- Brown, D. S. and Priest, E. R. (2000). Topological Differences and Similarities between Force-Free and Potential Models of Coronal Magnetic Fields. *Solar Phys.*, 194:197–204.
- Brown, D. S. and Priest, E. R. (2001). The Topological Behaviour of 3D Null Points in the Sun's Corona. *Astron. Astrophys.*, 367:339–346.
- Bungey, T. N., Titov, V. S., and Priest, E. R. (1996). Basic Topological Elements of Coronal Magnetic Fields. *Astron. Astrophys.*, 308:233–247.
- Close, R. M., Parnell, C. E., Longcope, D. W., and Priest, E. R. (2004a). Recycling of the Solar Corona's Magnetic Field. *Astrophys. J.*, 612:L81–L84.
- Close, R. M., Parnell, C. E., Mackay, D. H., and Priest, E. R. (2003). Statistical Flux

- Tube Properties of 3D Magnetic Carpet Fields. *Solar Phys.*, 212:251–275.
- Close, R. M., Parnell, C. E., and Priest, E. R. (2004b). Separators in 3D Quiet-Sun Magnetic Fields. Accepted by Solar Physics.
- Cowley, S. W. H. (1973). A Qualitative Study of the Reconnection between the Earth's Magnetic field and Interplanetary Field of Arbitrary Orientation. *Radio Science*, 8:903–913.
- Démoulin, P., Hénoux, J. C., and Mandrini, C. H. (1992). Development of a Topological Model for Solar Flares. *Solar Phys.*, 139(1):105–123.
- Domínguez Cerdeña, I., Kneer, F., and Sánchez Almeida, J. (2003). Quiet-Sun Magnetic Fields at High Spatial Resolution. *Astrophys. J.*, 582:L55–L58.
- Dungey, J. W. (1958). *Cosmic Electrodynamics*. Cambridge University Press, Cambridge.
- Durney, B. R., Young, D. S. D., and Roxburgh, I. W. (1993). On the Generation of the Large-scale and Turbulent Magnetic Fields in Solar-Type Stars. *Solar Phys.*, 145(2):207–225.
- Fukao, S., Ugai, M., and Tsuda, T. (1975). Topological Study of Magnetic Field near a Neutral Point. *Rep. Ionosphere Space Res. Jpn*, 29:133–139.
- Galsgaard, K. and Nordlund, A. (1997). Heating and Activity of the Solar Corona. 3. Dynamics of a Low Beta Plasma with Three-Dimensional Null Points. *J. Geophys. Res.*, 102:231–248.
- Galsgaard, K., Parnell, C. E., and Blaizot, J. (2000). Elementary Heating Events – Magnetic Interactions between Two Flux Sources. *Astron. Astrophys.*, 362:395–405.
- Greene, J. M. (1988). Geometrical Properties of Three-dimensional Reconnecting Magnetic Fields with Nulls. *J. Geophys. Res.*, 93:8583–8590.
- Hagenaar, H. J. (2001). Ephemeral Regions on a Sequence of Full-Disk Michelson Doppler Imager Magnetograms. *Astrophys. J.*, 555:448–461.
- Hagenaar, H. J., Schrijver, C. J., and Title, A. M. (1997). The Distribution of Cell Sizes of the Solar Chromospheric Network. *Astrophys. J.*, 481:988–995.
- Hagenaar, H. J., Schrijver, C. J., and Title, A. M. (2003). The Properties of Small Magnetic Regions on the Solar Surface and the Implications for the Solar Dynamo(s). *Astrophys. J.*, 584:1107–1119.
- Harvey, K. L. (1993). *Magnetic Dipoles on the Sun*. PhD thesis, Astronomical Institute, Utrecht University.
- Hesse, M. and Schindler, K. (1988). A Theoretical Foundation of General Magnetic Reconnection. *J. Geophys. Res.*, 93:5558–5567.
- Heyvaerts, J. and Priest, E. R. (1984). Coronal Heating by Reconnection in DC Current

- Systems. A Theory Based on Taylor's Hypothesis. *Astron. Astrophys.*, 137(1):63–78.
- Hughes, D. W., Cattaneo, F., and Kim, E. (1998). Nonlinear Multi-Cellular Fast Dynamics. *Studia Geophysica et Geodaetica*, 42:328–334.
- Inverarity, G. W. and Priest, E. R. (1999). Magnetic Null Points Due to Multiple Sources of Solar Photospheric Flux. *Solar Phys.*, 186:99–121.
- Lau, Y. T. and Finn, J. M. (1990). 3D Kinematic Reconnection in the Presence of Field Nulls and Closed Field Lines. *Astrophys. J.*, 350:672–691.
- Lau, Y. T. and Finn, J. M. (1996). Magnetic Reconnection and the Topology of Interacting Twisted Flux Tubes. *Phys. Plasmas*, 3:3983–3997.
- Levine, R. H. (1974). A New Theory of Coronal Heating. *Astrophys. J.*, 190:457–446.
- Lin, H. (1995). On the Distribution of the Solar Magnetic Fields. *Astrophys. J.*, 446:421–430.
- Livi, S. H. B., Wang, H., and Martin, S. F. (1985). The Cancellation of Magnetic Flux. I – On the Quiet Sun. *Australian J. Phys.*, 38:855–873.
- Livingston, W. C. and Harvey, J. W. (1975). A New Component of Solar Magnetism – The Inner Network Fields. *Bull. Amer. Astron. Soc.*, 7:346.
- Longcope, D. W. (1996). Topology and Current Ribbons: A Model for Current Reconnection and Flaring in a Complex Evolving Corona. *Solar Phys.*, 169:91–121.
- Longcope, D. W. (1998). A Model for Current Sheets and Reconnection in X-ray Bright Points. *Astrophys. J.*, 507:433–442.
- Longcope, D. W. (2001). Separator Current Sheets: Generic Features in Minimum-Energy Magnetic Fields Subject to Flux Constraints. *Phys. Plasmas*, 8:5277–5290.
- Longcope, D. W., Brown, D. S., and Priest, E. R. (2003). On the Distribution of Magnetic Null Points above the Solar Photosphere. *Phys. Plasmas*, 10:3321–3334.
- Longcope, D. W. and Cowley, S. C. (1996). Current Sheet Formation along Three-Dimensional Magnetic Separators. *Phys. Plasmas*, 3:2885–2897.
- Longcope, D. W. and Kankelborg, C. C. (1999). Coronal Heating by Collision and Cancellation of Magnetic Elements. *Astrophys. J.*, 524:483–495.
- Longcope, D. W. and Klapper, I. (2002). A General Theory of Connectivity and Current Sheets in Coronal Magnetic Fields Anchored to Discrete Sources. *Astrophys. J.*, 579:468–481.
- Lothian, R. M. and Browning, P. K. (1995). Coronal Magnetic Field Equilibrium with Discrete Flux Sources. *Solar Phys.*, 161:289–316.
- Maclean, R. C., Beveridge, C., Longcope, D. W., Brown, D. S., and Priest, E. R. (2004). A Topological Analysis of the Magnetic Breakout Model for an Eruptive Solar Flare.

- Submitted to Proc. Roy. Soc.
- Martin, S. F. (1984). *Proc. Symp. on Small-Scale Dynamical Processes in Quiet Sun Stellar Atmospheres*, page 30. National Solar Observatory, Sacramento Peak, NM.
- Martin, S. F. (1988). The Identification and Interaction of Network, Intranetwork, and Ephemeral-Region Magnetic Fields. *Solar Phys.*, 117(2):243–259.
- Martin, S. F. (1990). *Solar Photosphere: Structure, Convection and Magnetic Fields*, page 129. Proceedings of the 138th Symposium of International Union, Kiev, U.S.S.R., Kluwer Academic Publishers, Dordrecht.
- McKenzie, J. F., Banaszekiewicz, M., and Axford, W. I. (1995). Acceleration of the High Speed Solar Wind. *Astron. Astrophys.*, 303:L45–L48.
- Mellor, C., Gerrard, C. L., Galsgaard, K., Hood, A. W., and Priest, E. R. (2004). Numerical Simulations of the Flux Tube Tectonics Model for Coronal Heating. Submitted to *Solar Phys.*
- Meneguzzi, M. and Pouquet, A. (1989). Turbulent Dynamos Driven by Convection. *J. Fluid Mech.*, 205:297–318.
- Milnor, J. W. (1965). *Topology from the Differentiable Viewpoint*. University Virginia Press, Virginia.
- Parker, E. N. (1981). The Dissipation of Inhomogeneous Magnetic Fields and the Problem of Coronal Heating – Part Two – The Dynamics of Dislocated Flux. *Astrophys. J.*, 244:644–652.
- Parker, E. N. (1983). Magnetic Neutral Sheets in Evolving Fields – Part Two – Formation of the Solar Corona. *Astrophys. J.*, 264:642–647.
- Parker, E. N. (1988). Nanoflares and the Solar X-ray Corona. *Astrophys. J.*, 330:474–479.
- Parnell, C. E. (2001). A Model of the Solar Magnetic Carpet. *Solar Phys.*, 200:23–45.
- Parnell, C. E. (2002). Nature of the Magnetic Carpet: I Distribution of Magnetic Fluxes. *Roy. Astron. Soc.*, 335:389–398.
- Parnell, C. E. (2004). In Preparation.
- Parnell, C. E. and Galsgaard, K. (2003). Elementary Heating Events – Magnetic Interactions between Two Flux Sources. II Flux Connectivity. *Astron. Astrophys.*, submitted.
- Parnell, C. E. and Priest, E. R. (1994). Modelling of Dynamic Coronal Heating. *Proc. of the 3rd SOHO Workshop*, ESA SP-373:149–158.
- Parnell, C. E. and Priest, E. R. (1995). A Converging Flux Model for the Formation of an X-ray Bright Point above a Supergranule Cell. *Geophys. Astrophys. Fluid Dynam.*, 80:255–276.
- Parnell, C. E., Smith, J. M., Neukirch, T., and Priest, E. R. (1996). The Structure of

- Three-Dimensional Magnetic Neutral Points. *Phys. Plasmas*, 3(3):759–770.
- Petrovay, K. and Szakály, G. (1993). The Origin of Intranetwork Fields: A Small-Scale Solar Dynamo. *Astron. Astrophys.*, 274:543–554.
- Priest, E. R. (1982). *Solar Magnetohydrodynamics*. Kluwer Academic Publishers, Dordrecht.
- Priest, E. R., Bungey, T. N., and Titov, V. S. (1997). The 3D Topology and Interaction of Complex Magnetic Flux Systems. *Geophys. Astrophys. Fluid Dynamics*, 84:127–163.
- Priest, E. R., Heyvaerts, J., and Longcope, D. W. (2004). Coronal Heating at Separators and Separatrices. In Preparation.
- Priest, E. R., Heyvaerts, J. F., and Title, A. M. (2002). A Flux-Tube Tectonics Model for Solar Coronal Heating Driven by the Magnetic Carpet. *Astrophys. J.*, 576:533–551.
- Priest, E. R., Longcope, D. W., and Titov, V. S. (2003). Binary Reconnection and the Heating of the Solar Corona. *Astrophys. J.*, 598:667–677.
- Priest, E. R. and Titov, V. S. (1996). Magnetic Reconnection at Three-Dimensional Null Points. *Phil. Trans. R. Soc. Lond. A*, 354:2951–2992.
- Prim, R. C. (1957). Shortest Connection Networks and Some Generalizations. *Bell Systems Tech. J.*, 36:1389–1401.
- Roberts, B. (1991). *Advances in Solar MHD*. Cambridge University Press, Cambridge.
- Schindler, K., Hesse, M., and Birn, J. (1988). General Magnetic Reconnection, Parallel Electric Fields, and Helicity. *J. Geophys. Res.*, 93(A6):5547–5557.
- Schrijver, C. J. and Title, A. M. (2002). The Topology of a Mixed-Polarity Potential Field, and Inferences for the Heating of the Quiet Solar Corona. *Solar Phys.*, 207:223–240.
- Schrijver, C. J. and Title, A. M. (2003). The Magnetic Connection between the Solar Photosphere and the Corona. *Astrophys. J.*, 597:L165–L168.
- Schrijver, C. J., Title, A. M., Ballegoijen, A. A. V., Hagenaar, J. H., and Shine, R. A. (1997). Sustaining the Quiet Photospheric Network: The Balance of Flux Emergence, Fragmentation, Merging, and Cancellation. *Astrophys. J.*, 487:424–436.
- Schrijver, C. J., Title, A. M., Harvey, K. L., Sheeley, N. R., Wang, Y. M., van den Oord, G. H. J., Shine, R. A., Tarbell, T. D., and Hurlburt, N. E. (1998). Large-Scale Coronal Heating by the Small-Scale Magnetic Field of the Sun. *Nature*, 394:152–154.
- Simon, G. W. and Leighton, R. B. (1964). Velocity Fields in the Solar Atmosphere. III. Large-Scale Motions, the Chromospheric Network, and Magnetic Fields. *Astrophys. J.*, 140:1120–1147.
- Simon, G. W., Title, A. M., and Weiss, N. O. (2001). Sustaining the Sun's Magnetic Network with Emerging Bipoles. *Astrophys. J.*, 561:427–434.

- Title, A. M. (2000). Magnetic Fields below, on and above the Solar Surface. *Phil. Trans. Roy. Soc. London*, A358:657–668.
- Titov, V. S. and Priest, E. R. (1993). The Collapse of an X-type Neutral Point to Form a Reconnecting Time-Dependent Current Sheet. *Geophys. Astrophys. Fluid Dynam.*, 72(1-4):249–276.
- Tobias, S. M. (2002). The Solar Dynamo. *Phil. Trans. R. Soc. Lond. A.*, 360:2741–2756.
- van Ballegooijen, A. A., Nisenson, P., Noyes, R. W., Lofdahl, M. G., Stein, R. F., Nordlund, Å., and Krishnakumar, V. (1998). Dynamics of Magnetic Flux Elements in the Solar Photosphere. *Astrophys. J.*, 509:435–447.
- Vekstein, G. E. and Priest, E. R. (1992). Magneto-hydrostatic Equilibria and Cusp Formation at an X-type Neutral Line by Footpoint Shearing. *Astron. Astrophys.*, 384:333–340.
- Vekstein, G. E. and Priest, E. R. (1993). Magnetostatic Equilibria and Current Sheets in a Sheared Magnetic Field with an X-point. *Astron. Astrophys.*, 146:119–125.
- Vekstein, G. E., Priest, E. R., and Amari, T. (1990). Formation of Current Sheets in Force-Free Magnetic Fields. *Astron. Astrophys.*, 243:492–500.
- Wang, H. (1988). On the Relationship between Magnetic Fields and Supergranule Velocity Fields. *Solar Phys.*, 117(2):343–358.
- Wang, H. and Zirin, H. (1988). The Velocity Pattern of Weak Solar Magnetic Fields. *Solar Phys.*, 115(2):205–219.
- Wang, J. and Shi, Z. (1988). Intra-Network Flux Concentrations. *Chinese Astron. Astrophys.*, 12:241–248.
- Wang, J., Wang, H., Tang, F., Lee, J. W., and Zirin, H. (1988). Flux Distribution of Solar Intranetwork Magnetic Fields. *Solar Phys.*, 160:277–288.
- Wang, J., Zirin, H., and Shi, Z. (1985). The Smallest Observable Elements of Magnetic Flux. *Solar Phys.*, 98:241–253.
- Welsch, B. T. and Longcope, D. W. (1999). Statistical Properties of Magnetic Separators in Model Active Regions. *Astrophys. J.*, 552:1117–1132.
- Withbroe, G. L. and Noyes, R. W. (1977). Mass and Energy Flow in the Solar Chromosphere and Corona. *Annual Review of Astronomy and Astrophysics*, 15:363–387.
- Wolfson, R. and Low, B. C. (1988). Energy Buildup in Sheared Force-Free Magnetic Fields. *Astrophys. J.*, 391:353–358.
- Zirin, H. (1985). Evolution of Weak Solar Magnetic Fields. *Australian J. Phys.*, 38:961–969.
- Zirin, H. (1987). Weak Solar Fields and Their Connection to the Solar Cycle. *Solar Phys.*, 110:101–107.

Zwingmann, W., Schindler, K., and Birn, J. (1985). On Sheared Magnetic-Field Structures Containing Neutral POints. *Solar Phys.*, 99:133–143.